Normal Incidence Ultrasonic Beam Transmission Through Steel Plates. Measuring and Modelling The Transmission Coefficient

MASTER THESIS

By:
Ivar RAVNDAL

UNIVERSITY OF BERGEN

Department of Physics and Technology

June, 2020

Abstract

Ultrasonic beam transmission through solid plates has been extensively studied over the past decades. Through this study many anomalies have been found. Plane-wave theory can not account for these anomalies. It is therefore important to have a fundamental understanding of these effects in order to accurately model guided ultrasonic waves in solids. Through the use of experiments and modelling these effects can be studied.

The objective of this thesis is to study ultrasonic beam transmission through steel at a normal incidence angle. This study is done by studying the on-axis pressure with measurement techniques used by numerous members of the acoustics group. In addition to the on-axis pressure the use of equidistant measurements along an axis are introduced to the normal incidence ultrasonic beam transmission measurement. This use of equidistant measurements allows for the use of 2D Fourier transformations, and the study of beam transmission in the wavenumber domain. Using these pressure wavenumber spectra the reconstruction of the transmission coefficient can be achieved using results from measurements. This method is replicated in simulation by using the angular spectrum method and offers comparable results.

Acknowledgements

This thesis is part of a long-term project by the acoustics group at the University of Bergen into the study of guided ultrasonic waves (GUW). The study in this thesis was performed under the supervision of Per Lunde and co-supervisor Magne Vestrheim.

Firstly I thank my two supervisors Per and Magne. Throughout this process you have both been an immense help. You have always been willing to answer questions and offer help when needed. You have pushed me to explore aspects of problems that were not evident to me at first, and motivating me to work on.

I would also like to thank Mathias Sæther for being patient and answering any questions I had and helping along the way in anyway possible. Thank you Simen for offering to read and give feedback on the draft. Thank you Magne Aanes for letting me compare my results with yours.

Lastly thank you family, girlfriend and friends for all the support offered.

Contents

Chapter 1

Introduction

1.1 Motivation

Signal transmission through fluid embedded visco-elastic solids has an integral role in many research and industrial uses, with Guided Ultrasonic Waves (GUW) of particular interest. GUW are especially of interest in the form of non-destructive testing and evaluation (NDT & E) and non-invasive ultrasonic technology as these are favourable methods of crack detection, flow measurement, material characterization and corrosion measurements among others. However the process of signal transmission through solids is complex. As the interaction of the beam and solid can be subject to effects such as reflection, dispersion, interference and diffraction among others. It is therefore important to have a good understanding of the process of GUW in order to have reliable and accurate models of the processes. The use of numerical models and physical measurements can contribute to the understanding of this. The acoustics group at the University of Bergen have both conducted measurements and made models of this process. This thesis is a part of that research and aims to contribute to further research within this field.

1.2 Previous Work

Rayleigh first wrote about free vibrations of an infinite plate in 1888 [1]. The theory for the symmetric and anti-symmetric Lamb modes and their dispersion relation for a vacuum embedded plate was formulated by Lamb in 1889 [2], and further in 1917 [3]. Following this Reissner[4], in 1938, and Osborne and Hart, in 1945 [5] and 1946 [6], formulated the theory for these waves in a fluid embedded plate. In 1939 Sanders [7] performed measurements of transmission through thin plates. The general structure and properties for the dispersion curves for a vacuum embedded plate was found by Mindlin et al. throughout the 1950's e.g. [8]. These dispersion properties for leaky Lamb modes and numerical solutions for them have been studied by numerous researchers e.g. [9]. Throughout the 20th century these researchers, among many others, built a fundamental understanding of sound propagation and transmission through elastics. The use of plane-wave theory has been used to explain the propagation of waves in plates [4] [5]. However studies into how normal incident beams interact with solid plates show effects plane-wave theory does not account for. These include increase of on-axis transmitted pressure, frequency downshift and narrowing of the transmitted beam, all associated with the excitation of leaky Lamb waves e.g.[10, 11, 12, 13]. The acoustics group at the University of Bergen have conducted significant research into the transmission of sound through elastic plates. Among others, in 2008 Lohne et al. [12] wrote on ultrasonic signal transmission in plates and compared simulated models with experiments. Lohne observed the three

aforementioned effects through measurements. In 2011 Aanes et al. compared simulated beam interactions at normal incidence using finite element method and comparing with an angular spectrum method and measurements [13] confirming the results of Lohne. Aanes continued the research into his PhD-thesis [11] developing two models for simulation of beam transmission which incorporated the transducer into the simulation allowing for more realistic beam interactions with the plate. In 2017 Aanes et al. wrote on and discussed the complex dispersion properties of Lamb and leaky Lamb modes in elastic and viscoelastic plates [14].

The transmission coefficient, T, is a plane-wave coefficient and describes the transmission of plane waves through the solid. A finite transducer is however not a plane-wave transmitter and has a complex angular spread. This dilemma has been solved numerous ways, among others using a large ($80\,mm \times 40\,mm$) ultrasonic transducer by Cawley [10] and using spacial distributed measurements e.g. [15, 16]. Safaeinili et al. [16] used air coupled materials and many different emitter-receiver positions and angles to synthesize a wide angle focused transducer aperture. Through the summation of these one dimensional scans they were able to reconstruct the transmission coefficient with excellent agreement to theory. Joecker and Smeulders [15] used the synthesized aperture technique of Safaeinili in conjunction with spatial measurements without the solid for spectral decomposition in order to determine the transmission coefficient, and found excellent agreement between the measurements and theory. Both of these techniques used angled beam incidence and reconstructed the transmission coefficient as a function of frequency and and incident angle.

The modelling of sound transmission has been done in numerous ways including more recently within Gaussian beam method e.g. [17], Finite Element Modelling (FEM) e.g. [18, 19], Distributed Point Source Modelling (DPSM) e.g. [20] and Angular Spectrum Method (ASM) e.g. [21, 22]. The Angular spectrum method simulates a baffled piston, with the sound-field decomposed into infinitely many plane waves, allowing for plane-wave theory and the use of plane-wave transmission and reflection coefficients. FE and FEM can simulate a real transducer and it's sound field, making it more accurate, but is load heavy. Kocbach developed a FEM program for piezoelectric transducers [23] and has been used extensively in the Acoustics group at the university of Bergen. Midtbø [24] developed an ASM model based on a model developed by Anderson and Martin [25].

1.3 Objective

The objective of this thesis is to study the beam transmission through a steel plate from normal incidence, this includes the excitation of leaky Lamb waves and the the effects associated with this from the plate. The goal is to study this through measurement and compare with an implementation of ASM based on the model by Midtbø [24]. Through the measurement and simulation of the pressure spectra, effects such as transmission can be studied. Furthermore, to reconstruct the transmission coefficient as a function of the horizontal wavenumber and frequency using the normal incidence measurements. This will be done by using the same measurement techniques that have been previously utilized by the acoustics group [11, 24, 26], but introducing equidistant traversing measurements along an axis in order to transform the measurements from the spatial domain to the wavenumber domain. Throughout this process several comparisons to previous works will be made.

1.4 Outline of Thesis

In Ch. 2 the theory that forms the basis for this thesis is presented. This includes plane-wave transmission, a summarized derivation of Lamb modes and leaky Lamb modes. The theory the simulation model used in this thesis. And the equations for the Fourier transformations used.

In Ch. 3 the different experimental setups are explained, including the components used. The different methods used to conduct the measurements are presented. The Experimental setups for both on-axis and transverse measurements are presented. Lastly the methods used for post-processing are presented.

In Ch. 4 the simulation model is discussed. The different variables and parameters used are presented and discussed. Lastly the different post-processing methods used are presented, this includes the testing of post-processing methods used in the experimental setup.

In Ch. 5 the results from the simulations and measurements are presented. This includes all the stages of the simulation and measurements. For the simulations this entails the verification of post-processing. For the measurements this includes results from both on-axis and transverse measurements. Lastly the results are compared.

In Ch. 6 a final conclusion on the work throughout the thesis is given and suggestions for further work.

Chapter 2

Theory

In this chapter the theory this thesis is based upon will be presented. The theory is a selection of different subjects ranging from basic beam transmission to a specific simulation method. In Sect. 2.1 the theory of beam transmission is presented, this includes the pressure-to-pressure transfer function. Sect. 2.2 and 2.3 present the theory for Lamb and leaky Lamb modes. Sect. 2.4 presents the theory and equations for the simulation method Angular spectrum method (ASM). Lastly the theory for the discrete Fourier transform and Hankel transformation is presented in Sect. 2.5.

2.1 Beam Transmission

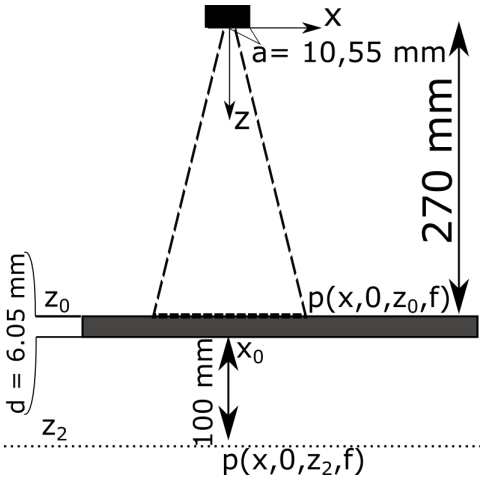

FIGURE 2.1: Illustration of beam transmission from baffled piston through fluid embedded solid plate, y-axis is pointing out of paper.

Fig. 2.1 shows a model of the system used in this thesis and is based on the model used by Aanes [11]. The model is the basis for both simulation and measurements. This model has a uniformly vibrating circular baffled piston radiating towards a solid plate with infinite extent in two directions, submerged in a fluid. The piston is assumed to be perfectly perpendicular to the z-axis and thus having an incident angle $\theta = 0$ with the z-axis. As the angle θ is zero it is not shown in the figure. The coordinates are shown in the figure with the x-axis horizontal and z-axis vertical, and y-axis out of the paper, with origin placed at the center of the pistons lower face. The plate has infinite extent in the x and y-directions and a thickness of $d = 6.05mm$ in the z-direction. The piston has a radius of $a = 10.55mm$, why this radius is chosen is discussed in Sect 4.1. The solid plate has its upper face placed at $z = 270\,mm$ and is denoted z_0 which is consistent with previous work such as Aanes [11]. The piston

uniformly vibrates and radiates a pulsed ultrasonic beam into the fluid propagating at fluid velocity c_f. The pressure at the piston-fluid interface is denoted $p(x_0, 0, 0, f)$, where x_0 denotes $x = 0$ and f is the frequency of the pulsed beam. The beam then reaches the fluid solid interface at z_0. The pressure spectrum at this interface is denoted $p(x, 0, z_0, f)$. The beam is transmitted through the solid plate, this process is expanded on in Sect. 2.2. The lower plate face then re-radiates into the fluid. The transmitted pressure spectrum used throughout simulations and measurements is located 100 mm below the lower face of the solid plate at position $z_2 = 376.05mm$. This pressure spectrum is denoted $p(x, 0, z_2, f)$. This model is symmetric around the z-axis and therefore only the z and x coordinates will be used from this point on. The y-coordinate can be assumed to be $y = 0$ if not specified otherwise. The entire system is assumed to be lossless.

2.1.1 Transfer Function

The pressure-to-pressure transfer function, or H_{pp}, is used in order to investigate the transmission through the solid plate. The equation is consistent with its use previously [11, 24, 27, 28].

$$H_{pp}(x, z_2, f) = \frac{p(x, z_2, f)}{p(x_0, z_0, f)}. \tag{2.1}$$

Where $p(x_0, z_0, f)$ is the incident pressure located at distance z_0 from the source. $p(x, z_2, f)$ is the transmitted pressure spectrum at the position (x, z_2). The H_{pp}-transfer function is often plotted logarithmic as $20log_{10}(H_{pp})$.

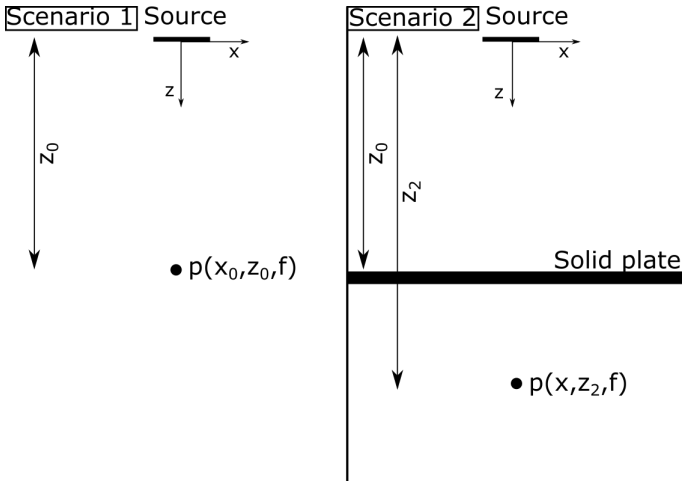

FIGURE 2.2: Illustrated position of pressure measurement for H_{pp} transfer function. y-axis is pointing out of paper

Fig. 2.2 an example of the positions for $p(x, z_2, f)$ and $p(0, z_0, f)$, are given and how they can be oriented in relation to one another.

2.2 Lamb Modes

The derivation and formulation of plane waves in elastic media has been done by many, and are cited by Aanes, but this brief formulation will follow the one given by Aanes [11]. Lamb modes occur in solid plates in a vacuum [2]. The plate is assumed to be of infinite extent in the x, y directions and isotropic homogeneous. There is also assumed to be no Lamb mode particle motion in the y-direction as this is confined to the x, z directions, making this a 2D-description. The confinement of particle motion means shear horizontal waves (SH) are excluded from the derivation. This is explored further later on in the derivation. Lamb modes are divided into two distinct type of modes, symmetric and anti-symmetric. Lamb waves are the waves propagating through the solid and are the superposition of propagating longitudinal and shear modes [29]. The longitudinal waves, denoted P (Primary), propagate in the medium as the compression an rarefaction of the solid. The shear waves, denoted S, propagate through the shear displacement of particles perpendicular to the direction of wave propagation [29]. Here only shear vertical waves are used further, denoted SV.

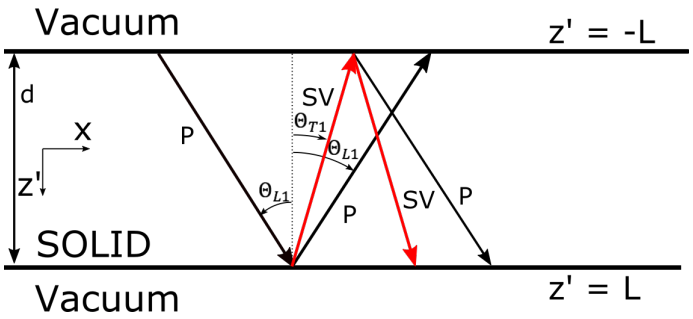

FIGURE 2.3: Illustration of propagation of Lamb wave within a vacuum embedded solid plate of thickness d. y-axis is pointing out of paper.

The propagation of Lamb waves is illustrated in Fig. 2.3. Here the z'-axis is oriented the same as z in Fig. 2.1, but has the origin placed in the middle of the solid plate. The plate has a thickness of $d = 2L$. The longitudinal and shear velocities are given respectively by

$$c_L = \sqrt{\frac{\lambda + 2\mu}{\rho_s}} \tag{2.2}$$

and

$$c_S = \sqrt{\frac{\mu}{\rho_s}}. \tag{2.3}$$

The linearized displacement equation of motion for an isotropic elastic, homogeneous solid medium is given as

$$(\lambda + 2\mu)\nabla(\nabla \cdot \underline{\boldsymbol{u}}) - \mu[\nabla \times (\nabla \times \underline{\boldsymbol{u}})] = \rho_s \frac{\partial^2 \underline{\boldsymbol{u}}}{\partial t} \tag{2.4}$$

where λ is the first Lamé parameter, the elastic modulus, and μ is the second Lamé parameter, the shear modulus. $\underline{\boldsymbol{u}} = (u_x, u_y, u_z)$ is the particle displacement and ρ_s is the density of the solid and t is time [30]. Equation 2.4 can be decomposed into two new expressions by using the longitudinal and shear velocities introduced in Eq. 2.2 and 2.3 [12].

$$(\nabla^2 - \frac{1}{c_L^2}\frac{\partial^2}{\partial t^2})\Phi = 0 \tag{2.5}$$

and

$$(\nabla^2 - \frac{1}{c_s^2}\frac{\partial^2}{\partial t^2})\underline{\Psi} = 0 \tag{2.6}$$

The Hermholtz decomposition yields us the displacement vector, $\underline{\boldsymbol{u}}$ expressed as the scalar potential, Φ and a vector potential, $\underline{\Psi}$, i.e. $\underline{\boldsymbol{u}} = \nabla\Phi + \nabla \times \underline{\Psi}$. Here Eq. 2.5 describes the longitudinal wave and Eq. 2.6 describes the shear wave. As stated previously the particle motion is restricted to the (x, z)-plane. This can be done without any loss of generality [12]. The waves can propagate in the x-direction, making Φ and $\underline{\Psi}$ independent of y, thus making $\frac{\partial}{\partial y} = 0$. The horizontal and vertical displacements and stresses are given as [31]

$$u_x = \frac{\partial \Phi}{\partial x} - \frac{\partial \Psi_y}{\partial z'}, \tag{2.7}$$

$$u_{z'} = \frac{\partial \Phi}{\partial z'} + \frac{\partial \Psi_y}{\partial x}, \tag{2.8}$$

$$T_{z'z'} = (\lambda + 2\mu)(\frac{\partial u_{z'}}{\partial z'}) + \lambda(\frac{\partial u_x}{\partial x} + \frac{\partial u_y}{\partial y}), \tag{2.9}$$

$$T_{xz'} = \mu(\frac{\partial u_x}{\partial z'} + \frac{\partial u_{z'}}{\partial x}). \tag{2.10}$$

By separation of variables the solutions for the scalar fields and vector fields, Φ and $\underline{\Psi}$, are given as [12]

$$\Phi = (A^- e^{-ih_{z'}z'} + A^+ e^{ih_{z'}z'})e^{i(\eta x - \omega t)} \tag{2.11}$$

and

$$\Psi_y = (B^- e^{-ik_{z'}z'} + B^+ e^{ik_{z'}z'})e^{i(\eta x - \omega t)}, \tag{2.12}$$

where

$$\omega = 2\pi f. \tag{2.13}$$

Here A_2^- and A_2^+ are the longitudinal wave amplitudes in positive and negative z'-directions within the solid. B_2^- and B_2^+ are the equivalent amplitudes only for shear waves. Here the formulation differs from Aanes [11], as he uses a time convention of $e^{i\omega t}$, but here a time convention of $e^{-i\omega t}$ will be used in order to be consistent with other sections. The wavenumbers for the longitudinal and shear waves are given as [11]

$$h = \frac{\omega}{c_L}, \tag{2.14}$$

$$k = \frac{\omega}{c_S}, \tag{2.15}$$

and the vertical components of these and the horizontal wavenumber η are given as [32]

$$h_{z'} = \begin{cases} \sqrt{h^2 - \eta^2} & \text{for } \eta \leq h \\ i\sqrt{\eta^2 - h^2} & \text{for } \eta > h \end{cases}, \tag{2.16}$$

$$k_{z'} = \begin{cases} \sqrt{k^2 - \eta^2} & \text{for } \eta \leq k \\ i\sqrt{\eta^2 - k^2} & \text{for } \eta > k \end{cases}, \tag{2.17}$$

$$\eta = h_x = k_x. \tag{2.18}$$

The boundary conditions for an elastic plate in a vacuum are zero normal and shear stresses at the interface of the solid and vacuum, such that

$$T_{z'z'} = 0, \quad \text{at} \quad z' = \pm L \tag{2.19}$$

$$T_{xz'} = 0, \quad \text{at} \quad z' = \pm L. \tag{2.20}$$

The rest of the derivation and formulation of the Lamb modes will not be included in this thesis, rather a brief summation of the steps will be given. Aanes [11] following [12] introduces trigonometric functions for Eqs. 2.11 and 2.12. Further these two functions are inserted into the equations for displacement and stress Eqs. 2.7, 2.8, 2.10 and 2.9. Using the boundary conditions from Eqs. 2.19 and 2.20 and Gaussian elimination of the trigonometric equations for displacement and stress a matrix is obtained. Setting the determinant of the matrix to zero, the dispersion relation for the symmetric and anti-symmetric lamb modes for a solid plate in a vacuum are given. This defines the symmetric and anti-symmetric modes for the vacuum embedded solid plate as [11]

$$\text{Symmetric} : \frac{\tan(k_{z'}L)}{\tan(h_{z'}L)} = -\frac{4\eta^2 h_{z'} k_{z'}}{(2\eta^2 - k^2)^2}, \tag{2.21}$$

$$\text{Anti} - \text{symmetric} : \frac{\tan(k_{z'}L)}{\tan(h_{z'}L)} = -\frac{(2\eta^2 - k^2)^2}{(4\eta^2 h_{z'} k_{z'})}. \tag{2.22}$$

These are further defined as the characteristic functions for the symmetric, S, and anti-symmetric, AS, modes

$$S = \frac{(k^2 - 2\eta^2)^2}{tan(h_{z'}L)} + \frac{4\eta^2 h_{z'} k_{z'}}{tan(k_{z'}L)} = 0 \tag{2.23}$$

and

$$AS = \frac{(k^2 - 2\eta^2)^2}{tan(k_{z'}L)} + \frac{4\eta^2 h_{z'} k_{z'}}{tan(h_{z'}L)} = 0. \tag{2.24}$$

2.2.1 Cut-off Frequencies

Some certain frequencies generate standing compressional and shear waves across the thickness of the plate [11, 33]. This happens when the phase velocity of the Lamb waves approach infinity [11, 34]. This can be calculated by letting the horizontal wavenumber η approach zero in Eqs. 2.21 and 2.22. The phase-velocity in the x-direction is given as [11, 12, 34]

$$c_{ph} = \frac{\omega}{\eta}. \tag{2.25}$$

Eqs. 2.21 and 2.22 become zero if the numerator or denominator of the expressions become zero or infinity,

$$\lim_{kL \to n\pi} tan(kL) = 0 \text{ or } \lim_{kL \to \frac{n\pi}{2}} tan(kL) = \infty \; where \; n = 1, 2, 3... \tag{2.26}$$

This gives us cut-off frequencies for symmetric Lamb modes [11]

$$f^S_{tn} = \frac{2nc_S}{4L}, n = 1, 2, 3, ... \text{ and } f^S_{lm} = \frac{(2m-1)c_L}{4L}, m = 1, 2, 3, ... \tag{2.27}$$

and for anti-symmetric modes

$$f^A_{ln} = \frac{2nc_L}{4L}, n = 1, 2, 3, ... \text{ and } f^A_{tm} = \frac{(2m-1)c_S}{4L}, m = 1, 2, 3, ... \tag{2.28}$$

Where f^S_{tn} is the corresponding frequencies for the symmetrical thickness-shear, TS, modes. f^S_{lm} is the corresponding frequencies for the symmetrical thickness-extensional, TE, modes. f^A_{tm} and f^A_{ln} are the equivalent frequencies for the anti-symmetrical TS and TE modes respectively

2.3 Leaky Lamb Modes

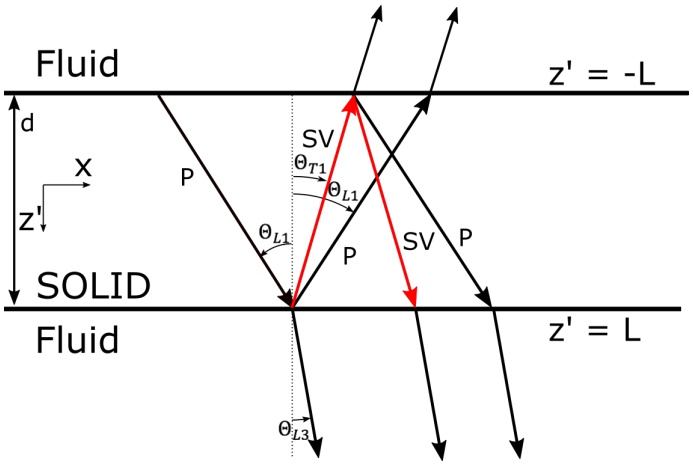

FIGURE 2.4: Illustration of leaky Lamb wave propagation through fluid embedded solid plate with thickness d. y-axis pointing out of paper.

If the solid plate, of thickness $d = 2L$, is submerged in a single fluid propagating waves in the solid can leak energy into the fluid. These waves leaking energy into the fluid are called leaky Lamb waves. The waves generate a pressure wave in the fluid, illustrated in Fig. 2.4. The pressure wave in fluid travel with velocity c_f.

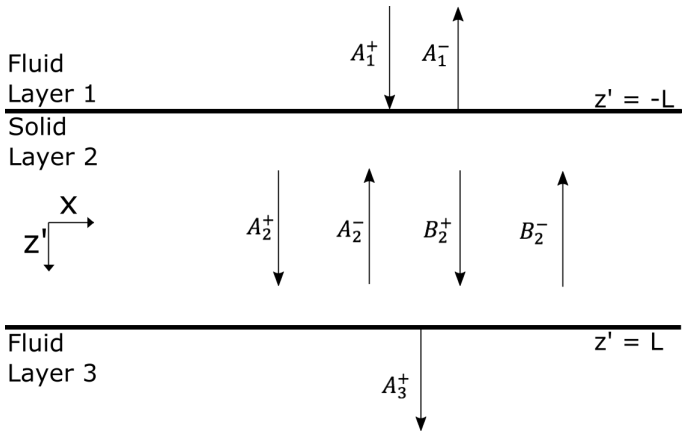

FIGURE 2.5: Illustration of solid plate embedded in fluid

The following derivation also follows [11, 12]. Fig. 2.5 shows the solid plate immersed in a single fluid. The figure is divided into three layers. Layer 1 is the fluid above the plate, the plate is layer 2 and the fluid below the plate is layer 3. In Layer 1 an incident plane wave A_1^+, where 1 denotes layer and $+$ denotes the propagating z'-direction, coming from $z' = -\infty$. A reflected plane wave A_1^-, also in layer 1, is

propagating towards $z' = -\infty$. In layer 3 a transmitted plane wave A_3^+ is propagating towards $z' = \infty$. The waves in layer 1 and 3 can written as [11, 12]

$$\Phi_1 = A_1^+ e^{ih_{f,z'}z'} + A_1^- e^{-ih_{f,z'}z'} \tag{2.29}$$

and

$$\Phi_3 = A_3^+ e^{ih_{f,z'}z'}. \tag{2.30}$$

The boundary conditions for an isotropic infinite plate, fully immersed in a single fluid, are continuity of normal displacement $u_{z'}$, normal stress $T_{z'z'}$ and vanishing shear stress $T_{xz'}$, and are given as [11, 12]

$$u_{z',n} = u_{z',n+1} \text{ at } z' = \pm L \tag{2.31}$$

$$T_{z'z',n} = T_{z'z',n+1} \text{ at } z' = \pm L \tag{2.32}$$

$$T_{xz',n} = 0 \text{ at } z' = \pm L \tag{2.33}$$

Where n and $n+1$ denote the layer number, 1,2 or 3. The vertical wavenumber for the fluid, $h_{f,z'}$ is defined as [11, 12]

$$h_{f,z'} = \begin{cases} \sqrt{h_f^2 - \eta^2} & \text{for } \eta \leq h_f \\ i\sqrt{\eta^2 - h_f^2} & \text{for } \eta > h_f. \end{cases}, \tag{2.34}$$

Where [35]

$$h_f = \frac{\omega}{c_f}. \tag{2.35}$$

The horizontal and normal displacement, and the normal stress in layers 1 and 3 are now given as

$$u_{x,1\wedge 3} = \frac{\partial \Phi}{\partial x}, \tag{2.36}$$

$$u_{z',1\wedge 3} = \frac{\partial \Phi}{\partial z'}, \tag{2.37}$$

$$T_{z'z',1\wedge 3} = -p = \lambda_f (\frac{\partial u_x}{\partial x} + \frac{\partial u_{z'}}{\partial z'}). \tag{2.38}$$

Where p is the sound pressure and λ_f is the Lamé parameter for the fluid. For layer 1 this is given as [[11] [12]]

$$u_{z',1} = ih_{f,z'}[A_1^+ e^{ih_{f,z'}z'} - A_1^- e^{-ih_{f,z'}z'}], \tag{2.39}$$

$$T_{z'z',1} = -p = \rho_f \omega^2 [A_1^+ e^{ih_{f,z'}z'} - A_1^- e^{-ih_{f,z'}z'}]. \tag{2.40}$$

For layer 3 this is given as

$$u_{z',3} = ih_{f,z'} A_3^+ e^{ih_{f,z'}z'}, \tag{2.41}$$

$$T_{z'z',3} = -p = -\rho_f \omega^2 A_3^+ e^{ih_{f,z'}z'}. \tag{2.42}$$

As in the previous section the further derivation will not be explored, but a more rigorous one can be found in Aanes thesis [11]. A brief summary of what is done will be given. Using the boundary conditions at $z' = \pm L$ and using trigonometric functions the displacement u'_z and $T_{z'z'}$ are rewritten. $T_{xz'}$ is the same as in Sect. 2.2. These equations are arranged into matrix $\boldsymbol{A}$ [11]. The dispersion relations for the symmetric and anti-symmetric leaky Lamb waves are found by setting determinant of the matrix to zero, $det|\boldsymbol{A}| = 0$, The determinant is calculated using cofactor expansion [11]. Then the dispersion relation for the symmetrical and anti-symmetrical leaky Lamb modes for an infinite isotropic plate fully immersed in a single fluid are given as [11]

$$S + iY = 0 \tag{2.43}$$

and

$$AS - iY = 0. \tag{2.44}$$

Where [11]

$$Y = \frac{\rho_f h_{z'}}{\rho_s h_{f,z'}} k^4 \tag{2.45}$$

2.3.1 Plane-wave Transmission and Reflection Coefficients for Fluid Embedded Plate

The transmission and reflection coefficients are more rigorously derived by Aanes [11] and Lohne [12], but a summation of what is done will be given. The time convention used here is $e^{-i\omega t}$. Setting the incident wave, $A_1^+ = 1$ and inserting this into equations the for the reflection and transmission coefficient given as [12, 11]

$$R(\eta, L, f) = \frac{A_1^-}{A_1^+} e^{i2h_{f,z'}L} \tag{2.46}$$

and

$$T(\eta, L, f) = \frac{A_3^+}{A_1^+} e^{i2h_{f,z}L}. \tag{2.47}$$

Using Cramer's rule and using the matrix, $\boldsymbol{A}$, from Sect. 2.3 A_1^- and A_3^+ are calculated [11]. Giving the transmission and reflection coefficient for infinite isotropic plate immersed in a single fluid

$$T(\eta, L, f) = \frac{iY(AS + S)}{(S - iY)(AS + iY)} \tag{2.48}$$

and

$$R(\eta, L, f) = \frac{SAS - Y^2}{(S - iY)(AS + iY)}. \tag{2.49}$$

AS, S and Y are given respectively in Eqs. 2.23, 2.24 and 2.45.

2.4 Angular Spectrum Method

In this section the simulation method Angular Spectrum Method (ASM) will be presented. This ASM model was developed Midtbø [24] and was implemented in this thesis in Matlab. The Angular Spectrum Method simulates a uniformly vibrating planar circular piston in a rigid baffle. The piston is radiating, at an incident angle of $\theta = 0$, into a fluid with a solid steel plate at a distance of 270 mm. The piston is assumed to be vibrating uniformly at a constant normal surface velocity of v_0. The velocity of the fluid is c_f and the system is assumed to be lossless. Fig. 2.1 shows the system in detail. In ASM cylindrical coordinates replace the Cartesian coordinates of Sect. 2.1. The position is now a function of (r, z) where r represents the radial distance and z represents the vertical distance, the system is assumed to be symmetrical around the z-axis. All other variables are still consistent with section 2.1.

2.4.1 ASM Method

As stated previously the normal particle velocity on the piston surface, $v_z(r, z = 0, f)$, is assumed to be constant and uniform, this boundary condition is written as [24, 35]

$$v(r, z = 0, f) = \begin{cases} v_0, & r \leq a \\ 0, & r \geq a \end{cases} \tag{2.50}$$

where a is the radius of the piston. A Hankel transform/Fourier-Bessel transform is used to decompose the normal particle velocity and is given as [24, 31]

$$V_z(\eta_r, 0, f) = 2\pi \int_0^\infty v_z(r, 0, f) J_0(\eta_r r) r dr. \tag{2.51}$$

Here η_r is distinguished from η of Sect. 2.2. Here η_r is a function of r and is defined as the horizontal wavenumber $\eta_r = h_r$. $V_z(\eta_r, 0, f)$ is known as the angular spectrum of $v_z(r, 0, f)$ and is characterized by the dependence on the horizontal wavenumber η_r. J_0 is the zeroth order Bessel function of the first kind. Here a time convention of $e^{-i\omega t}$ is used. A known integral identity is used to write the angular spectrum as [24, 31]

$$V_z(\eta_r, 0, f) = 2\pi v_0 \int_0^a J_0(\eta_r r) r dr = 2\pi a v_0 \frac{J_1(a\eta_r)}{\eta_r} \tag{2.52}$$

Where J_1 is the first order Bessel function of the first kind. This function is known as the source aperture function. The identity $2J_1(a\eta_r)/a\eta_r$ is the directivity function also known as the Jinc-function [24], which has the property [24]

$$\lim_{x \to 0} \frac{2J_1(x)}{x} = 1. \tag{2.53}$$

The source aperture from Eq. 2.52 and the identity from Eq. 2.53 will be used later on. The actual field variable of interest is the pressure, which is obtained from the angular spectrum, Eq. 2.51. This is done by using Euler's equation and Fourier transform [35]. This derivation is expanded on in Midtbø's thesis [24], but results in the equation

$$P(\eta_r, 0, f) = \frac{\rho_f \omega}{h_{z,f}} V(\eta_r, 0, f). \tag{2.54}$$

Here ρ_f is the fluid density and $h_{z,f}$ is fluid vertical wavenumber. When the pressure is a function of the horizontal wavenumber it is referred to as the pressure wavenumber spectrum. The equation is not valid for $h_{f,z} = \eta_r$, because the denominator of the fraction would become 0 and result in a singularity. This is discussed further in Sect. 4.1.1. Using the Jinc function identity from Eq. 2.53 and Eq. 2.52 we can rewrite Eq. 2.54

$$P(\eta_r, 0, f) = \pi a^2 \frac{\rho_f \omega}{h_{z,f}} v_0 \frac{2J_1(\eta_r a)}{\eta_r a}. \tag{2.55}$$

Giving the pressure wavenumber spectrum at $z = 0$. The pressure in the wavenumber domain at distance z_0 is found by using plane wave field extrapolation [32]

$$P(\eta_r, z, f) = P(\eta_r, 0, f) e^{(ih_{z,f}z)}. \tag{2.56}$$

Accounting for a steel plate the transmission coefficient, $T(\eta_r, d, f)$, which is defined Eq. 2.48, but defined here with cylindrical coordinates. $T(\eta_r, d, f)$ is introduced to Eq. 2.56

$$P(\eta_r, z_2, f) = P(\eta_r, 0, f) T(\eta_r, d, f) e^{ih_{f,z}(z_2 - d)}. \tag{2.57}$$

Here d is the thickness of the steel plate and z_2 denotes the z-position of the transmitted pressure. The wave field propagation term has $(z_2 - d)$, as the transmission coefficient includes the propagation through the plate. In order to get the pressure from the wavenumber-domain to the spatial-domain an inverse Hankel transform is used on Eqs. 2.56 and 2.57 and give [32]

$$p(r, z, f) = \frac{1}{2\pi} \int_0^\infty P(\eta_r, z, f) J_1(\eta_r r) \eta_r d\eta_r. \tag{2.58}$$

and

$$p(r, z_2, f) = \frac{1}{2\pi} \int_0^\infty P(\eta_r, z_2, f) J_0(\eta_r r) \eta_r d\eta_r. \tag{2.59}$$

The pressure here is a function of r the spatial position, and is referred to as the pressure spectrum.

2.4.2 Pressure Calculated Transmission Coefficient

In addition to Eq. 2.48 the transmission coefficient can also be calculated using the calculated the pressure wavenumber spectra $P(\eta_r, z_2, f)$ and $P(\eta_r, z_0, f)$ from Eqs. 2.57 and 2.56 respectively. Here z_0 denotes the pressure at the face of the steel plate. Rearranging Eq. 2.57 we can calculate the transmission coefficient with

$$T(\eta_r, d, f) = \frac{P(\eta_r, z_2, f)}{P(\eta_r, z_0, f) e^{ih_{f,z}(z_2 - z_0 - d)}}. \tag{2.60}$$

Here the incident pressure is calculated to z_0, this is accounted for in the wave field propagation term. Eq. 2.60 is used further in Ch. 3 and 4. The thickness of the plate $d = 2L$ is assumed to be unchanged further and is not listed as one of the variables in further use.

2.5 Fourier Transformation

In this section the equations for the Discrete Temporal Fourier transformation and the Hankel transformation will be discussed. This is the basis of many simulation and post processing methods discussed in Chs. 3 and 4.

2.5.1 Discrete Fourier Transform (DFT)

The Fourier method is a mathematical operation that decomposes /or transforms for example a signal of time into its frequency components. We can distinguish two types of transformations, temporal and spatial. The temporal Fourier transformation takes a continuous signal of time and transforms it to the frequency domain. For sampled signals the signal is not continuous but is a set of discrete values. The discrete Fourier transform (DFT) approximates the Fourier transform as a sum of all the samples. The temporal DFT is given as [32]

$$F(f) = \sum_{t=0}^{N-1} f(t) e^{i2\pi ft/N}. \tag{2.61}$$

Where N is the number of of samples.

2.5.2 Hankel transformation

The Hankel transform of the zeroth order, or Fourier-Bessel transform, is a 2D Fourier transform that assumes rotational symmetry as in Sect. 2.4. In the Hankel transformation used in this thesis the pressure is assumed to be symmetrical around the z-axis. The Hankel transformation from the spatial x-domain to the wavenumber η-domain is given as [32]

$$F(\eta) = \frac{1}{2\pi} \int_0^\infty f(x) J_0(\eta x) \eta d\eta. \tag{2.62}$$

The inverse of Eq. 2.62 going from the wavenumber η-domain to the spatial x-domain is given as [32]

$$f(x) = 2\pi \int_0^\infty F(\eta) J_0(\eta x) x dx. \tag{2.63}$$

Chapter 3

Experimental Setup and Method

Through this chapter the experimental setup and individual components will be presented. Following this the methods used for measurement and post-processing are shown. This setup has was first used in this configuration by Aanes [11], and subsequently by Midtbø [24] and Eileraas [26]. The basis for this setup is described in Sec. 2.1. In Sect. 3.1.1 the components of the experimental setup are presented. In Sect 3.1 the equipment used throughout the measurements are discussed. Sect. 3.2 presents the different experimental configurations used in this thesis. The methods used to conduct the measurements are presented in Sect. 3.3. In Sect. 3.4 the post-processing methods are presented.

3.1 Equipment

In this section the equipment used throughout the measurements are presented. The equipment remains the same through all the different measurements.

3.1.1 Experimental Setup

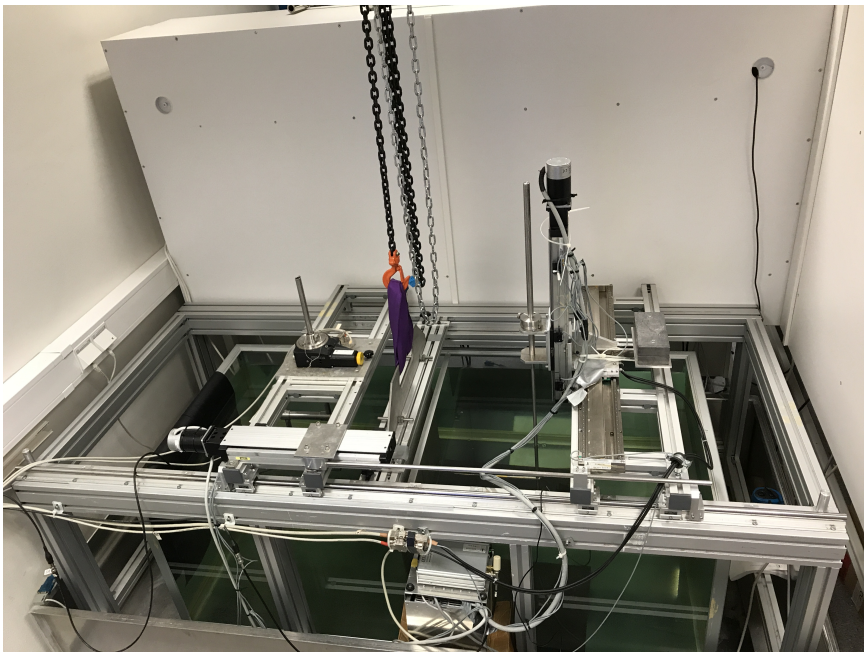

FIGURE 3.1: Photo of measurement tank with steel plate immersed in water

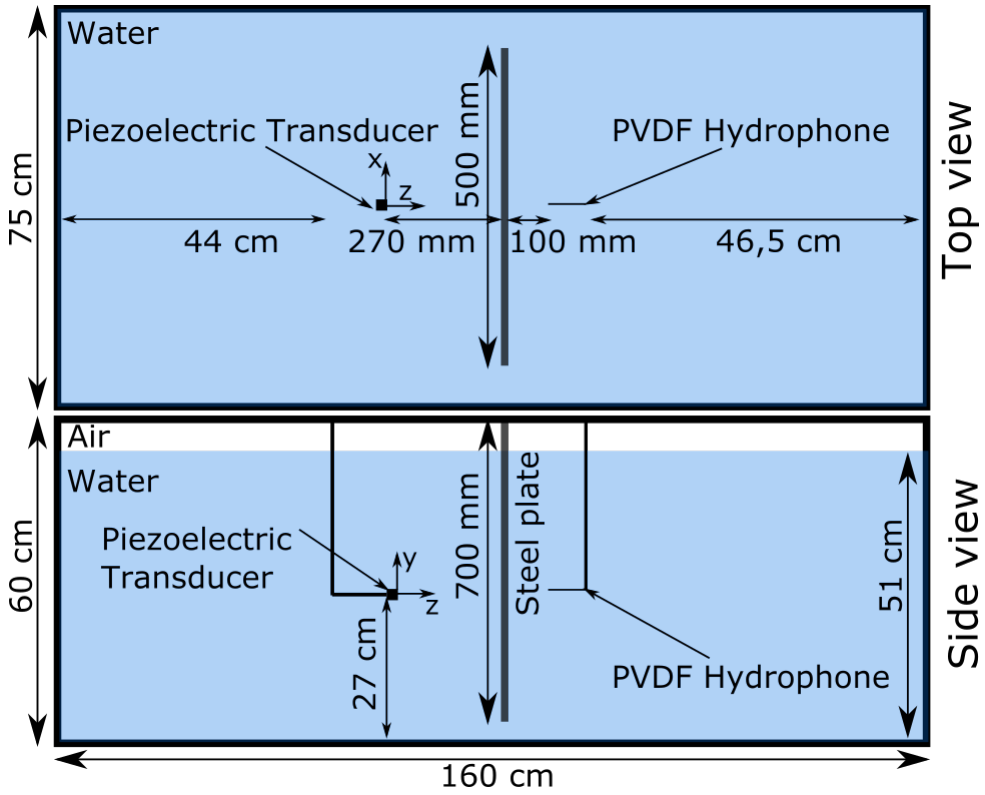

FIGURE 3.2: Schematic of the experimental setup with top and side view, the axes are oriented accordingly

In the photo Fig. 3.1 the experimental setup is shown. In Fig. 3.2 a schematic of the setup is illustrated. The experimental setup consists of a steel plate submerged in water within a tank with the dimensions measured to $height\ x\ width\ x\ length\ = 60\,x\,75\,x\,160\,cm^3$. The tank is filled to $51\,cm \pm 1\,cm$ in the y-direction. The steel plate has been measured to dimensions $6,05 \pm 0,01\,mm$ thick, $500\,mm$ wide and $700\,mm$ long [26]. The piezoelectric transducer, to the left in the photo and schematic is attached to the visible motor-stage, it is radiating towards the plate at a distance of $z_0 = 270mm$ from the plate, $440\,mm$ from the back glass and $270\,mm$ from the side glass. The transducer radiates at an incident angle of $\theta = 0°$. On the other side of the steel plate a needle hydrophone, attached to the rod seen on the right side of photo Fig. 3.1, is placed $100\,mm$ from the right side of the steel plate and $465\,mm$ from the glass wall. The total distance between the transducer and hydrophone is $z_2 = 376,05\,mm$. These distances were chosen to compare to previous work done by among other Aanes [11]. The axes are consistent with that of Ch. 2, with the origin placed in the middle of the transducer. The z-axis points towards the steel plate, the x-axis along the short length of the tank and the y-axis in the vertical direction of the tank. Measurements are made over the frequency range of 350 kHz to 1 MHz. This range is chosen to be consistent with previous work [11, 24] and the excitation of leaky Lamb modes within that range.

3.1.2 Transducer and Needle Hydrophone

The transducer used in this setup was built by Aanes during his thesis (transducer no. 3) [11]. It is a piezoelectric transducer with e piezoelectric element with thickness of $4,0\,mm$ and radius of $12,4\,mm$ [11]. The transducer was calibrated by Aanes and is intended for use in the $350\,kHz - 1\,MHz$ range.

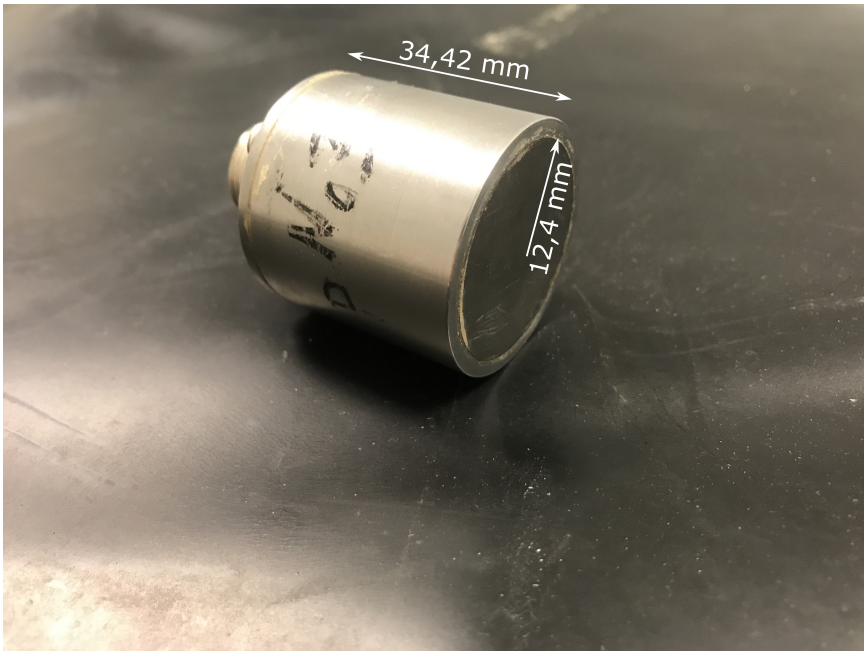

FIGURE 3.3: Photograph of the piezoelectric transducer

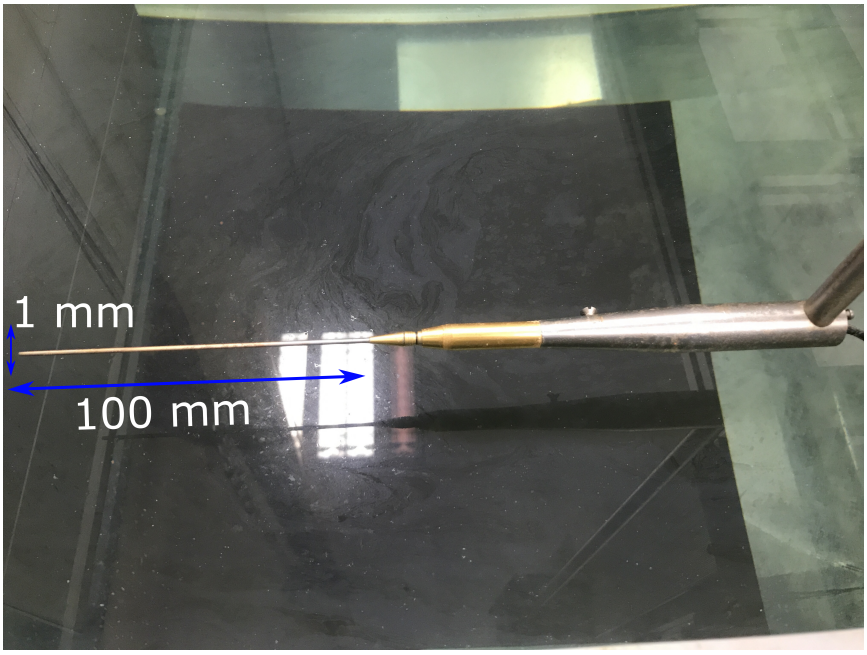

FIGURE 3.4: Photograph of PA needle hydrophone

The needle hydrophone is also the same as used by Aanes [11], Midtbø [24] and Eileraas [26]. This hydrophone was produced by Precision Acoustics Ltd. and is a PVDF needle hydrophone. It consists of a 1 mm diameter hydrophone with a 100mm probe length. The hydrophone has National Physical Laboratory (NPL) calibration as well as in-house calibration. The in-house calibration is detailed in M. Aanes' thesis [11]. Here the NPL calibration is used [36]. The hydrophone is connected with a coaxial plug and has an uncertainty of $\pm 0,8dB$ [36]. The Hydrophone is calibrated from NPL in the frequency range of 100 kHz to 1 MHz with 10kHz increments providing a level of confidence of approximately 95% [36]. In the calibration certificate it was also noted that "The tolerance on the orientation of the hydrophone relative to the direction of propagation of the incoming wave was $\pm 3^\circ$ in the horizontal plane and $\pm 3^\circ$ in the vertical plane." [36]. No other data regarding this is provided, so the actual effect of this is uncertain. Lastly the certificate from NPL also noted that the soaking time of the hydrophone was approximately 1 hour prior to use and a significantly different soaking time may affect the measured sensitivity [36].

3.1.3 Electronic Transmission and Measurement Components

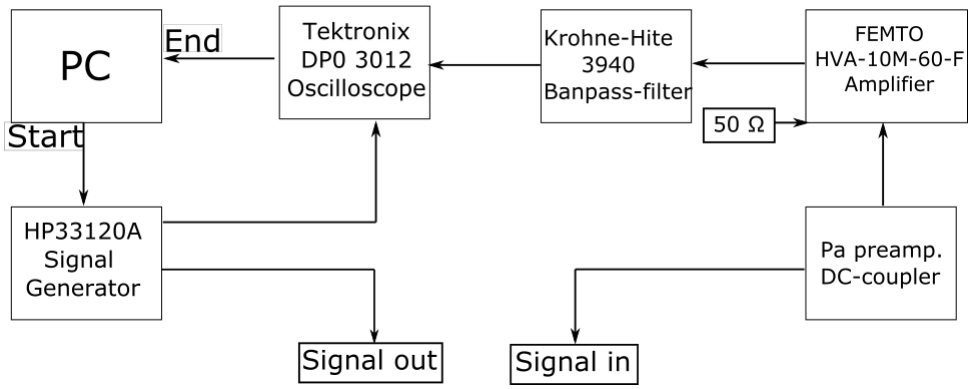

FIGURE 3.5: Illustration of electrical components and their connections

In Fig 3.5 an illustration of the electrical components used in the measurements is shown. The computer controlled signal generator, HP33120A, generates a sinusoidal signal. It is set up to supply a 10 V peak-to-peak sine burst of 130 μs duration with a burst rate of 50 Hz. It also triggers the oscilloscope. It transmits the resulting waveform to the piezoelectric transducer. The signal is then radiated from the transducer and picked up by the needle hydrophone. The hydrophone is connected to a pre-amplifier, PA110078, and DC coupler, DCPS223 (Precision Acoustics Ltd.). The signal is terminated with 50 Ω in parallel with an amplifier, HVA-10M-60-F (Precision Acoustics Ltd.) with an input impedance of 1 $M\Omega$ and an amplifier gain of around 46 dB [11]. This gain is used for all frequencies, as Aanes found that the frequency response of the amplification factor is relatively flat in the frequency range, 350 kHz to 1 MHZ [11]. The amplifier is connected through a coaxial cable with the DC-coupler. The signal is then filtered through a band-pass filter (200 kHz-2MHz) of the type Krohne Hite model 3940. Lastly the signal is received by the oscilloscope, Tektronix DPO 3012. The parameters of the oscilloscope such as sample frequency, average of bursts and time delay before storage are computer controlled.

3.1.4 Positioning System

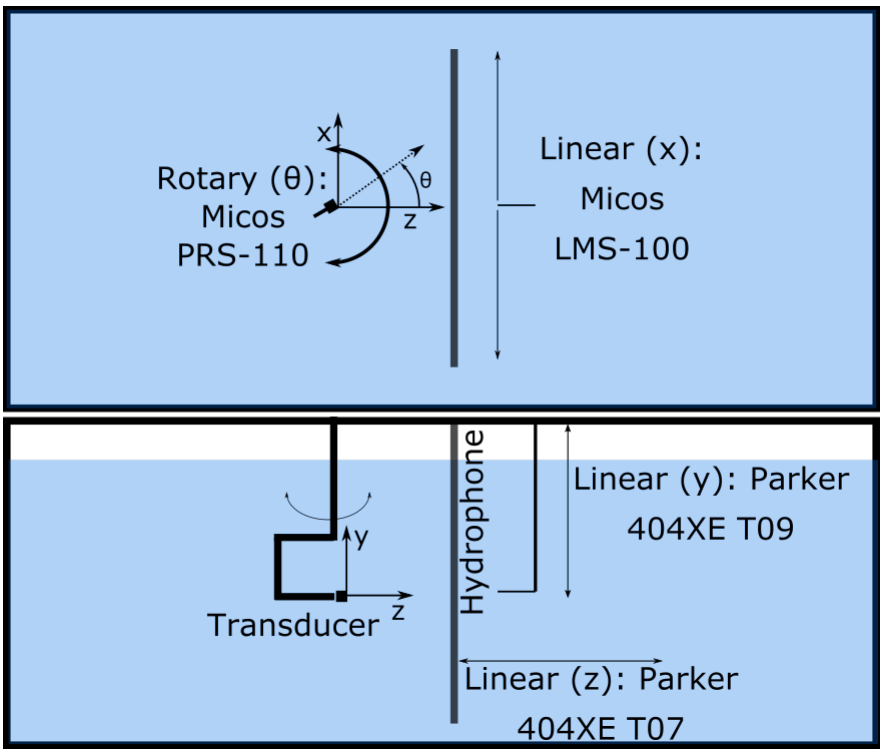

FIGURE 3.6: Illustration of motor-stages and their axes. The top part is seen from above and the bottom part is from the side.

In Fig. 3.6 the four motor-stages used in the experimental setup are depicted. The motor-stages are used to position the transducer and hydrophone. The transducer is only controlled on the rotary axis, θ. This is controlled by the Micos PRS-110 with an accuracy of $\pm 0.006^\circ$ [37]. The hydrophone is controlled by three motor-stages, one for each linear axes. The x-position is controlled by the Micos LMS-100, with an accuracy of $\pm 3 \mu m$ [37]. The range is limited by the cable connected to the motor stage, but is sufficient for the measurements. The y-position is controlled by the Parker 404XE T09 and the z-position is controlled by the Parker 404XE T07. The Parker 404XE T09 has a range of $400\,mm$ and an accuracy of $\pm 106\,\mu m$ [38]. The Parker 404XE T07 has a range of $300\,mm$ and accuracy of $90\,\mu m$ [38]. All of the motor-stages are controlled through the use of Matlab and corresponding scripts.

3.2 Experimental Setups

In this section the different experimental setups are presented. There are two pairs of measurements conducted. each of these will be presented. The x and z positions will vary in the setups, but the y-coordinate remains unchanged at $y = 0$ and is not listed as one of the variables in $p(x, z, f)$.

3.2.1 On-Axis Free Field Measurement

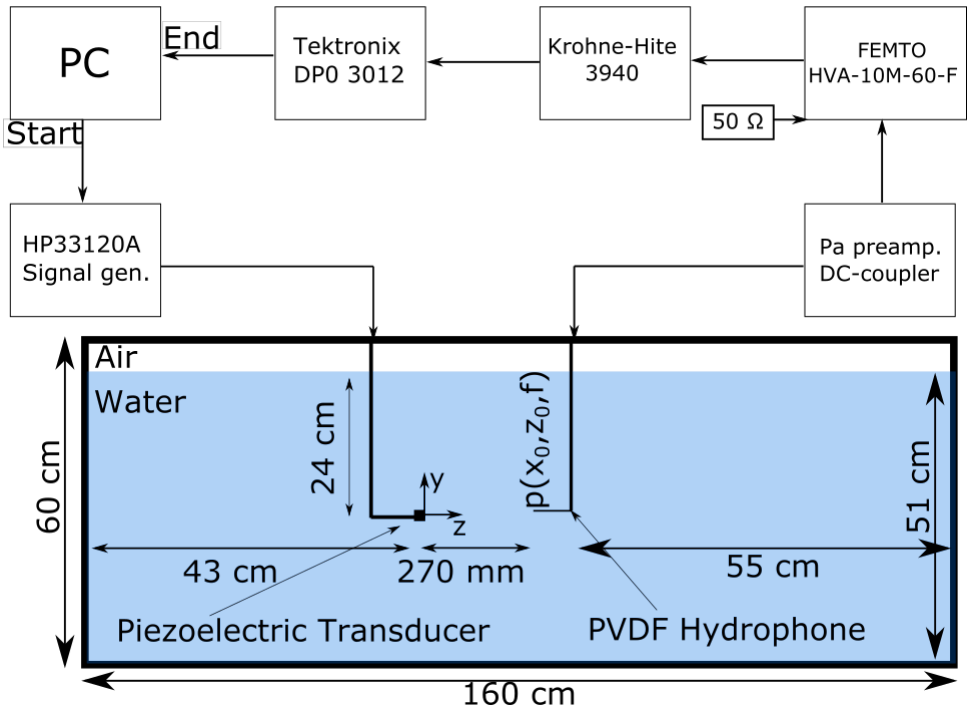

FIGURE 3.7: Illustration of on-axis free field measurement, $p(x_0, z_0, f)$. View from the side.

In this setup the pressure $p(x_0, z_0, f)$ is measured. This is one of the measurements needed in the H_{pp}-transfer function from Eq. 2.1. In Fig. 3.7 the hydrophone is placed at z-position z_0. The measurements are conducted for each frequency in the range $350\,kHz - 1\,MHz$ with $\Delta f_1 = 1kHz$. The signal is radiated as a sine wave lasting 130 μs. The measurement takes in total about an hour to conduct.

3.2.2 On-Axis Transmission Measurement

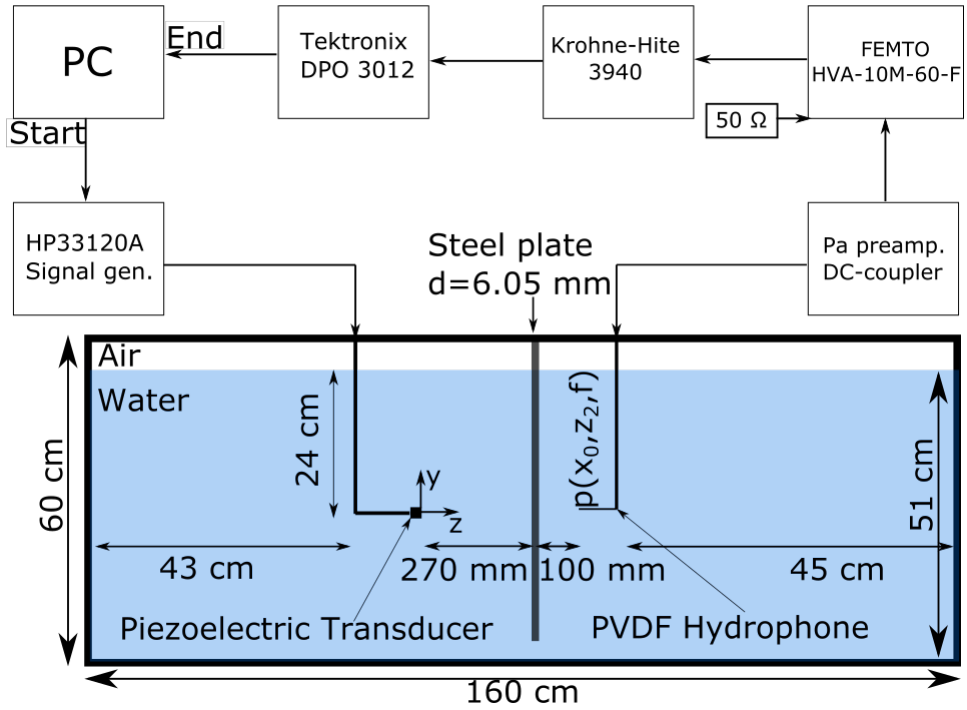

FIGURE 3.8: Illustration of on-axis transmission measurement, $p(x_0, z_2, f)$. View from the side.

In this measurement the transmitted pressure $p(x_0, z_2, f)$ is measured. With the steel plate placed at z_0 and the hydrophone $100\,mm$ behind the $6.05\,mm$ thick steel plate at position z_2. This is the second measurement used in the H_{pp} transfer function Eq. 2.1. This measurement along with the on-axis free field measurement of Sect. 3.2.1 are consistent with setups from [11, 24, 26] and results are compared with [11] in Ch. 5. The measurement is conducted for each frequency in the range $350\,kHz - 1\,MHz$ with a frequency step of $\Delta f = 1\,kHz$.

3.2.3 Transverse Free Field Measurement

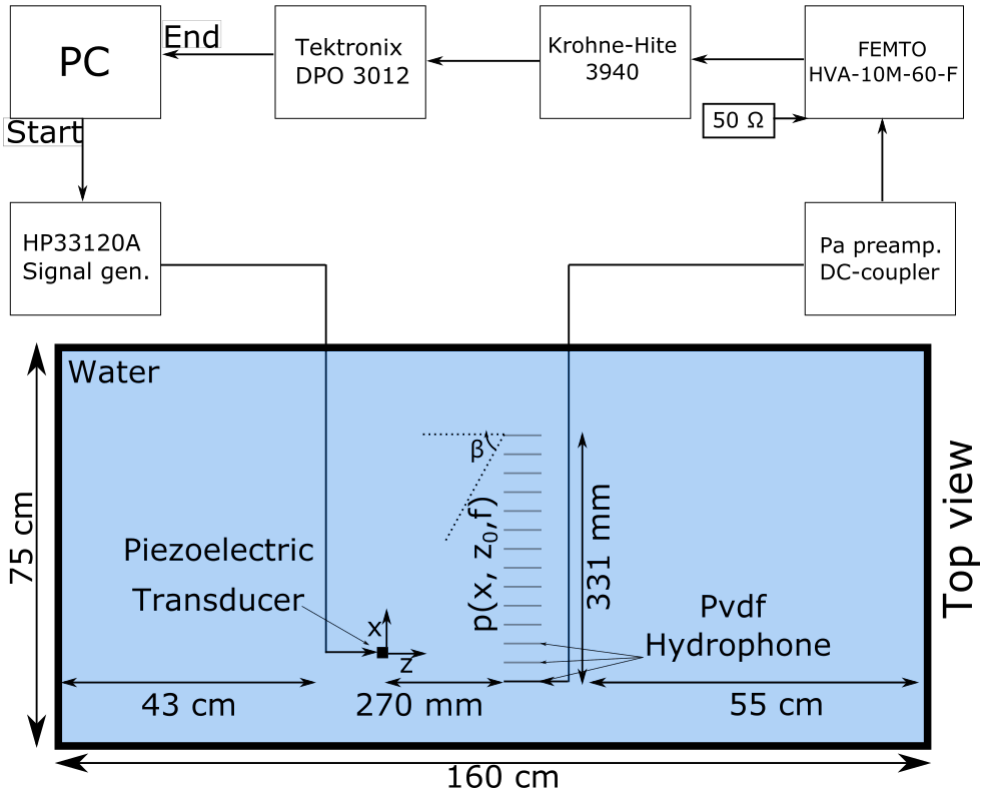

FIGURE 3.9: Illustration of transverse free field measurement, $p(x, z_0, f)$. View from top.

Fig. 3.9 shows an illustration of the transverse free field measurement, note this is from the top with the x-axis as the vertical axis. The transducer is also moved closer to one side of the tank in order to get a more expansive measurement, this means the origin is moved along the x-axis. This measurement is one part of the measurement for the transmission coefficient by measuring $p(x, z_0, f)$. Here the hydrophone traverses along the x-axis in the positive direction with a step interval $\Delta x = 1mm$. The hydrophone starts at $x_{min} = -10mm$ and moves to $x_{max} = 320mm$ with $\Delta x = 1mm$ and a total length of 331 mm. The hydrophone starts at x_{min} in order to ensure the middle of the main lobe is measured. $p(x, z_0, f)$ is measured at each x-position. The transverse movement is controlled by the Micos LMS-100 which is operated by a Matlab script which was written during this thesis for this purpose. The frequency range is still $350kHz - 1MHz$ but with a $\Delta f = 5kHz$, a larger Δf is chosen in this measurement because of time constraints. After each frequency has been measured at a x-position the script moves the hydrophone Δx. As mentioned in Sect. 3.1.2 the horizontal angle tolerance of the hydrophone is $\pm 3°$. The angle between the transducer and hydrophone is denoted β. The maximum value of β is at $x = 320mm$ with an angle of $\beta = 50°$. At this angle the measurement will be affected. With these parameters this measurement takes about 8 days. The water height in the y-direction is filled to $51cm \pm 1cm$, but as the measurement takes about 8 days up to $1cm$ water can evaporate over the course of the measurement.

3.2.4 Transverse Transmission Measurement

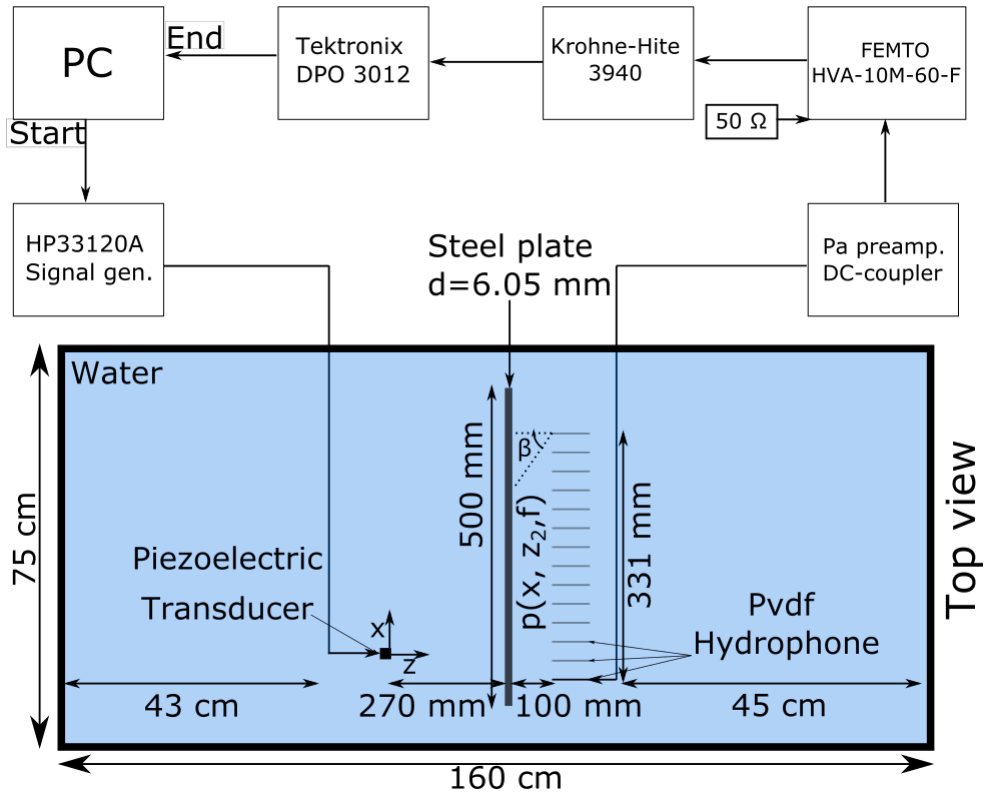

FIGURE 3.10: Illustration of transverse transmission measurement, $p(x, z_2, f)$. View from side.

Fig. 3.10 shows an illustration of the transverse transmission measurement. The plate is placed at position z_0 with the hydrophone at position z_2. The transmitted pressure, $p(x, z_2, f)$, is measured for the same frequencies and x-positions as in the free field transverse measurement of Sect. 3.2.3. This measurement along with the transverse free field measurement of Sect. 3.2.3 are used for the purpose of transformation the spatial-domain to the wavenumber-domain. The measurement takes about 8 days to finish as well.

3.2.5 Symmetrical Transverse Measurement

A second version of the transverse measurement has also been used to measure both sides of the beam. In this setup the transducer has the same position as in 3.2.1. The hydrophone starts at position $x_{min} = -210\,mm$ and traverses to $x_{max} = 210\,mm$. with a step of $\Delta x = 5mm$. This is done at both $z = z_0$ and $z = z_2$. These measurements are used in a comparison with a simulation done by Aanes shown in Fig. 5.81.

3.2.6 Transverse Measurement Numbering

The transverse measurements of Sects. 3.2.3 and 3.2.4 were first conducted only for the frequency $f = 455\,kHz$ in order to test the setup. This measurement is used further in Ch. 5 and is referred to as measurement 1. The measurements of Sects. 3.2.3 and 3.2.4 over the entire frequency range is referred to as measurement 2. The symmetrical transverse measurement of Sect. 3.2.5 is referred to as measurement 3. The differing parameters are listed in Table. 3.1

TABLE 3.1: Transverse measurements

Measurement	Frequency Range [kHz]	Δf	$x_{min}[mm]$	Δx [mm]	$x_{max}[mm]$
1	455		-10	1	320
2	350 to 1000	1	-10	1	320
3	350 to 1000	5	-210	5	210

3.3 Methods Used in Measurements

In this section the techniques used to measure the pressure field will be discussed.

3.3.1 Placement and Alignment of the Transducer and Hydrophone

The placement of the transducer is set in the z and y-direction. The transducer can only be manually moved in the $x - direction$, but can be remotely rotated around the y-axis (See Fig. 3.6). For the on-axis measurements of Sects. 3.2.1, and 3.2.2 and the symmetrical measurement of Sect. 3.2.5, the transducer is placed at a marked location for the center of the tank. For the transverse measurements of Sects. 3.2.3 and 3.2.4 the transducer is placed at a marked location $110\,mm$ in the negative x-direction. The hydrophone can move in the x, z and y directions. Along the z-axis the hydrophone is placed at either z_0 or z_2. This is achieved by measuring the distance manually with two reference rods with lengths $270\,mm$ and $100\,mm$. The $270\,mm$ rod is used to measure the z_0 position and the $100\,mm$ rod for the z_2 position. There is some uncertainty in the z-position as this placement using the reference rod is subject to human error. The exact uncertainty is hard to assert, but some deviation is expected.

3.3.2 Incident Angle of Transducer

To ensure that the incident angle θ is set to zero the hydrophone is placed at $z = 100mm$ from the transducer. Through the use of the Micos LMS-100 and Parker 404XE T07 motor-stages the peak pressure is found. Then the hydrophone is moved $200mm$ along the z-axis away from the transducer. The incident angle θ of the transducer is then adjusted so that the pressure is at the maximum again. This process is repeated until no adjustment of the transducer is needed between the two hydrophone positions.

3.3.3 Measuring Pressure

The oscilloscope uses an 8-bit resolution. The signal has a length of $130\mu s$ and the measurement is averaged over 256 bursts. The pressure $p(x, z, t)$ is measured over a $4000\mu s$ window and is sampled as the voltage output of the hydrophone, $V(x, z, t)$. As mentioned in Sect. 3.1.3 the oscilloscope is triggered by the signal generator, the time delay from when the oscilloscope begins sampling to when the signal is radiated is $1600\mu s$. 100 000 samples are taken over the $4000\mu s$ interval, this amounts to a sample frequency of 25 MHZ and a $\Delta t = 4 \cdot 10^{-8}\,s$. The samples n of the measurement are stored in array. The time-stamp t_i of each sample n is stored in a second array. The oscilloscope samples the voltage over the hydrophone and this stored as the voltage value $V(x, z, t)$. This representation of the pressure as the voltage output of the hydrophone is used throughout this thesis. The script used for the measurement can be seen in Appendix A.

3.3.4 Parameters and Variables Used in Experiments

In the following table the parameters and variable used in the measurements are presented.

TABLE 3.2: Parameters and variables of measurements

Parameter or Variable	Value or measured value	Description
f	$350\,kHz - 1\,MHz$	Frequency
Δf	$1\,kHz$	Frequency step for on-axis measurements
Δf	$5\,kHz$	Frequency step for traversing measurements
x		Horizontal position
x_0	$0\,mm$	Middle of transducer
x_{min}	$-10\,mm$	Start x-position for transverse measurements
x_{max}	$320\,mm$	End x-position for transverse measurements
Δx	$1\,mm$	Step interval along x-axis for traversing hydrophone
z_0	$270\,mm$	Free field measurement position on z-axis
z_2	$376.5\,mm$	Transmission measurement position on z-axis
$p(x_0, z_0, f)$	$V(x_0, z_0, f)$	On-axis free field pressure
$p(x_0, z_2, f)$	$V(x_0, z_2, f)$	On-axis transmitted pressure
$p(x, z_0, f)$	$V(x, z_0, f)$	Free field pressure at position (x, z_0)
$p(x, z_2, f)$	$V(x, z_2, f)$	Transmitted pressure at position (x, z_2)
θ	0°	Incident angle of transducer from the z-axis
β		Angle between transducer and hydrophone
t_{min}	$-1600\mu s$	Start of sampling
t_{max}	$2400\mu s$	End of sampling
Δt	$4 \cdot 10^{-8} s$	Temporal sampling step
Signal length	$130\mu s$	Length av radiated signal
Sample window	$4000\,\mu s$	Length of sample interval
Time-stamp	t_i	Time of measurement of each sample
Samples, n	100 000	Samples taken over sample window
Sampling frequency	$25\,MHz$	Frequency of sampling over sampling window
Average	256	Number of measurements averaged over
Burst rate	$50\,Hz$	Time between bursts in Hz

3.4 Post-Processing of Data

In this section a summation of the methods used to post-process the gathered data through the measurement setups. This includes selection of post-processing window and mathematical operations applied to the data.

3.4.1 Selection of Post-Processing Window for On-Axis Measurement

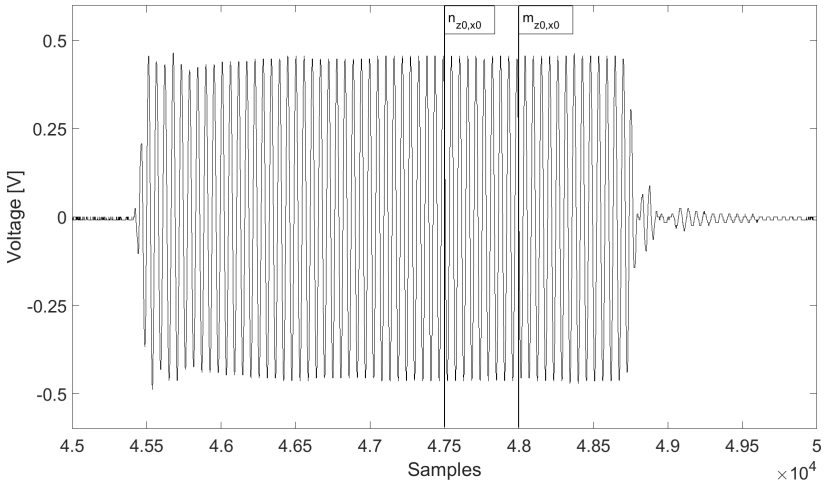

FIGURE 3.11: Example of selected post-processing window for $V(0, z_0, t)$

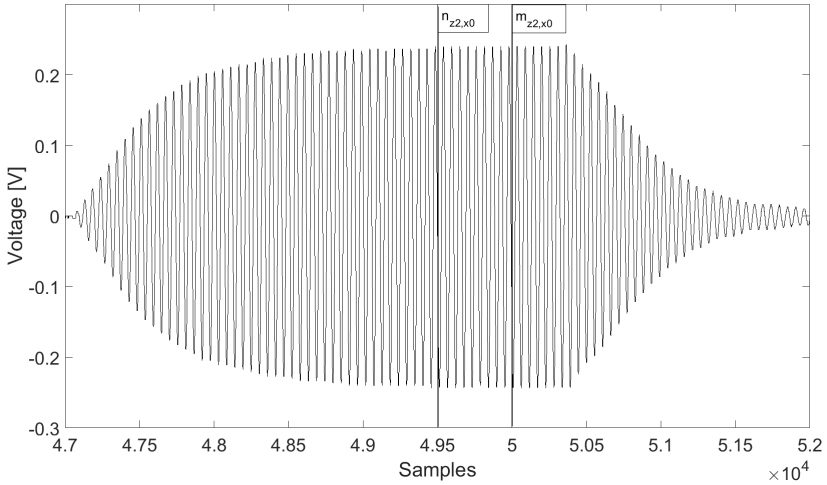

FIGURE 3.12: Example of selected post-processing window for $V(0, z_2, t)$

The post-processing window is the selected interval of samples that will be used for processing. This includes the fast Fourier transform (fft), used in Matlab. The $130\mu s$ long signal is located somewhere in the $4000\,\mu s$ long window. A post-processing window is selected manually by going into the waveform and designating a start sample, $n_{z,x}$, and end sample $m_{z,x}$. Here z, x denotes the position of the hydrophone. For the on-axis measurement they are denoted n_{z_0,x_0}, m_{z_0,x_0} n_{z_2,x_0} and m_{z_2,x_0}. The

number of samples in the post-processing window is 5000. This selection is seen in Figs. 3.11 and 3.12, where the interval between sample $n_{z,x}$ and sample $m_{z,x}$ is the designated post-processing window for the z_0 and z_2 measurements. The designation is done for the frequency $455kHz$ because of its vicinity to a leaky Lamb mode in the transmission measurement. The vicinity to a leaky Lamb mode is favourable as the signal is strongest here, and easiest to have clear signal. This post-processing window is then used for all the other frequencies measured.

3.4.2 Selection of Post-Processing Window for Transverse Measurements

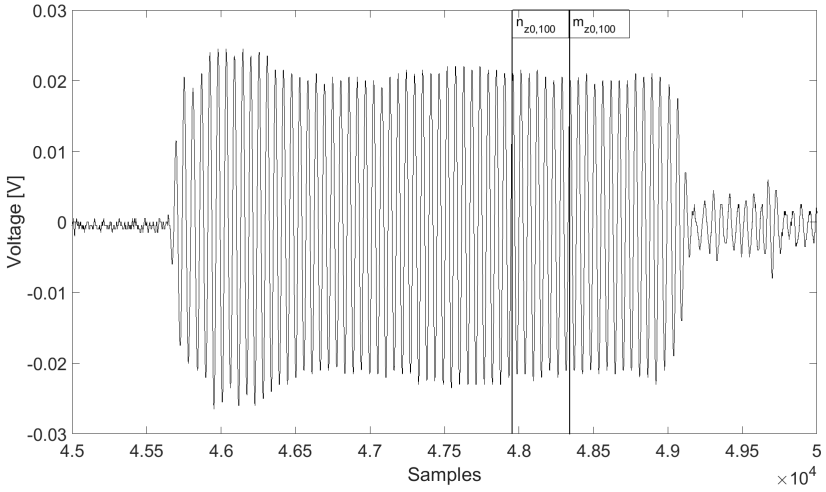

FIGURE 3.13: Calculated steady state region for $V(100mm, z_0, t)$

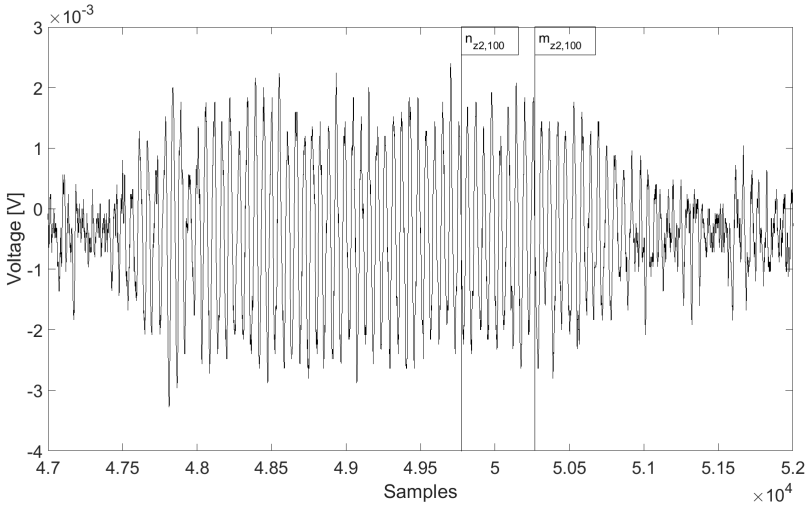

FIGURE 3.14: Calculated steady state region for $V(100mm, z_2, t)$

In order to select a post-processing window for the transverse measurements a different approach than the one for the on-axis measurement is needed. Because the hydrophone moves further away from the transducer the signal position within the sample window changes. Therefore a calculation is implemented, using the sound

velocity and the Pythagorean theorem, to account for the shift in position. At position z_0 the fluid velocity of water is used c_f. At position z_2 an approximate velocity c_a is used. This velocity is an average of the velocity the sound travels from the transducer to position (x_0, z_2), this is found using an average time of arrival (TOA) of the z_2 measurements and is set to $c_a = 1515\,m/s$. A post-processing window is selected as seen in previous section, in Figs. 3.11 and 3.12, for the measurement at $x = 0$, where sample n_{z,x_0} and sample m_{z,x_0} are designated, containing 5000 samples. Afterwards a post-processing window is calculated for each previous and subsequent x positions, $n_{z,-9}$, $n_{z,-8}$... $n_{z,320}$. This is done for both z_0 and z_2. In Figs. 3.13 and 3.14 the calculated post-processing windows are shown at position $x = 100mm$ for the z_0 and z_2 measurements respectively.

3.4.3 Temporal DFT - Voltage Spectrum

The sampled voltage from each measurement are given as a function of time, $V(x, z, t)$. For any further use they are needed as a function of frequency $V(x, z, f)$. Here the temporal DFT from Eq. 2.61 is utilized. Matlab has a built in version of this DFT called Fast Fourier Transform (fft) this function is utilized on the post-processing windows discussed in Sect. 3.4.1 and 3.4.2. Each individual post-processing window is transformed. Once a post-processing window has been transformed to the frequency domain the maximum voltage from that measurement is stored as a complex number, comprised of the amplitude and phase, in a x by f array for further processing. This is done for position z_0 and z_2, resulting in two arrays. The resulting voltage spectra are denoted $V(x, z, f)$. A distinction between the the post-processing windows for the on-axis and transverse measurements is made because of characteristics of the signals. The on-axis $n_{z,x}$ and $m_{z,x}$ are adjusted by a Matlab script in order for the post-processing window to start and end at peaks of the signal. This script does however not work on the transverse measurements because of the distortion of the signal further out along the x-axis. The post-processing window is therefore used from the exact $n_{z,x}$ and $m_{z,x}$ values, meaning there occurs sampling effects because the selection of $n_{z,x}$ and $m_{z,x}$ is somewhat arbitrary. This could possibly have been remedied but because of circumstances discussed in 6 this was not accomplished.

3.4.4 Accounting for Phase

As explained in Sect. 3.4.2 the post-processing window for the transverse measurement is determined by manually asserting the window and then using an approximation to assert it in subsequent x-positions. To account for the discrepancy in phase a baseline time is used. The measurement is triggered by the signal generator so this time stamp is used as a reference for the phase. This is employed using equation

$$V(x, z, f) = max(V(x, z, f))e^{i\angle(V(x,z,f))-i\omega t_n}. \tag{3.1}$$

Where t_n is the time stamp of the first sample, $n_{z,x}$, of the post-processing window. The maximum amplitude of $V(x, z, f)$ is multiplied by the phase of the fft and the phase at t_n. This is done for each cell in the x by f array. Through this the discrepancy between the post-processing windows can be accounted for.

3.4.5 Pressure-to-Pressure Transfer Function

The H_{pp} transfer function is described by Eq. 2.1. The pressure is represented by the voltage output of hydrophone, $V(x,z,f)$. Therefore the equation is given as

$$H_{pp}(x,z_2,f) = \frac{V(x,z_2,f)}{V(x_0,z_0,f)}. \tag{3.2}$$

Here $V(x,z_2,f)$ represents the transmitted pressure. This is either obtained from the on-axis transmission measurement of Sect. 3.2.2, or the transmission measurement from measurement 3 of Sect. 3.2.5. These results are Fourier transformed from the temporal to the frequency domain before utilized. $V(x_0,z_0,f)$ is the on axis free field voltage. This is either obtained from the on-axis free field measurement of Sect. 3.2.1, or the x_0-position of the free field measurement from measurement 3 of Sect. 3.2.5. These results are also Fourier transformed from the temporal to the frequency domain before utilized. The calculation is performed for each frequency. This means for the on-axis results that each cell from the z_2-array corresponding to a frequency is divided by the corresponding cell in the z_0-array. For the symmetrical transverse measurement each row in the z_2-array for a given frequency is divided by the x_0-value at that given frequency from the z_0-array.

3.4.6 Resolution and Extent

The four parameters that are crucial for the Hankel transform from Eq. 2.62 are Δx, x_{max}, Δh_x and $h_{x,max}$. The term resolution refers to the step interval in a domain and the term extent refers to the maximum value in a domain. The relation is given as [32]

$$\frac{2\pi}{N} = \Delta x \Delta h_x \tag{3.3}$$

Where N is the number of spatial samples, Δx is the spatial resolution and Δh_x is the horizontal wavenumber resolution. Assuming the pressure maximum for the transverse measurement is at $x = 0$ the extent of x is $x_{max} = 320\,mm$ and a spatial resolution of $\Delta x = 1\,mm$. This results in an extent in the wavenumber domain of $h_{x,max} = 6283.2\,rad/m$ and wavenumber resolution of $\Delta h_x = 19.6\,rad/m$.

3.4.7 Hankel Transformation - Voltage Wavenumber Spectrum

The next part of the post processing is to transform the arrays discussed in Sect. 3.4.3 from the spatial domain, x-domain, to the wavenumber domain, h_x-domain. To do this the Hankel transformation is utilized. Before the Hankel transformation is utilized some characteristics of the voltage spectrum are needed. The x-value of the maximum measured voltage for $f = 455\,kHz$ is found. This x-value is manually assigned as x_0 for all $V(x,z,f)$, making x_{max} dependant on x_0. The Hankel transform is given in Eq. 2.62. The pressure spectrum is however represented as a voltage spectrum, giving the Hankel transformation as

$$V_M(h_x,z,f) = \frac{1}{2\pi}\int_0^\infty V(x,z,f) J_0(\eta x) h_x dh_x. \tag{3.4}$$

Where $V(x,z,f)$ is the complex valued pressure spectrum component found from Sect. 3.4.3 with the phase adjustment of Sect. 3.4.4. To solve this integral a trapezoidal numerical integration method is utilized. The limits of which are from x_0 to

x_{max}. $V_M(h_x, z, f)$ is then calculated for each horizontal wavenumber at frequency f. The values of h_x are given in Sect. 3.4.6, if it is assumed the voltage maximum is measured at $x = 0$. Each frequency row of the x by f array is transformed resulting in the a new array for the voltage wavenumber spectrum, h_x by f. This is done for the z_0 and z_2 positions, resulting in two new arrays. Each cell in the arrays corresponding to a value of $V_M(h_x, z_0, f)$ or $V_M(h_x, z_2, f)$ depending on the array. The cells containing the amplitude and phase.

3.4.8 Calculating the Transmission Coefficient

Using Eq. 2.60 the transmission coefficient can be calculated from the the measured wavenumber pressure spectra, $V_M(h_x, z_0, f)$ and $V_M(h_x, z_2, f)$. The transmission coefficient in Eq. 2.60 is defined for functions of pressure, but as the measured pressure is given as voltage the equation for the transmission coefficient is defined as

$$T_M(h_x, d, f) = \frac{V_M(h_x, z_2, f)}{V_M(h_x, z_0, f)e^{ih_{f,z}(z_2 - z_0 - d)}}. \tag{3.5}$$

Each cell from the z_2 array is divided by plane-wave propagation term and the corresponding cell from the z_0 array. The corresponding cell being the cell with the same h_x and f values. The calculation giving the transmission coefficient $T_M(h_x, d, f)$.

3.4.9 Post-Processing Parameters and Variables

In Tbl. 3.3 the different variables and parameters of the post-processing methods are collected. The implementation of the post-processing methods can be seen in Appendix. B and Appendix. D.

TABLE 3.3: Parameters and variables of measurements

Parameter or Variable	Value	Description
$n_{z,x}$		First selected sample of post-processing window where z, x denote position of hydrophone
$m_{z,x}$		Last selected sample of post-processing window where z, x are the position of the hydrophone
n	5000	number of temporal samples
c_f	$1485\,m/s$	Fluid velocity
c_a	$1515\,m/s$	Average velocity of transmitted beam
$V(x, z, t)$		Sampled voltage in interval
t_n		Time-stamps of first selected and calculated samples
x_0		Position of maximum voltage
x_{max}		Spatial extent
Δx		Spatial step interval, wavenumber resolution
$h_{x,min}$	$0 rad/m$	Minimum wavenumber
$h_{x,max}$		Wavenumber extent, dependant on Δx
Δh_x		Wavenumber resolution, dependant on x_{max}

Chapter 4

Simulation Setup and Method

In This chapter the simulation using the ASM will be discussed, including methods used for further processing. Sect. 4.1 presents the Simulation parameters and variables. In Sect. 4.2 the use of the simulation and its results are discussed. This includes the directly calculated pressure wavenumber spectrum and transmission coefficient in Sect. 4.2.1. The simulated pressure spectra in Sect. 4.2.2. The post-processing of the pressure spectrum which includes the Hankel transformation to the pressure wavenumber spectrum in Sect. 4.2.3. The transmission coefficient calculated from these transformed pressure wavenumber spectrum is discussed in Sect. 3.4.8. Lastly the the simulation used to verify the post-processing method is presented in Sect. 4.2.5.

4.1 ASM Simulation

The implementation of the ASM model is done in Matlab, using the equations from Sect. 2.4. ASM is used both to compare with experimental results, but also verify and test the post processing methods used on the experimental results. The ASM model simulates a baffled piston of radius $a = 10.55mm$. This is the effective radius of the simulated FEM transducer in Aanes' thesis [11] which is based on physical transducer used in the measurements when adjusted to the frequency of maximum source sensitivity of $f = 575\,kHz$. This relationship is given by

$$a = \frac{1.6137}{h_f sin\theta_{-3dB}} \tag{4.1}$$

Where θ_{-3dB} is the -3dB angle of the transducer. This radius is consistent with the baffled piston simulations done previously [24, 26]. The piston is simulated radiating waves into a fluid at normal incidence, $\theta = 0$. A steel plate is $270\,mm$ from the piston face. The steel plate has a thickness of $6.05\,mm$. Finally the signal is transmitted into the fluid on the other side of the plate. As discussed in section 2.4, ASM calculates first the pressure as a function of η_r and f, then uses an inverse Hankel transform to get the pressure as a function of r and f. The pressure is calculated at the front face of the plate $270\,mm$ from the transducer, z_0. Then at the receiver point $100\,mm$ behind the steel plate, z_2. Although not as accurate in regards to the measurement as a FEM simulation with a simulated transducer as in Aanes' thesis [11], the time needed to implement and run a simulation in ASM is favourable. The script for the implementation of the model can be seen in Appendix C.

4.1.1 Determining Parameters and Variables

The parameters and variables used in the simulation chosen to match the experimental setups described in Sects. 3.2.3 and 3.2.4. The values are consistent with previous work [27, 24, 11, 26]. The first part of the ASM simulation is simulating the wavenumber pressure spectra $P(\eta_r, z_0, f)$ and $P(\eta_r, z_2, f)$. The determining variables here is η_r and the maximum value desired, $\eta_{r,max}$. $\eta_{r,max}$ is chosen so that it will include the relationship $h_f = \eta_r$, which is where the waves become evanescent. The requirement for $\eta_{r,max}$ is that the angular spectrum is truncated when the evanescent part is negligible. Therefore $\eta_{r,max}$ must be greater than the fluid-wavenumber of $f = 1000\,kHz$, which is $4231\,rad/m$, so $\eta_{r,max} = 4250\,rad/m$. This value could have been variable for each frequency, but this aspect was overlooked. $\eta_{r,min} = 0$. The next variable to consider is the step interval $\Delta\eta_r$. The consideration here is the relationship to $r_{max} = 320\,mm$, as $x_{max} = 320\,mm$ is Sect. 3.9 and 3.2.4. The relationship is given by [32]

$$\frac{2\pi}{N} = \Delta r \Delta \eta_r. \tag{4.2}$$

$\Delta r = 1\,mm$ in order to match $\Delta x = 1\,mm$ in the experimental setups of Sects. 3.9 and 3.2.4. $\Delta\eta_r = 1 \cdot 10^{-3}\,rad/m$ is chosen in order to have an accurate model of $P(\eta_r, z, f)$. This results in $N = 4250001$ number of samples. As stated in Sect. 2.4.1 at the value $\eta_r = h_f$ a singularity occurs in $P(\eta_r, z_0, f)$, because of the inverse proportionality with $h_{f,z}$, which becomes zero. This is solved by sampling very rapidly close to the value but not the value itself. This second sampling step is set to $\Delta\eta_{r,2} = 1.33 \cdot 10^{-8}\,rad/m$, this was chosen through trial and error. This sampling step is utilized in the interval $(\eta_r = h_f) - 0.01\,rad/m + \Delta\eta_r\,to\,(\eta_r = h_f) + 0.01\,rad/m - \Delta\eta_r$. The number of samples N is now a summation of the three η_r-intervals. Before $\eta_r = h_f$, near $\eta_r = h_f$ and after $\eta_r = h_f$. The total of samples add up to $N_2 = 5753739$ samples. This is however only used for the transformation and is not stored in an array. The stored array has the same number of samples as $P(\eta_r, z_2, f)$, $N = 4250001$. The distances in the z-direction are the same as in the experiment. The upper face of the plate at $z_0 = 270\,mm$. The plate thickness is set to $d = 6.05\,mm$, the same as the thickness in the experiments. The distance from the lower face of the plate is $100\,mm$ so that $z_2 = z_0 + d + 100\,mm = 376.05\,mm$. The same frequency interval as in the experimental setup is used here with a $f_{min} = 350\,kHz$ and $f_{max} = 1\,MHz$. The frequency step is chosen to be $\Delta f = 5\,kHz$ as in the experimental setups of Sects. 3.9 and 3.2.4. Next are the physical parameters needed, here the same parameters used in previous simulations are used [11, 24, 26]. The fluid density is set to $\rho_f = 1000\,kg/m^3$ and plate density to $\rho_p = 8000\,kg/m^3$. The sound velocity in the fluid is set to $c_f = 1485\,m/s$, the compressional velocity in the plate is set to $c_l = 5780\,m/s$ and the shear velocity in the plate is set to $c_s = 3130\,m/s$. Finally the particle velocity on the piston face is set to $v_0 = 1\,m/s$ as this has been the utilized in [24, 26]. All these values are given in Tbl. 4.1

TABLE 4.1: Variables and parameters of ASM model

Variable or parameter	value	Description
$\eta_{r,min}$	$0\,rad/m$	Minimum Horizontal wavenumber
$\eta_{r,max}$	$4250\,rad/m$	Maximum horizontal wavenumber
$\Delta\eta_r$	$1 \cdot 10^{-3}\,rad/m$	Main wavenumber step
$\Delta\eta_{r,2}$	$1.33 \cdot 10^{-8}$	Secondary wavenumber step
f_{min}	$350\,kHz$	Minimum frequency
f_{max}	$1\,MHz$	Maximum frequency
Δf	$5\,kHz$	Frequency step
c_f	$1485\,m/s$	Fluid velocity
c_l	$5780\,m/s$	Compressional velocity in steel
c_s	$3130\,m/s$	Shear velocity in steel
ρ_f	$1000\,kg/m^3$	Fluid density water
ρ_p	$8000\,kg/m^3$	Density steel
v_0	$1m/s$	Particle velocity piston face
a	$10.55\,mm$	Piston Diameter
z_0	$270mm$	Distance from piston to plate
d	$6.05\,mm$	Thickness of plate
z_2	$376.05\,mm$	Distance from steel plate and receiver
r_{min}	$0\,mm$	Start of simulated pressure field
r_{max}	$320\,mm$	End of simulated pressure field
Δr	$1\,mm$	radial step
N	42500001	Number of samples

4.2 Use of ASM

In this section the use of ASM will be discussed. The main simulation of $P(\eta_r, z, f)$ and $p(r, z, f)$ but also other uses such as comparing post-processing methods utilized for the physical measurements detailed in Sect. 3.4.

4.2.1 Directly Calculated Pressure Wavenumber Spectra and Transmission Coefficient

The first part of the ASM simulation, as mentioned previously, calculates the pressure as a function of the η_r and f, $P(\eta_r, z, f)$. They are calculated from Eqs. 2.56 and 2.57. These pressure wavenumber spectra can be used to compare with the ones obtained from the transverse measurements of Sects. 3.2.3 and 3.2.4 and are denoted P_D. In addition the transmission coefficient used in the calculation, described in Eq. 2.48, can be compared with the measured one. This equation is given in Cartesian coordinates, but is used here with the cylindrical coordinates used in ASM. The transmission coefficient used in the simulation is denoted $|T_D|$

4.2.2 Simulated Pressure Spectra

The second part of the ASM simulation is the simulated pressure spectra, $p(r, z_0, f)$ and $p(r, z_2, f)$, denoted p_r. These are calculated using the Eqs. 2.58 and 2.59. A trapezoidal integration method is used. The integration limit is set by the vector η_r. The pressure spectra components can be used to compare with the measured

voltage spectra components described in Sect. 3.4.3 and are used in the further post-processing simulation.

4.2.3 Post-processing of Pressure Spectrum

This step in the ASM-simulation is used to simulate the methods used in Sect. 3.4.7. The simulated pressure spectrum, $p_r(r, z, f)$, from Sect. 4.2.2 is utilized in the same manner as the voltage spectra $V(x, z, f)$ from the the Sect 3.4.3. The Hankel transformation from Eq. 2.62 is used to transform the simulated pressure spectra to the wavenumber domain again. Here the Hankel transformation is a function of r and η_r. A trapezoidal integration is utilized with the limit being the r-vector of the pressure spectrum. This means the new pressure wavenumber spectra are subject to the same restraints as the measurements in regards to r_{max} and Δr. With these variables the extent can be up to $\eta_{r,max} = 6283.3 rad/m$, but is set to $\eta_{r,max} = 4300\, rad/m$ as this is deemed sufficient. The resolution can be be set to to $\Delta\eta_r = 19.6$ and is rounded up to $\Delta\eta_r = 20 rad/m$. The same method as in 3.4.7 is utilized. These pressure wavenumber spectra are denoted P_H. The parameters of the Hankel transformation are given in Table. 4.2.

TABLE 4.2: Variables and parameters of Hankel transformation

Variable or parameter	value	Description
r_{max}	$320\, mm$	Extent of pressure spectrum in r-domain
r_{min}	$0\, mm$	Minimum r-value
Δr	$1\, mm$	Spatial resolution
$\eta_{r,max}$	$4300\, rad/m$	Extent in wavenumber domain
$\eta_{r,min}$	$0\, rad/m$	Minimum in wavenumber domain
$\Delta\eta_r$	$20\, rad/m$	Resolution in wavenumber domain

4.2.4 Pressure Calculated Transmission Coefficient

Using the Hankel transformed pressure wavenumber spectra P_H the transmission coefficient can again be calculated using Eq. 2.60 as in Sect 3.4.8, denoted T_H. This transmission coefficient can show what effect the reduction of resolution and extent of the spatial samples from the pressure spectrum $p(r, z, f)$ will have on the reconstruction of the transmission coefficient.

4.2.5 Post-Processing Verification

To verify that the transformation is implemented correctly a second simulation is conducted, but utilizing a larger r_{max}. In this simulation the $r_{max} = 63.5m$ resulting in a $\Delta\eta_r = 0.1\, rad/m$. Due to the size of this simulation it is only conducted for the frequency $f = 455\, kHz$. The differing parameters of the Hankel transformation used in this simulation are given in Table. 4.3. The rest of the variables and parameters are given in Table. 4.1.

TABLE 4.3: Variables and parameters of Hankel transformation

Variable or parameter	value	Description
r_{max}	63.5 mm	Extent of pressure spectrum in r-domain
r_{min}	0 mm	Minimum r-value
Δr	1 mm	Spatial resolution
$\eta_{r,max}$	4300 rad/m	Extent in wavenumber domain
$\eta_{r,min}$	0 rad/m	Minimum in wavenumber domain
$\Delta\eta_r$	0.01 rad/m	Resolution in wavenumber domain

Chapter 5

Results and Discussion

In this chapter the results from the simulations and experiments will be presented and discussed. First the results will be presented individually and later on compared. In Sect. 5.1 the results from the ASM simulation will be presented. This includes the direct calculation of the transmission coefficient in Sect. 5.1.1 and the pressure wavenumber spectra in Sect. 5.1.2. Next the pressure spectra are presented in Sect. 5.1.3. Further the results from the simulated post-processing are presented in Sects. 5.1.4 where the method of post-processing is tested, and in Sect. 5.1.5 the effects of limited spatial extent and resolution are presented. Following the ASM results, the measurement results are presented. Firstly the results from the on axis measurements. Sect. 5.2.1 presents the sampled data and Sect. 5.2.2 presents the processed data results with comparison to previous work. Following this the results from the transverse measurements are presented in Sects. 5.3 with the sampled data presented in Sect. 5.3.1. In Sect. 5.3.2 the results from the post-processed symmetrical transverse measurement with comparison to previous work are shown. Sect. 5.3.3 presents the the voltage spectra results from the transverse measurements. Sect. 5.3.4 presents the voltage wavenumber spectra results from the measurements and Sect. 5.3.5 presents the measured results for the transmission coefficient. Lastly the comparison and discussion of the two sets of results are presented in Sect. 5.4 followed by some final thoughts in Sect. 5.5.

Unfortunately the processing of the sampled intervals $V(x, z, t)$ from the transverse measurements, specifically the assignment of start and end sample of post-processing window, resulted in the phase component being nonsensical. Because of this the results will focus on the magnitude of measurements and simulations.

5.1 ASM Simulations

In this section the results from the ASM simulation detailed in Ch. 4 will be presented. The results will be presented in the order they are in the simulation process, starting at the directly calculated wavenumber spectra and transmission coefficient. Following this the verification of the Hankel transformation. Lastly the results from the simulation with limited spatial resolution and extent is shown. The spectra will be shown at three different frequencies $f = 455\,kHz$, $f = 700\,kHz$ and $f = 955\,kHz$. These three frequencies are chosen as they represent three different intervals of transmission through the plate. $f = 455\,kHz$ is in close vicinity to S_{-2} leaky Lamb mode at normal incidence, $f = 700\,kHz$ is not in the vicinity of mode and therefore represents a minimum in transmission and $f = 955kHz$ is close to the A_3 mode at normal incidence. All the variables and parameters of the simulation are found in Table. 4.1

5.1.1 Direct Calculation of Transmission Coefficient

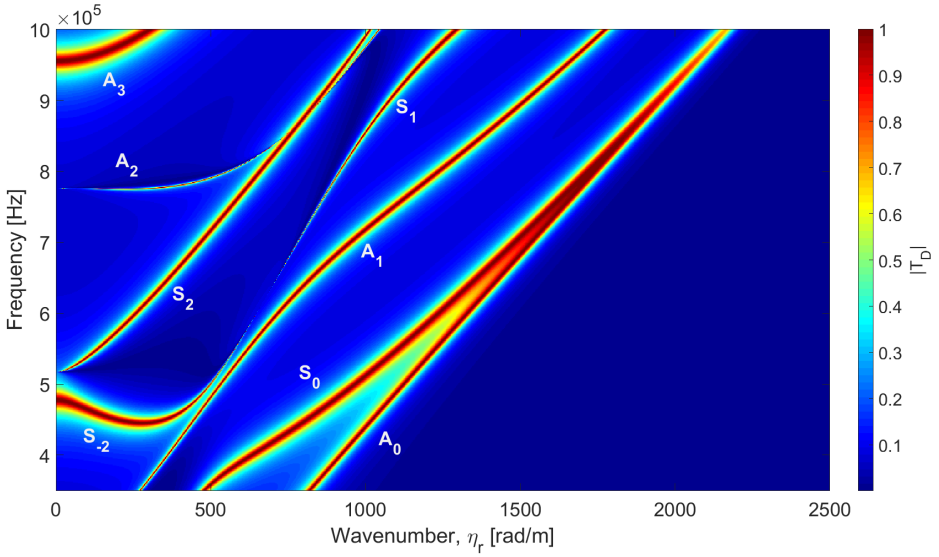

FIGURE 5.1: Directly calculated transmission coefficient $|T_D|$ with labeled leaky Lamb modes

The magnitude of the directly calculated transmission coefficient T_D is plotted in Fig. 5.1. The horizontal axis shows η_r and the frequency f along the vertical axis. The figure shows the magnitude of the transmission coefficient as a function of η_r and f, with the colour denoting the value of $|T_D|$. Along with the magnitude of T_D the leaky Lamb modes have been labeled consistent with [11], except for the S_{-2} mode which is consistent with [14]. $|T_D|$ is calculated using equation 2.48.

5.1.2 Direct Calculation of the Pressure Wavenumber Spectra and Transmission Coefficient Components

As detailed in Sect. 4.2.1 the first part of the ASM simulation calculates the pressure wavenumber spectra, $P_D(\eta_r, z, f)$ and the transmission coefficient $T_D(\eta_r, f)$. Because these spectra are calculated directly they represent the theoretically correct values.

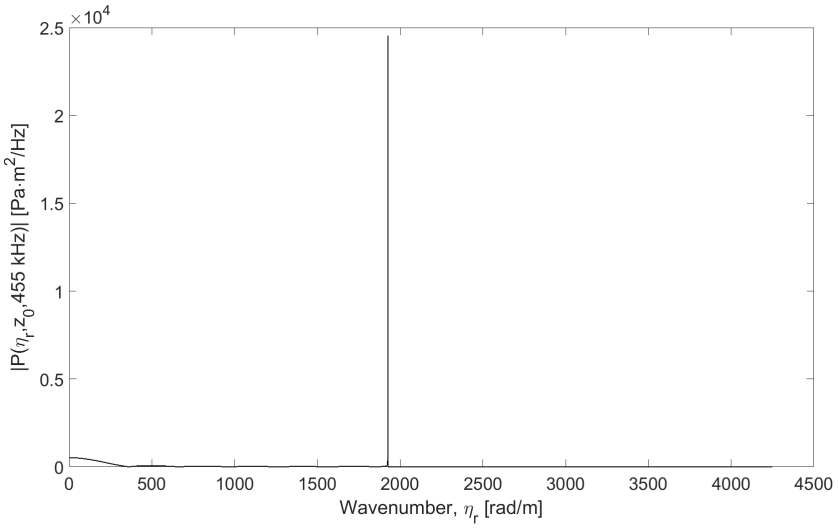

FIGURE 5.2: Directly calculated magnitude of the pressure wavenumber spectrum $P_D(\eta_r, z_0, 455kHz)$

Fig. 5.2 shows the directly calculated magnitude of the wavenumber spectrum for $|P_D(\eta_r, z_0, 455kHz)|$. The figure has the horizontal wavenumber η_r along the horizontal axis and the magnitude $|P(\eta_r, z_0, 455\,kHz)|[Pa/Hz][m^2]$ along the vertical axis. The clearest peak is at $\eta_r = 1925.2\,rad/m$. This is consistent with what is discussed in Sect. 4.1.1 where $\eta_r = h_f$ results in a singularity. For $f = 455\,kHz$ $h_f = 1925.2\,rad/m$. With the region beyond $\eta_r = h_f$ being the evanescent region.

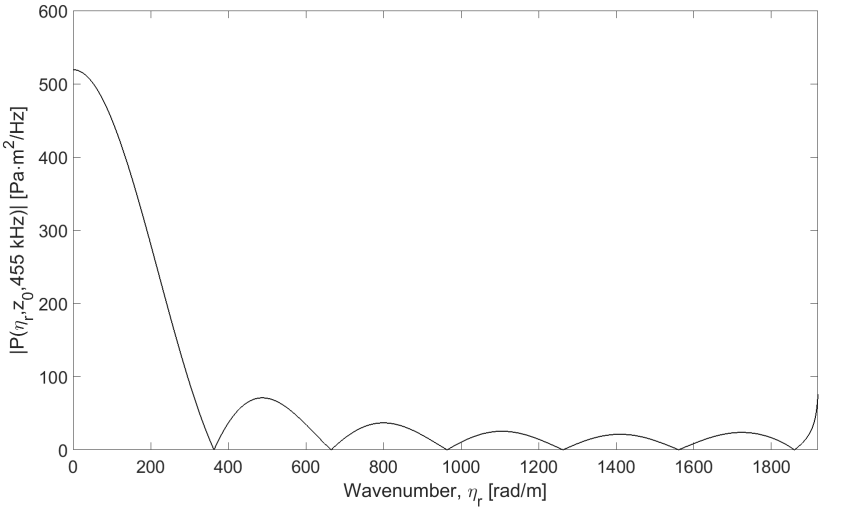

FIGURE 5.3: Zoomed in $|P_D(\eta_r, z_0, 455\,kHz)|$ from Fig. 5.2

Excluding the peak at $h_x = 1925.2\,rad/m$ from Fig. 5.2 shows a more detailed view of the directly calculated spectrum, shown in Fig. 5.3. The maximum is observed at

$\eta_r = 0$ with diminishing side lobes as η_r increases until the exponential increase at $\eta_r = h_f$.

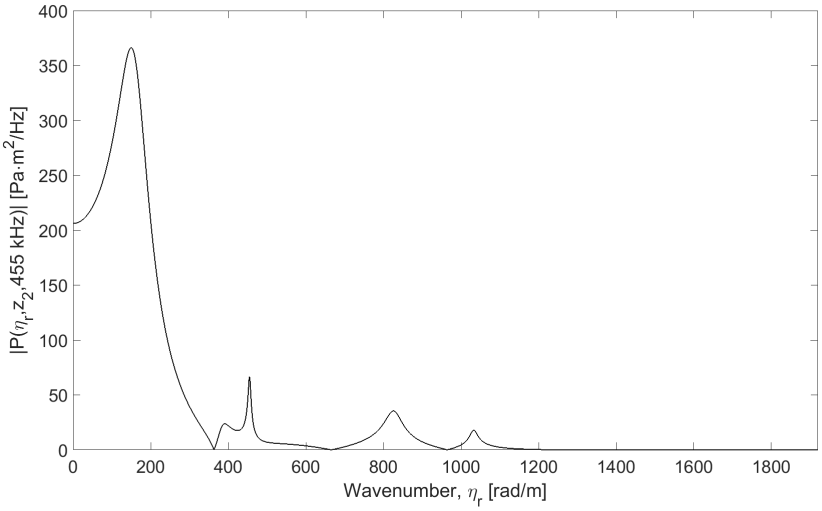

FIGURE 5.4: Directly calculated magnitude of the pressure wavenumber spectrum $P_D(\eta_r, z_2, 455kHz)$

In Fig 5.4 the magnitude of the transmitted pressure wavenumber spectrum $P_D(\eta_r, z_2, 455\,kHz)$. Here we see the influence of the plate's transmission coefficient. The peak at $\eta_r = 1925.2 rad/m$ is not present, as the magnitude approaches approaches zero along η_r after the peaks seen in Fig. 5.4.

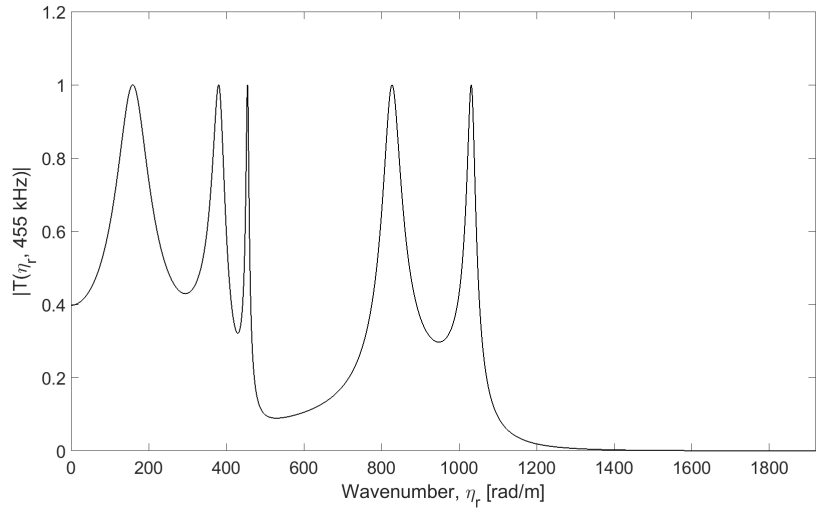

FIGURE 5.5: Directly calculated magnitude of the transmission coefficient, $T_D(\eta_r, 455kHz)$

The transmission coefficient for the frequency $455\,kHz$ is plotted in Fig. 5.5. The magnitude of the transmission coefficient has a value between 0 and 1. 0 being no transmission and 1 being unity and full transmission. Here one can see the effect the transmission coefficient has on the pressure wavenumber spectrum. The transmission coefficient $|T_D(0, 455\,kHz)| = 0.4$ shows why the transmitted $|P_D(\eta_r, z_2, 455\,kHz)|$ does not have a maximum at $\eta_r = 0$ while $|P_D(\eta_r, z_0, 455\,kHz)|$ has.

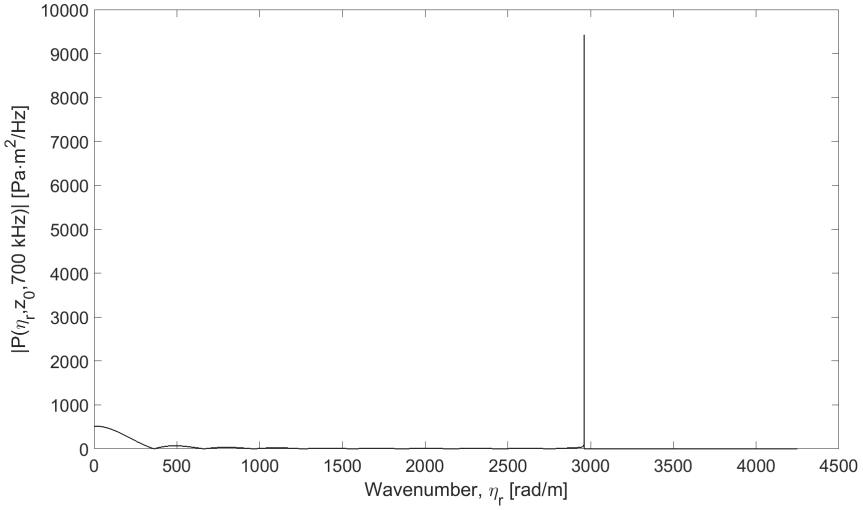

FIGURE 5.6: Directly calculated magnitude of pressure wavenumber spectrum $P_D(\eta_r, z_0, 700kHz)$

Fig. 5.6 has the magnitude of the pressure wavenumber spectrum $P_D(\eta_r, z_0, 700kHz)$ plotted. As in Fig. 5.2 we have a peak at $\eta_r = h_f$, which at $f = 700kHz$ is $h_f = 2961.8\,rad/m$.

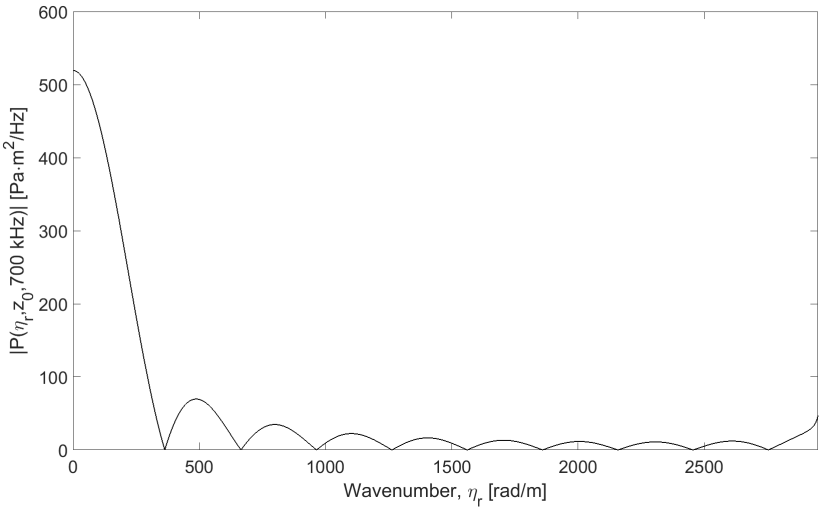

FIGURE 5.7: Zoomed in $|P_D(\eta_r, z_0, 700\,kHz)|$ from Fig. 5.6

In Fig. 5.7 as in Fig. 5.3 we see the peak at $\eta_r = 0$ and diminishing side-lobes, but here continuing further as the singularity for $f = 700\,kHz$ is higher. The pressure at $\eta_r = 0$ is the same as in Fig. 5.2, this is because the baffled piston used in this model has the same particle velocity v_0 for all frequencies.

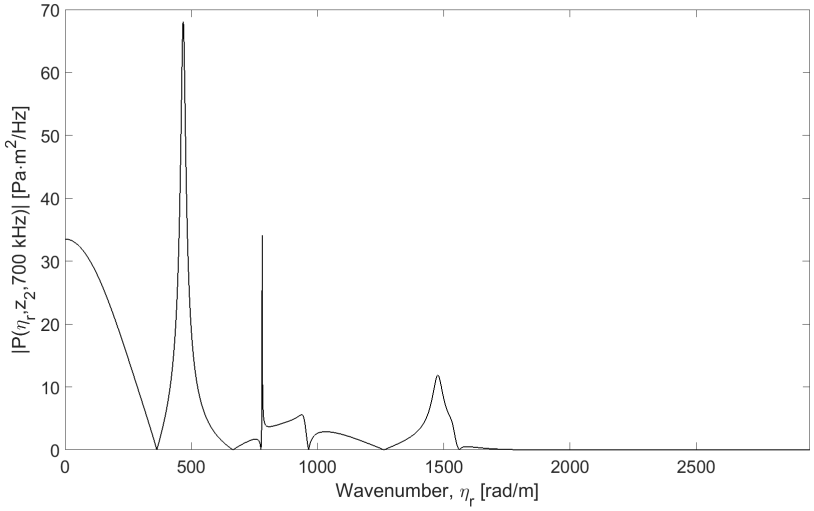

FIGURE 5.8: Directly calculated magnitude of the pressure wavenumber spectrum $P_D(\eta_r, z_2, 700kHz)$

The magnitude of the transmitted pressure wavenumber spectrum $P_D(\eta_r, z_2, 700\,kHz)$ is plotted in Fig. 5.8. Here the highest peak is not at $\eta_r = 0\,rad/m$ but rather at $\eta_r = 467.5\,rad/m$. Also worth noting is the fact that the magnitude in Fig. 5.8 is significantly lower than that of Fig. 5.4. Because $f = 700\,kHz$ is not in the vicinity a leaky Lamb mode at normal incidence.

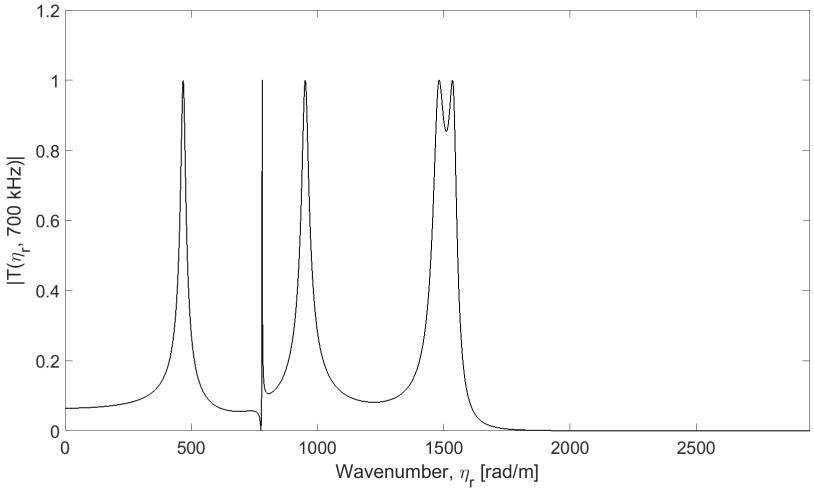

FIGURE 5.9: Directly calculated magnitude of transmission coefficient, $T_D(\eta_r, 700kHz)$

In Fig. 5.9 the magnitude of the transmission coefficient $T_D(\eta_r, 700\,kHz)$ is shown. The magnitude of the transmission coefficient at $\eta_r = 0$ is $|T_D(0, 700\,kHz)| = 0.06454$. This explains why $|P_D(0, z_2, 800\,kHz)| = 33.51\ Pa \cdot m^2/Hz$ whilst $|P_D(0, z_0, 700\,kHz)| = 519.3\ Pa \cdot m^2/Hz$. The peaks of $|T_D|$ do not overlap with peaks of $P_D(\eta_r, z_0, 955\,kHz)|$, resulting in the low transmission shown in Fig. 5.8. This is an example of how the excitation of leaky Lamb waves impact the transmitted pressure wavenumber spectrum.

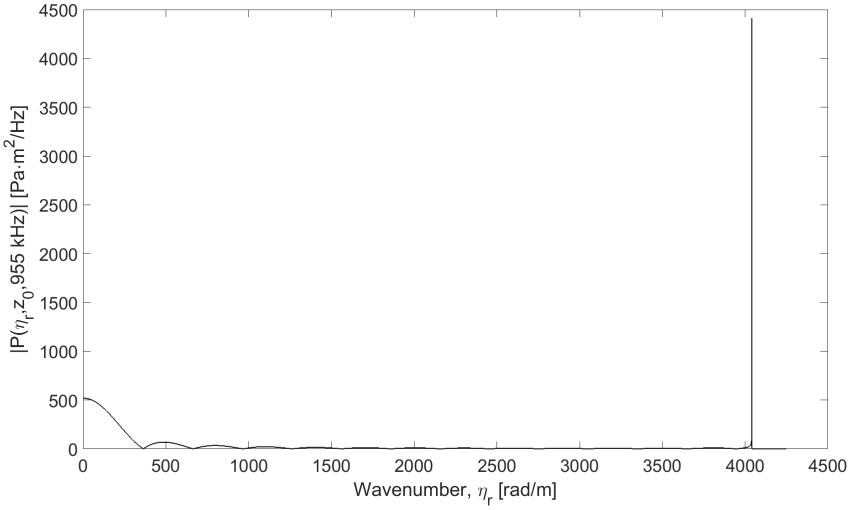

FIGURE 5.10: Directly calculated magnitude of the pressure wavenumber spectrum for $P_D(\eta_r, z_0, 955kHz)$

In Fig. 5.10 we see the magnitude of the pressure wavenumber spectrum $P_D(\eta_r, z_0, 955\,kHz)$. Here with a main at $\eta_r = 0$ with diminishing side-lobes and a peak at $\eta_r = h_f = 4040.7 rad/m$.

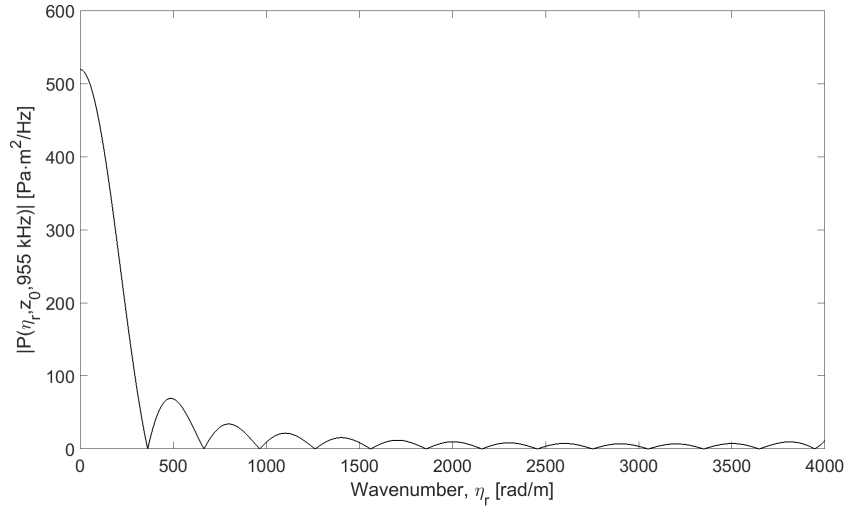

FIGURE 5.11: Zoomed in $|P_D(\eta_r, z_0, 955\,kHz)|$ from Fig. 5.10

Fig. 5.11 shows $|P_D(\eta_r, z_0, 955\,kHz)|$ from 5.10 without the peak at $\eta_r = h_f$. The magnitude at $\eta_r = 0$ is consistent with Figs. 5.3 and 5.7.

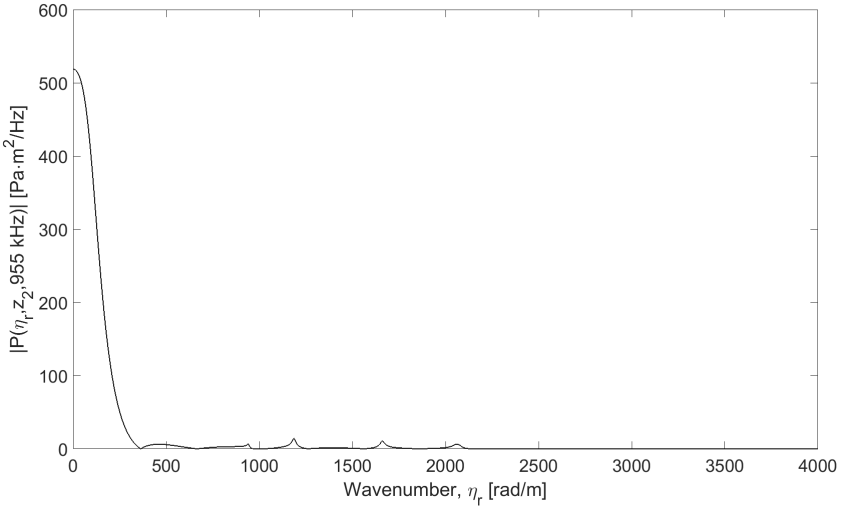

FIGURE 5.12: Directly calculated pressure wavenumber spectrum for $P_D(\eta_r, z_2, 955kHz)$

In Fig. 5.12 the magnitude of $P_D(\eta_r, z_2, 955\,kHz)$ is plotted. Here the peak from $|P_D(\eta_r, z_0, 955\,kHz)|$ is transmitted fully, with no other larger peaks along η_r.

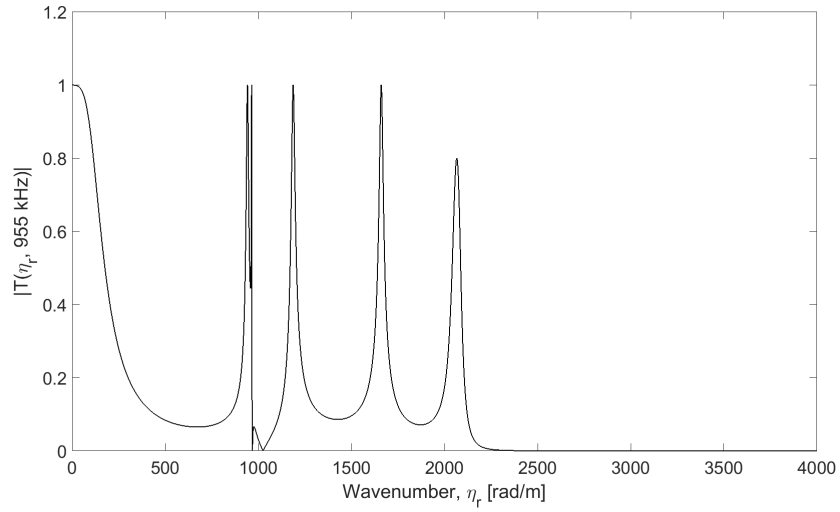

FIGURE 5.13: Directly calculated transmission coefficient, $T_D(\eta_r, 955kHz)$

Fig. 5.13 shows the transmission coefficient $|T_D(\eta_r, 955\,kHz)|$. The transmission coefficient shows why $|P_D(\eta_r, z_2, 955\,kHz)|$ has a peak at $\eta_r = 0$ as the transmission coefficient is equal to 1, meaning full transmission and the presence of a mode. The other peaks of $|T_D|$ do not overlap with any large magnitude of $|P_D(\eta_r, z_0, 955\,kHz)|$, resulting in lack of other peaks in $|P_D(\eta_r, z_2, 955\,kHz)|$.

5.1.3 Pressure Spectrum Components

In this section the simulated pressure spectrum $p_r(r, z, f)$ is presented. These are inversely Hankel transformed from the pressure wavenumber spectra of Sect. 5.1.2. They are calculated using the inverse Hankel transformation in Eqs. 2.58 and 2.59. The parameters of these transformations are given in Table. 4.1. Components of the pressure spectrum are presented in the plots. The same frequencies as in the Sect. 5.1.2 will be used.

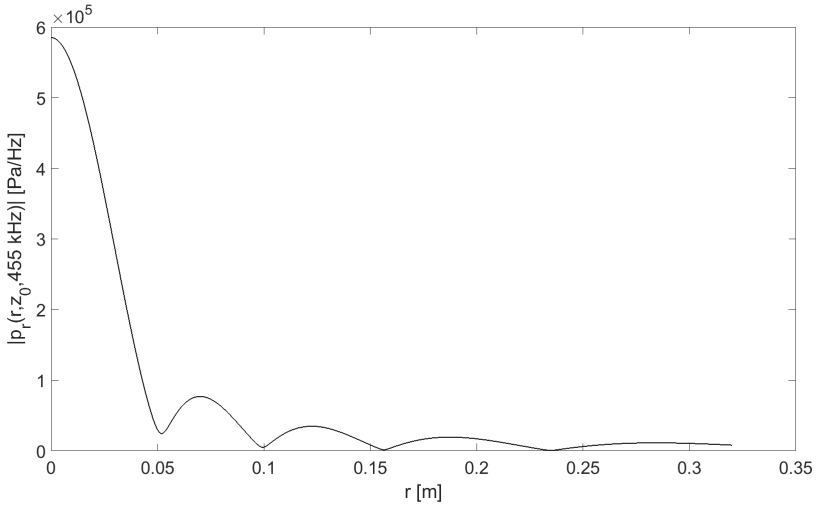

FIGURE 5.14: Calculated magnitude of the pressure spectrum component, $p_r(r, z_0, 455\,kHz)$

The simulated magnitude of pressure spectrum component $p_r(r, z_0, 455\,kHz)$ is plotted in Fig. 5.14. Along the vertical axis the magnitude $|p(r, z, f)|$ is given and the radial distance r is along the horizontal axis. We see a clear main-lobe at $r = 0\,m$ with weaker side-lobes further along. As the side-lobes diminish in magnitude, they extend along r. The simulated spectrum component stops at $r = 0.32\,m$ as this is maximum extent used in this simulation.

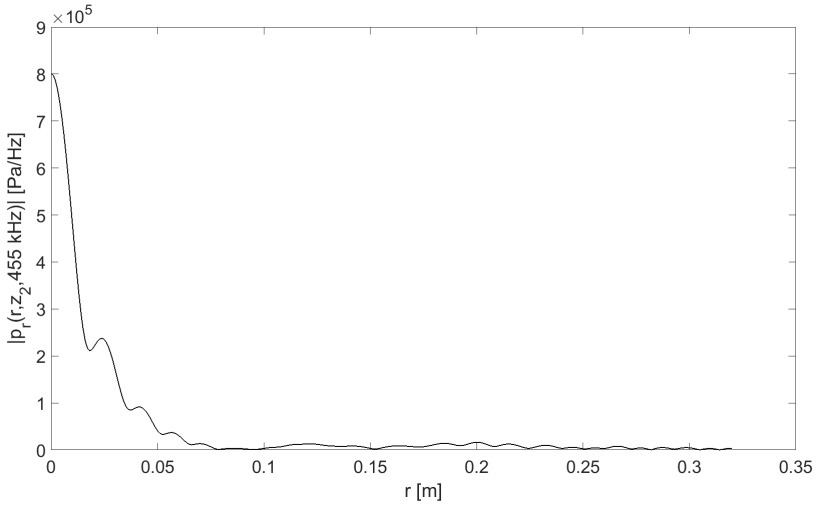

FIGURE 5.15: Calculated magnitude of the pressure spectrum component $p_r(r, z_2, 455\,kHz)$

In Fig. 5.15 the magnitude of the transmitted pressure component $p_r(r, z_2, 455\,kHz)$ is plotted. A clear main-lobe is visible at $r = 0$ with some faint side-lobes further out. Note the pressure increase of $2.7dB$ from ${}_rp(0, z_0, 455\,kHz)$ to $p_r(0, z_2, 455\,kHz)$, qualitatively consistent with [27, 11].

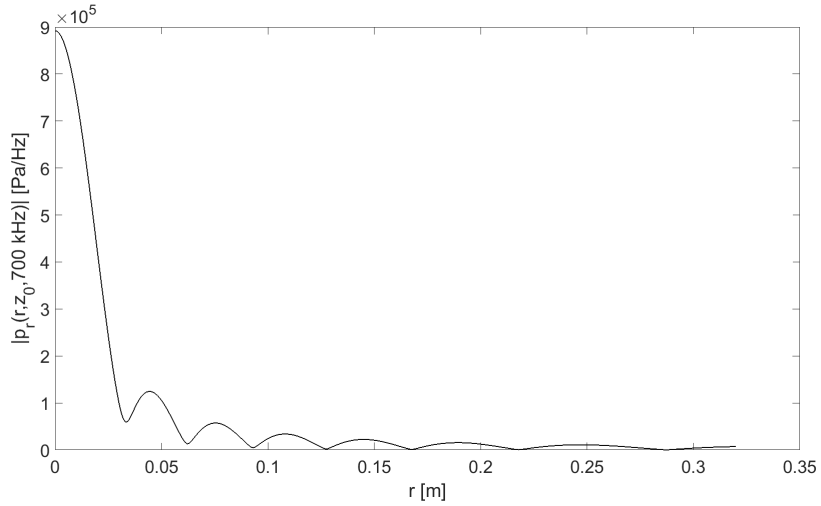

FIGURE 5.16: Calculated magnitude of the pressure spectrum component $p_r(r, z_0, 700\,kHz)$

Fig. 5.16 has the magnitude of the pressure spectrum $p(r, z_0, 700\,kHz)$ plotted. The spectrum is very similar to that of Fig. 5.14, but with a slightly narrower main lobe and more side-lobes. The pressure is also greater for $p_r(0, z_0, 700\,kHz)$ caused by the narrowing of the main-lobe.

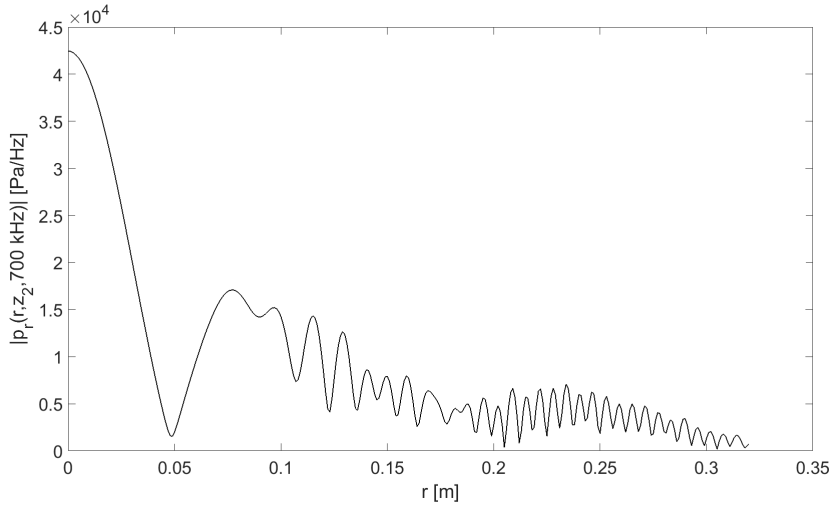

FIGURE 5.17: Calculated magnitude of the pressure spectrum component $p_r(r, z_2, 700\,kHz)$

$|p_r(r, z_2, 700\,kHz)|$ is plotted in Fig. 5.17 . Here the main lobe is significantly dampened from plate when compared to Fig. 5.16. The side lobes are not well defined and oscillate rapidly. This oscillation is accurate, as the parameters of $P_D(\eta_r, z_0 700\,kHz)$ are more than enough to give this accurate of resolution in the r-domain.

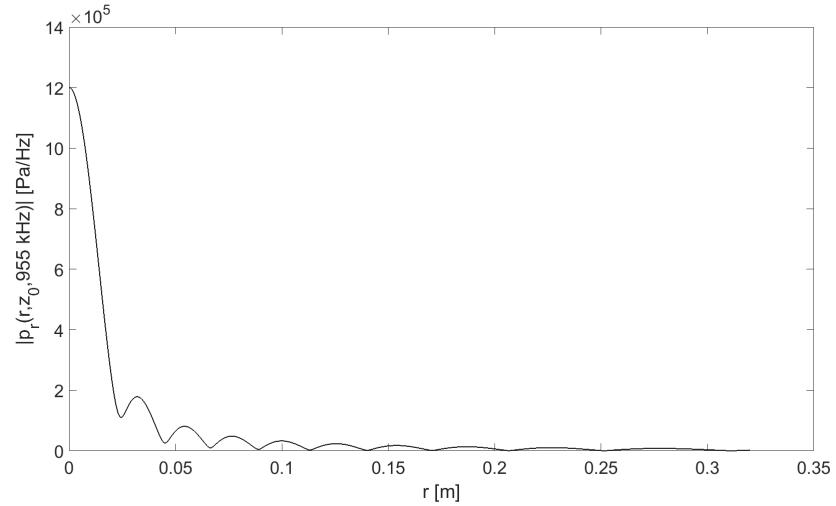

FIGURE 5.18: Calculated magnitude of the pressure spectrum component $p_r(r, z_0, 955\,kHz)$

In Fig. 5.18 the pressure spectrum component $|p_r(r, z_0, 955\,kHz)|$ is plotted. Compared to Figs. 5.14 and 5.18 the main-lobe is narrower and greater than both $p_r(0, z_0, 455\,kHz)$ and $p_r(0, z_0, 700\,kHz)$.

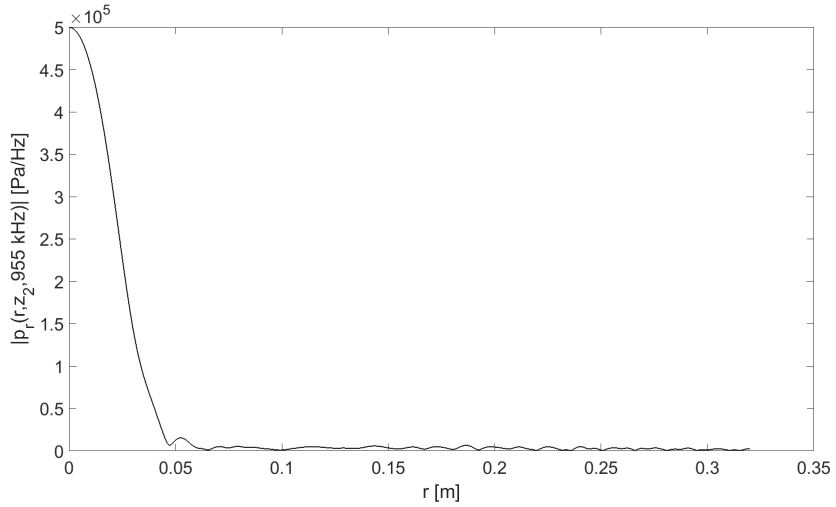

FIGURE 5.19: Calculated magnitude of the pressure spectrum component $p_r(r, z_2, 955\,kHz)$

The pressure spectrum component $|p_r(r, z_2, 955kHz)|$ is plotted in Fig. 5.19 . Here the main-lobe is very visible and is far greater than any side-lobes.

5.1.4 Post-processing Verification

In this section the simulation discussed in 4.2.5 will be presented. In this simulation the parameter $r_{max} = 63\,m$ is increased in order to increase the resolution in the wavenumber-domain to $\Delta\eta_r = 0.01\,rad/m$. The parameters and variables of this simulation are given in Tables. 4.1 and 4.3.

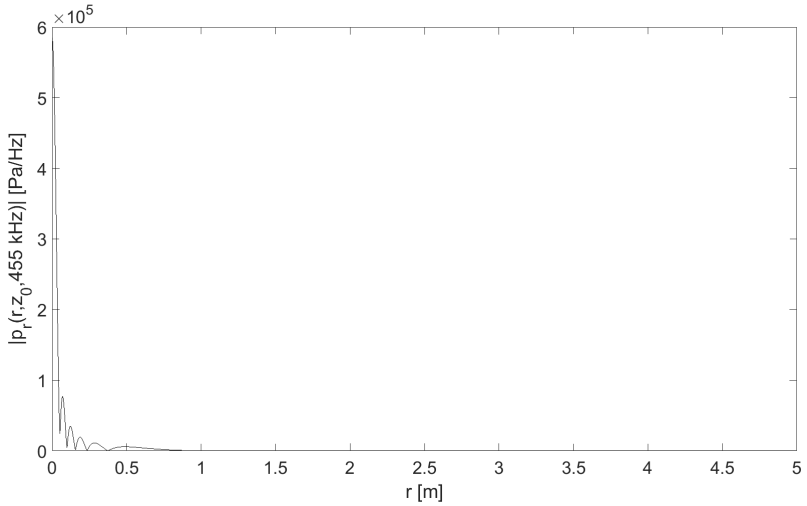

FIGURE 5.20: Calculated magnitude of the pressure spectrum $p_r(r, z_0, 455\,kHz)$

In Fig. 5.20 magnitude of the pressure spectrum component $p_r(r, z_0, 455\,kHz)$ is shown. This spectrum continues till $r = 63\,m$. With $r_{max} = 63\,m$ the pressure spectrum component is approaching zero, however there is still pressure at $r = 63\,m$. This is the result of the simulation being lossless. As the p is not zero at the end of the component, this may have effects on the Hankel transformation. This calculation is also performed for $p_r(r, z_2, 455\,kHz)$.

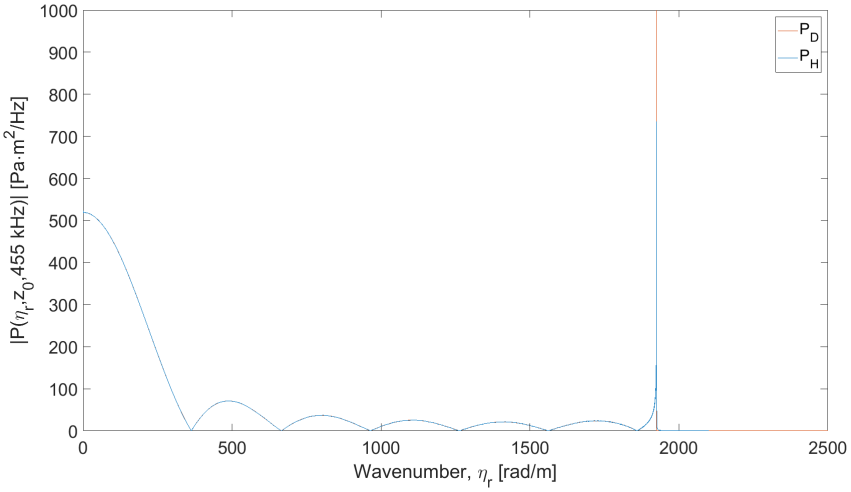

FIGURE 5.21: Magnitude comparison: $|P_H(\eta_r, z_0, 455kHz)|$ and $|P_D(\eta_r, z_0, 455kHz)|$ from Fig. 5.2

Comparing the pressure wavenumber spectrum that was Hankel transformed from the pressure spectrum in Fig. 5.20, $P_H(\eta_r, z_0, 455\,kHz)$, with the directly calculated

wavenumber spectrum from Fig. 5.14, $P_D(\eta_r, z_0, 455\,kHz)$. We see very similar curves. The most significant difference is the peak at $\eta_r = h_f$ where P_H does not reach the same value as P_D. $P_H(1925.2\,rad/m, z_0, 455\,kHz) = 740\,Pa \cdot m^2/Hz$ while $P_D(1925.2\,rad/m, z_0, 455\,kHz) \approx 24500\,Pa \cdot m^2/Hz$. This is caused by the r_{max} being insufficient for the resolution, $\Delta\eta_r$, needed to calculate these values.

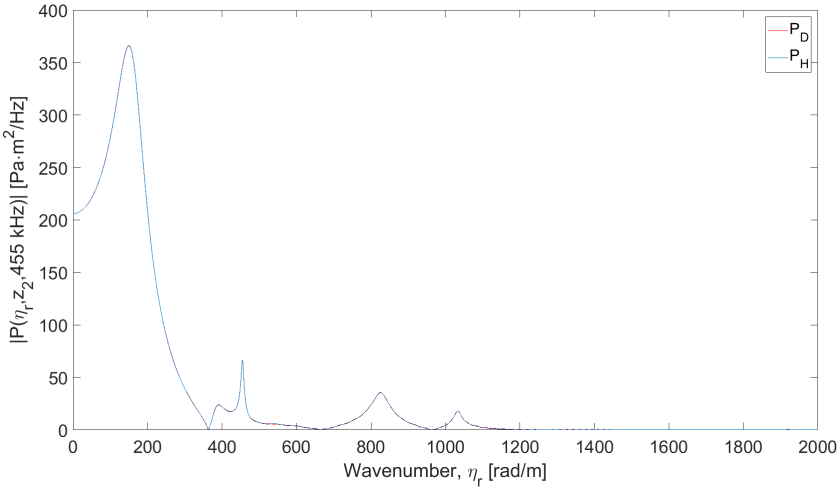

FIGURE 5.22: Magnitude comparison: $|P_H(\eta_r, z_2, 455kHz)|$ and $|P_D(\eta_r, z_2, 455kHz)|$ from Fig. 5.4

The comparison in Fig. 5.22 $P_H(\eta_r, z_2, 455\,kHz)$ and $P_D(\eta_r, z_2, 455\,kHz)$ from Fig. 5.4 we see they are almost identical as well.

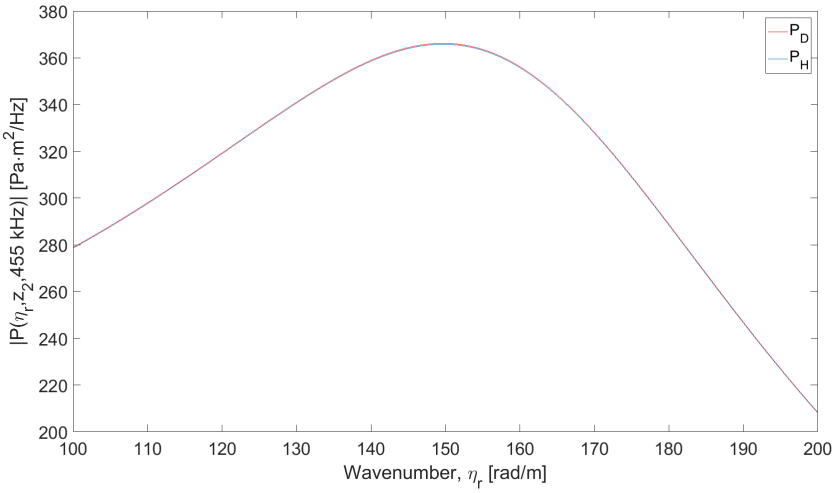

FIGURE 5.23: Zoomed in Fig. 5.22 $|P_H(\eta_r, z_2, 455kHz)|$, $|P_D(\eta_r, z_2, 455kHz)|$ from Fig. 5.3

Zooming in on a section near the peak of Fig. 5.22, Fig. 5.23 shows the interval $\eta_r = 100\,rad/m$ to $\eta_r = 200\,rad/m$. Here the variation is negligible at $\Delta P = 0.4Pa \cdot m^2/Hz$.

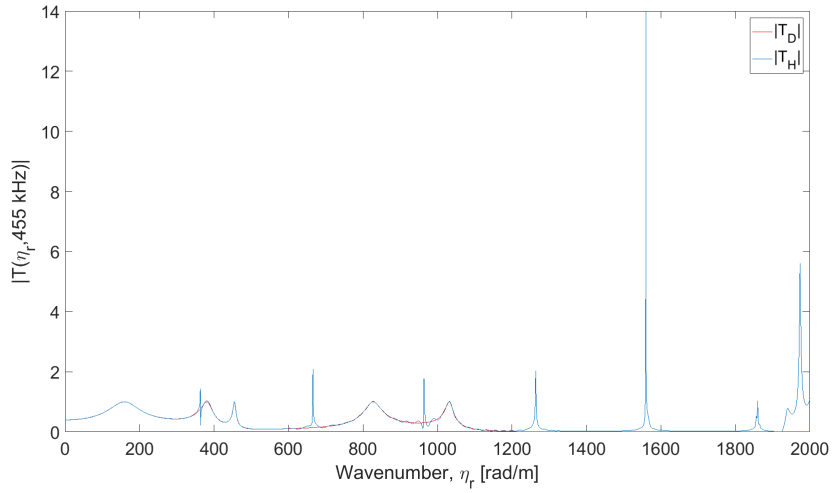

FIGURE 5.24: Comparison: $|T_H(\eta_r, 455kHz)|$, $|T_D(\eta_r, 455kHz|$ from Fig. 5.5

Using $P_H(\eta_r, z_0, 455\,kHz)$, $P_H(\eta_r, z_2, 455\,kHz)$ and Eq. 2.60 we can compare T_H with the calculated transmission coefficient, from Eq. 2.48, in Fig.5.24. Here the differences between the transformed spectra and the calculated ones becomes easier to see, as small differences between P_H and P_D can have large outcomes in the transmission coefficient.

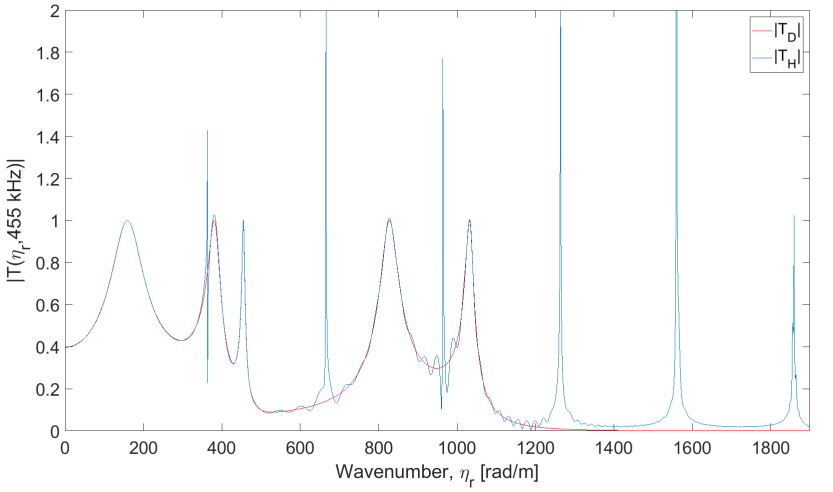

FIGURE 5.25: Zoomed in comparison from Fig. 5.24 $|T_H(\eta_r, 455kHz)|$, $|T_D(\eta_r, 455kHz)$

In Fig. 5.25 the vertical axis is scaled down and the differences from Fig. 5.24 are more evident. In general both follow transmission coefficients follow the same path, but at certain values T_H increases exponentially. This is caused by differences in $P_H(\eta_r, z_0, 455\,kHz)$ and $P_H(\eta_r, z_2, 455\,kHz)$, where $P_H(\eta_r, z_0, 455\,kHz)$ approaches zero, but $P_H(\eta_r, z_2, 455\,kHz)$ does not. The effect of the larger r_{max} is beneficial when compared to the pressure wavenumber spectrum of the next section.

The result of this simulation shows that the Hankel transformation of the pressure spectrum component in Fig. 5.20 and the z_2 equivalent does approximate $|P_D|$,

shown in Figs. 5.21 and 5.22. However as this simulation is not lossless the transformation will not be identical, because the pressure is never zero. The transmission coefficient in Fig. 5.25 showed that the transmission coefficient is not identical, but showed overall agreement in the lower wavenumbers. This would most likely improve with a larger r_{max}. The post processing method is shown to be usable.

5.1.5 Effects of Limited Spatial Resolution and Extent

In order to study the effect of the limited spatial extent and resolution of the measurements, the Hankel transformation from $p(r,z,f)$ to $P(\eta_r,z,f)$ is utilized. The pressure spectra components from Sect. 5.1.3 along with the complex phase components are Hankel transformed to the wavenumber domain. This calculation is detailed in Sect. 4.2.3. The wavenumber resolution here is $\Delta\eta_r = 20\,rad/m$. The pressure wavenumber spectra are compared to the directly calculated spectra from Sect. 4.2.1.

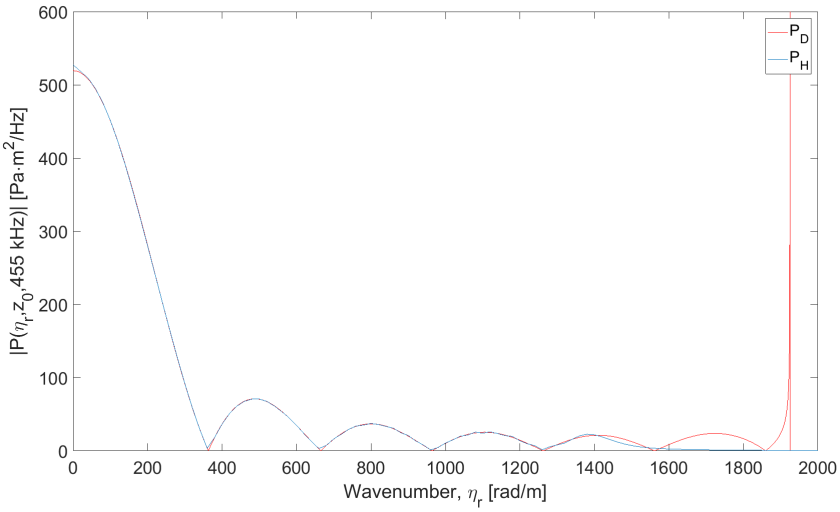

FIGURE 5.26: Magnitude comparison: $|P_H(\eta_r, z_0, 455kHz)|$ and $|P_D(\eta_r, z_0, 455kHz)|$ from Fig. 5.2

In Fig. 5.26 the magnitude of $P_H(\eta_r, z_0, 455\,kHz)$ for the Hankel transformed wavenumber spectrum $|P_H|$ and the directly calculated wavenumber spectrum $|P_D|$ from Fig 5.2 are compared. $|P_H|$ is transformed from the pressure spectrum component in Fig 5.14. Here there are several significant difference between the spectra. Firstly the magnitudes at $\eta_r = 0$ are not the same. $|P_H|$ starts at the value $|P_H| = 527.4Pa \cdot m^2/Hz$ while $|P_D| = 519.3\,Pa \cdot m^2/Hz$. following this $|P_H|$ does not reach the minimum of $|P_D|$. While $|P_D|$ reaches a first minimum of $0.00014\,Pa \cdot m^2/Hz$, $|P_H|$ reaches a minimum of $3.558\,Pa \cdot m^2/Hz$. This continues for the next three minimums. After the minimum near $\eta_r = 1260\,rad/m$ $|P_H|$ diverges from the path of $|P_D|$ and does not include the peak at $\eta_r = h_f$. Following the peak at $\eta_r = h_f$ $|P_D|$ is zero, however $|P_H|$ does not reach zero. When compared to Fig. 5.21 where $|P_H|$ follows the path of P_D it is evident that the lack of extent in the spatial domain impacts the pressure wavenumber spectrum.

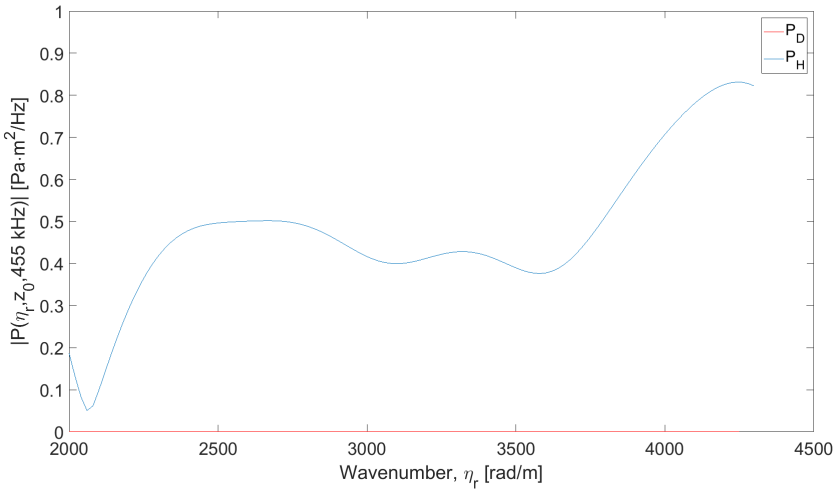

FIGURE 5.27: Zoomed in view from Fig 5.26, $|P_H(\eta_r, z_0, 455kHz)|$ after $\eta_r = h_f$

Zooming in on the area after the peak at $\eta_r = h_f$ we see in Fig. 5.27 that P_H does in fact not decrease, but rises, while $|P_D|$ approaches zero. The calculation of $|P_H|$ ends at $4300\,rad/m$, but it seems as the magnitude would rise further if a larger $\eta_{r,max}$ was used. The magnitude is minimal when compared to the value at $\eta_r = 0$ from Fig. 5.26, but shows that there are issues with the implementation Hankel transformation. Specifically the pressure spectrum components being nonzero at the r-limit.

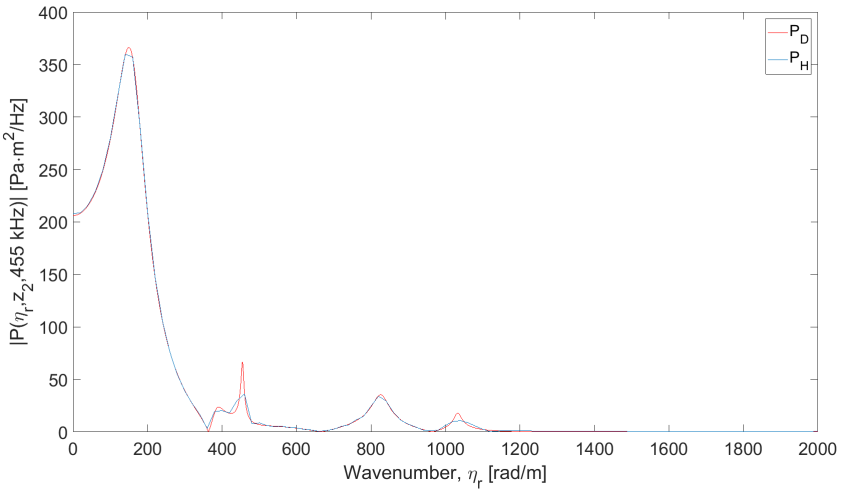

FIGURE 5.28: Magnitude comparison: $|P_H(\eta_r, z_2, 455kHz)|$ and $|P_D(\eta_r, z_2, 455kHz)|$ from Fig. 5.4

In Fig. 5.28 the magnitude of the transmitted wavenumber pressure spectra $P(\eta_r, z_2, 455\,kHz)$ are plotted. $|P_D|$ is from Fig. 5.4 and $|P_H|$ is Hankel transformed from the pressure spectrum component in Fig. 5.15 along with the complex phase component. In this figure the resolution of $|P_H|$ is more evident. This can be seen at the peaks of $|P_D|$ and $|P_H|$. The large $\Delta\eta_r$ means that the peaks of $|P_D|$ are not replicated by $|P_H|$.

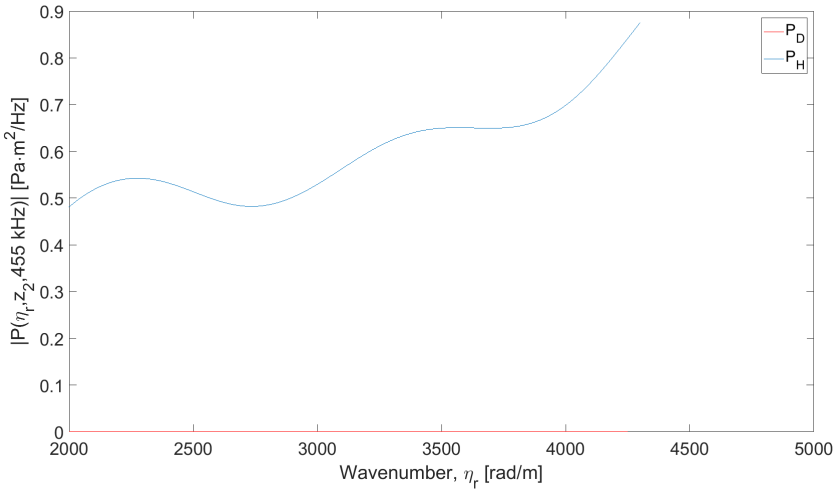

FIGURE 5.29: Zoomed in view from Fig 5.28, $|P_H(\eta_r, z_2, 455kHz)|$ after $\eta_r = h_f$

Showing the interval after $\eta_r = h_f$ for $|P_H(\eta_r, z_2, 455\,kHz)|$ in Fig. 5.29 we see the same effect as in Fig. 5.27. The magnitude of P_H rises while P_D approaches zero.

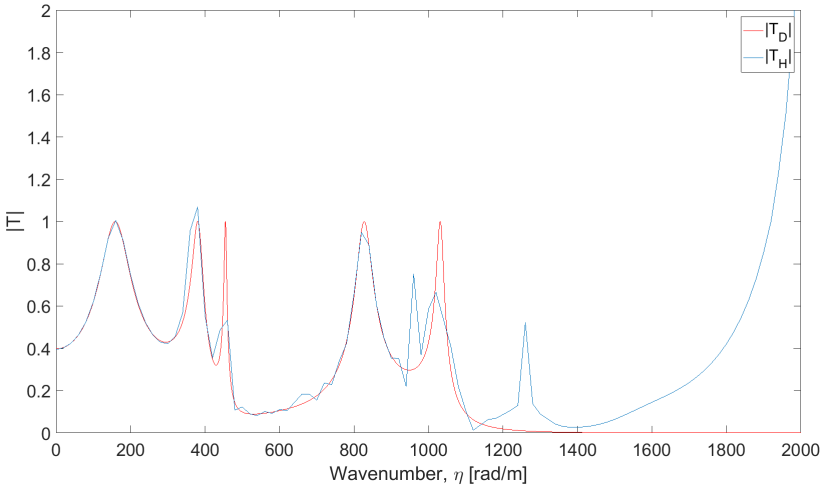

FIGURE 5.30: Magnitude comparison: $|T_H(\eta_r, 455kHz)|$ and $|T_D(\eta_r, 455kHz)|$ from Fig. 5.5

The difference between the directly calculated results and the Hankel transformed results are very evident in the magnitude of the transmission coefficient. In Fig. 5.30 the directly calculated transmission coefficient $|T_D|$, from Fig 5.5, and the transmission coefficient, $|T_H|$, calculated from $P_H(\eta_r, z_0, 455\,kHz)$ and $P_H(\eta_r, z_2, 455\,kHz)$ are plotted. The calculation of T_H is detailed in Sect 4.2.4. The first peak of the transmission coefficient is replicated by $|T_H|$. However $|T_H|$ does in fact exceed unity with a value of $|T_H(160\,rad/m, 455\,kHz)| = 1.005$. This is easily visible at the second peak. The third peak is not replicated by $|T_H|$ because the width of the peak is smaller than the resolution of $|T_H|$. Following this $|T_D|$ is somewhat replicated. After the minimum of $|T_H|$ at $\eta_r = 1120 rad/m$ $|T_H|$ diverges from $|T_D|$ and becomes exponential.

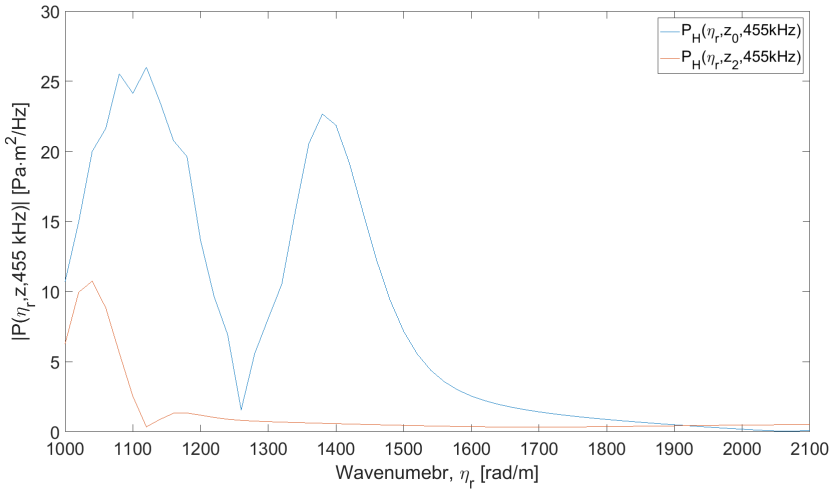

FIGURE 5.31: Magnitude comparison: $|P_H(\eta_r, z_0, 455kHz)|$ from Fig. 5.26 and $|P_H(\eta_r, z_2, 455kHz)|$ from Fig. 5.28

In Fig. 5.31 the magnitude of the two pressure wavenumber spectra $P_H(\eta_r, z_0, 455\,kHz)$ and $P_H(\eta_r, z_2, 455\,kHz)$ from Fig. 5.26 and 5.28 respectively. Here we see what causes the exponential growth of $|T_H|$. The peak at $\eta_r = 1380\,rad/m$ signifies the minimum of $|T_H|$. Following this the decrease of $|P_H(\eta_r, z_0, 455\,kHz)|$ causes the exponential growth. This does not happen for $|T_D|$.

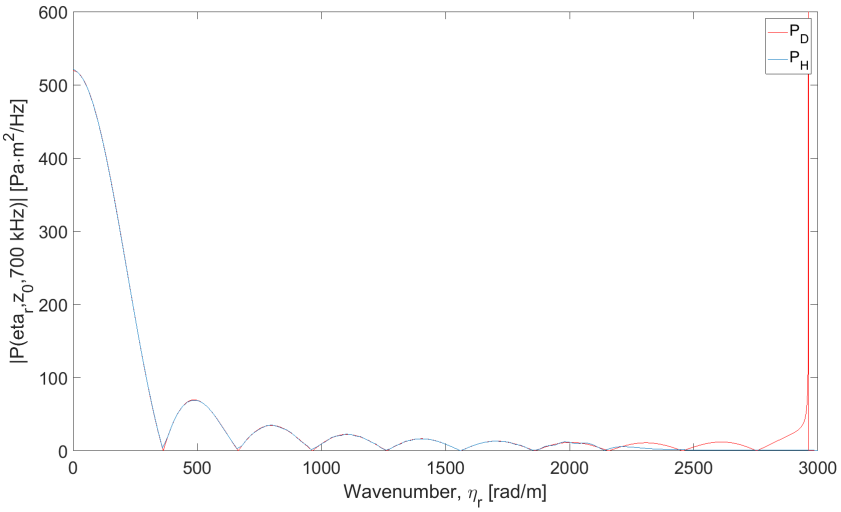

FIGURE 5.32: Magnitude comparison: $|P_H(\eta_r, z_0, 700kHz)|$ and $|P_D(\eta_r, z_0, 700kHz)|$ from Fig. 5.6

The magnitude of $P_H(\eta_r, z_0, 700\,kHz)$ and $P_D(\eta_r, z_0, 700\,kHz)$, from Fig. 5.6, are plotted in Fig. 5.32. $|P_H|$ is Hankel transformed from the pressure spectrum component in Fig. 5.16 with the complex component of the phase. Here the same effects as in Fig. 5.26 are observed. Although the disparity between the two at $\eta_r = 0$ is smaller than in Fig. 5.26, with $|P_H| = 521.6\,Pa \cdot m^2/Hz$. Following this the same effects as discussed for Fig. 5.26 are observed here. $|P_H|$ not reaching the minimum of $|P_D|$ and diverging from $|P_D|$. Although $|P_H|$ diverges from $|P_D|$ further along η_r when compared to Fig. 5.26. The effect of rise in magnitude after $\eta_r = h_f$ is observed for $|P_H(\eta_r, z_0, 700\,KHz)|$ as in Fig. 5.27.

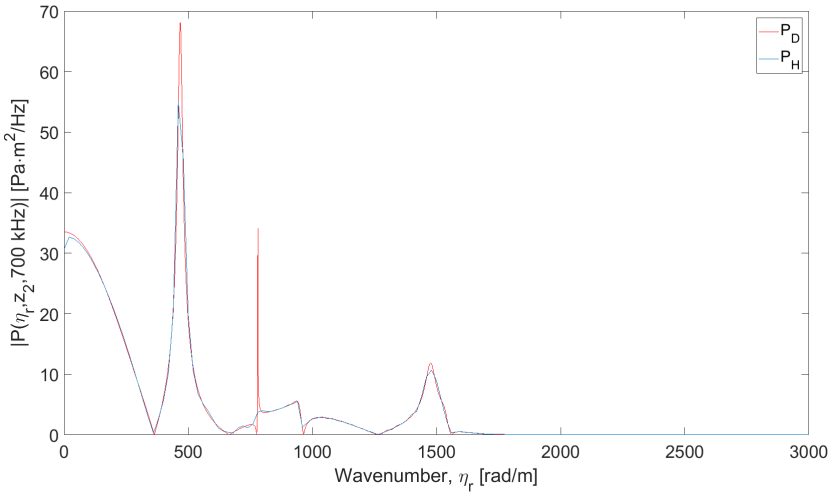

FIGURE 5.33: Magnitude comparison: $|P_H(\eta_r, z_2, 700kHz)|$ and $|P_D(\eta_r, z_2, 700kHz)|$ from Fig. 5.8

In Fig. 5.33 the Hankel transformed pressure wavenumber spectrum $|P_H(\eta_r, z_2, 700\,kHz)|$ is compared to the directly calculated wavenumber spectrum from Fig. 5.8. $|P_H|$ is Hankel transformed from the pressure spectrum component in Fig. 5.17 along with the complex phase component. In the plot some significant differences are observed. At $\eta_r = 0$ there is a relatively large difference in magnitude. The opposite effect of what is observed in Fig. 5.32 and the other Hankel transformed z_0-spectra. Here $|P_H|$ has a magnitude of $30.62Pa \cdot m^2/Hz$ compared to $|P_D|$ which has a magnitude of $33.51Pa \cdot m^2/Hz$. The largest peak of $|P_D|$ is not fully replicated by $|P_H|$ either. This is caused by the peak being narrower than $20\,rad/m$. The minimum and peak around $780\,rad/m$ is not shown by $|P_H|$ in any form, again caused by the lack of resolution. The effect of increase in magnitude after $\eta_r = h_f$ is observed for $|P_H(\eta_r, 700\,kHz)|$ as in Fig. 5.29.

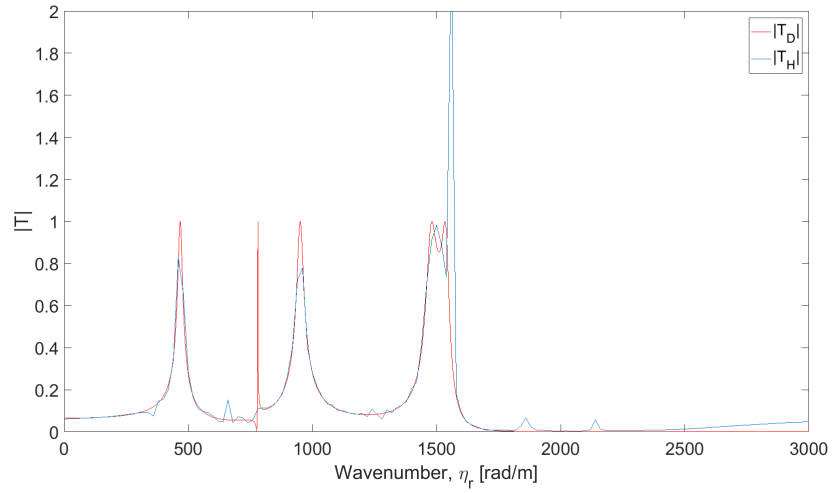

FIGURE 5.34: Magnitude comparison: $|T_H(\eta_r, 700kHz)|$ and $|T_D(\eta_r, 700kHz)|$ from Fig. 5.9

In Fig. 5.34 the plots of $T_D(\eta_r, 700\,kHz)$ from Fig. 5.9 and the transmission coefficient T_H. T_H is calculated from the spectra $P_H(\eta_r, z_0, 700\,kHz)$ and $P_H(\eta_r, z_2, 700\,kHz)$ from Figs. 5.32 and 5.33. Fig. 5.34 is similar to Fig. 5.33 in that many of the peaks become

too narrow for T_H to replicate. $|T_H|$ replicates $|T_D|$ to the level of detail possible with these parameters for the first and third peak. The second peak and the minimum are not visible in $|T_H|$ other than a small increase. The third peak of $|T_D|$ is replicated at first, but $|T_H|$ deviates and becomes exponential. This is caused by the discrepancies in the Hankel transformed pressure wavenumber spectra.

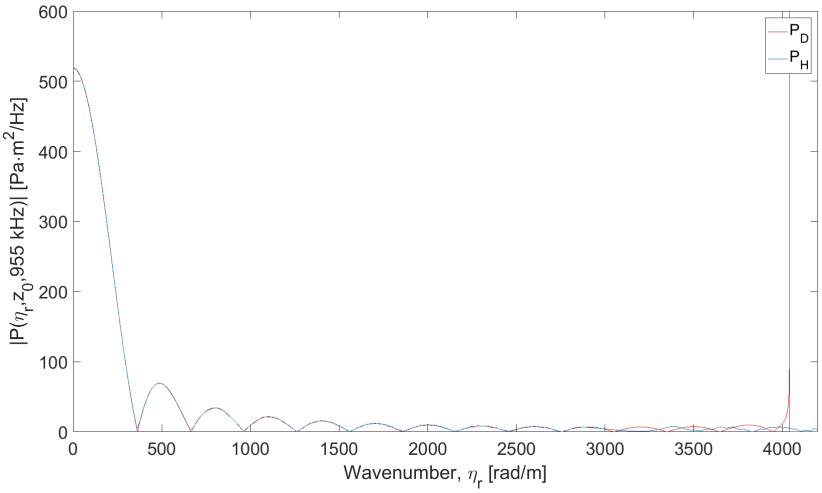

FIGURE 5.35: Magnitude comparison: $|P_H(\eta_r, z_0, 955kHz)|$ and $|P_D(\eta_r, z_0, 955kHz)|$ from Fig. 5.10

$|P_D(\eta_r, z_0, 955\,kHz)|$, from fig 5.10, and $|P_H(\eta_r, z_0, 955\,kHz)|$ are plotted in Fig. 5.35 . $|P_H|$ is Hankel transformed from the pressure spectrum component of Fig. 5.18 with the complex phase component. The same effects of Fig. 5.26 and 5.32 can be seen for $|P_H|$. Effects such as the slight different value at $0\,rad/m$, the higher minimum when compared to $|P_D|$ and the deviation from $|P_D|$. The effect of increase in magnitude after $\eta_r = h_f$ shown in Fig. 5.27 is not as evident in $|P_H(\eta_r, z_0, 955\,kHz)|$ as the peak at $\eta_r = h_f$ is at $4040.7 rad/m$ and the calculation continues to $\eta_{r,max} = 4300\,rad/m$. However $|P_H|$ does not seem to approach zero.

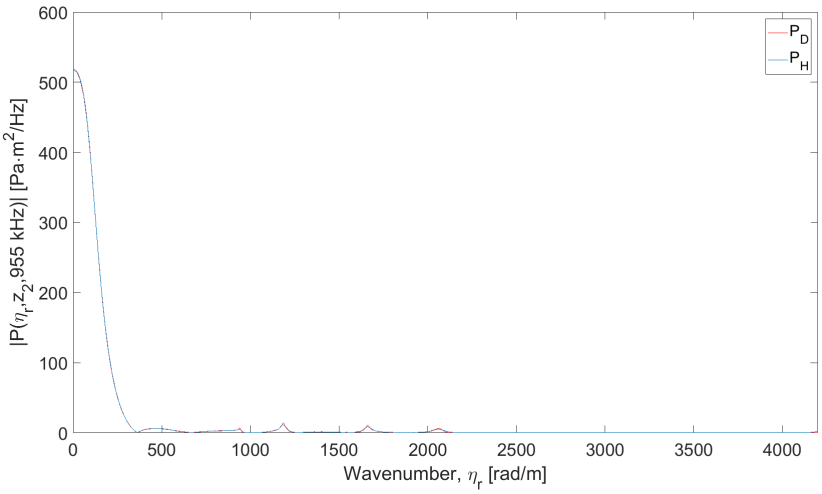

FIGURE 5.36: Magnitude comparison: $|P_H(\eta_r, z_2, 955kHz)|$ and $|P_D(\eta_r, z_2, 955kHz)|$ from Fig. 5.12

In Fig 5.36 the pressure wavenumber spectra $|P_D(\eta_r, z_2, 955\,kHz)|$, from Fig. 5.12, and $|P_H(eta_r, z_2, 955\,kHz)|$. $|P_H|$ is Hankel transformed from the pressure spectrum component of Fig. 5.19 with the complex phase component. The effect after $\eta_r = h_f$ is not as visible as in Fig. 5.29 because the calculation ends at $\eta_r = 4300\,rad/m$, but $|P_H(\eta_r, z_2, 955\,kHz)|$ does not seem to be approaching zero as $|P_D|$.

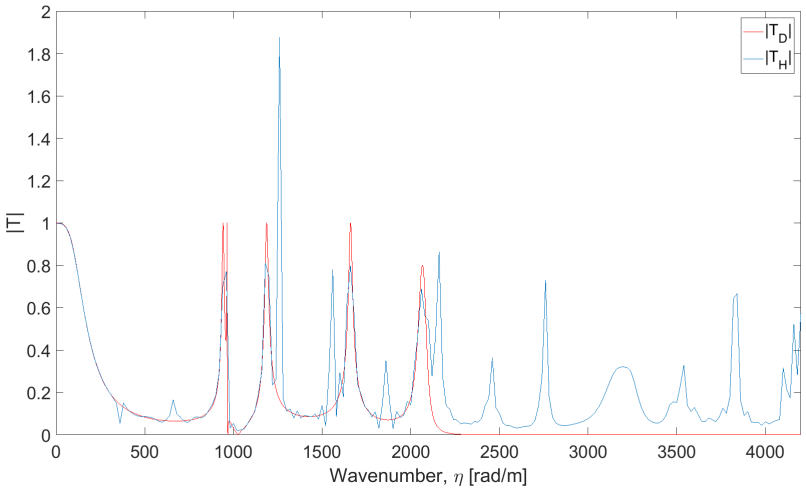

FIGURE 5.37: Magnitude comparison: $|T_H(\eta_r, 955kHz)|$ and $|T_D(\eta_r, 955kHz)|$ from Fig. 5.13

In Fig. 5.37 $|T_D(\eta_r, z_0, 955\,kHz)|$, from fig 5.13, and $|T_H(\eta_r, z_0, 955\,kHz)|$. T_H is calculated from the pressure wavenumber spectra $P_H(\eta_r, z_0, 955\,kHz)$ and $P_H(\eta_r, z_2, 955\,kHz)$ from Fig. 5.35 and 5.36. $|T_D|$ and $|T_H|$ have approximately the same magnitude at $0\,rad/m$, with T_H slightly lower. The transmission coefficient, $|T_D|$ has several narrow peaks following the first peak. These are too narrow to be replicated by $|T_H|$.

Through the inspection of the Hankel transformed wavenumber spectra and the corresponding transmission coefficients, it has been observed that P_H is a reasonable approximation of $|P_D|$ at lower wavenumbers. The approximation's similarities seem to end when $|P_H|$ approaches the singularity of $\eta_r = h_f$, seen in Fig. 5.26. The point at which $|P_H|$ deviates from $|P_D|$ is frequency dependant and increases with f. In conclusion the effect of the lack of extent and resolution coupled with the implementation of the Hankel transformation means a full approximation of $|P_D|$ is not possible with the current post-processing method. However a reasonable approximation of the pressure wavenumber spectrum and transmission coefficient is possible for lower wavenumber values below $\eta_r = h_f$, with this method and parameters.

5.2 On-axis Measurement Results

In this section the results from the conducted on-axis measurements will be presented. Examples of the sampled waveforms are presented. Following this the post-processing results from the on-axis measurements are shown with comparison to previous work.

5.2.1 On-axis Measurement Waveforms

The following waveforms will be a representation of the measurements. The same carrier frequencies, f_c will be used as the frequencies used in Sect. 5.1 $f = 455, 700, 955\,kHz$, at positions z_0 and z_2.

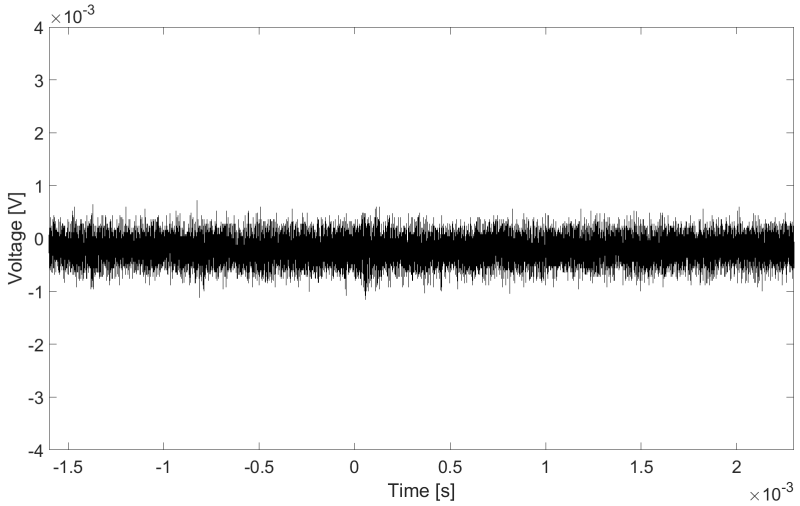

FIGURE 5.38: Sampled voltage, $V(x_0, z_0, t)$ without transmitted signal

Fig. 5.38 shows the sampled interval from when the hydrophone was placed in the tank and sampled the noise, without the transducer. Along the vertical axis the magnitude of the measured voltage is shown. Along the horizontal axis the time from when the oscilloscope is triggered is shown. As mentioned in Sect. 3.3.3 the oscilloscope is triggered 1600 μs before the transducer radiates the signal. The noise level is relatively low, with no distinguishing features, meaning no periodic signal will be received other than that of the transducer. This gives a baseline of the noise present in the tank and will be referred to later on.

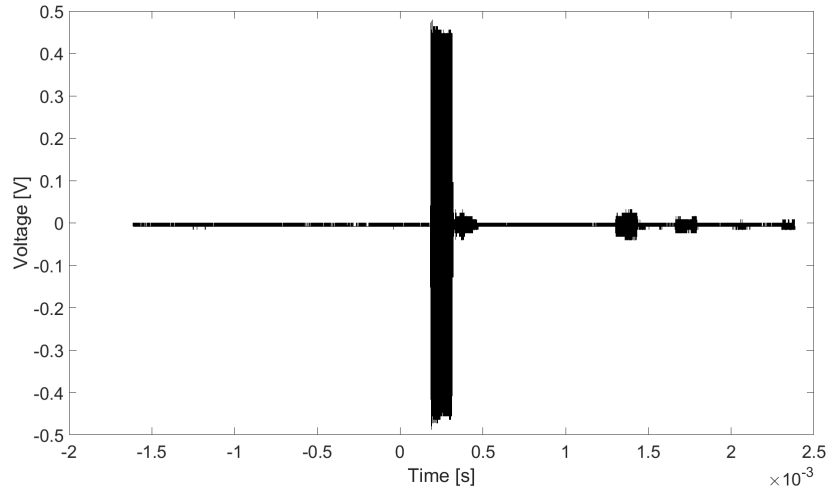

FIGURE 5.39: Sampled voltage, $V(x_0, z_0, t)$ with carrier frequency $f = 455\,kHz$

In Fig. 5.39 the sampled time interval of $4000\,\mu s$ for the measurement of the carrier frequency $f_c = 455\,kHz$. The signal is very visible with a time of arrival (TOA) of $t = 0.0001825\,s$. This is consistent with a calculated TOA of approximately $t \approx 0.000182\,s$. This is calculated using the direct path and velocity $c_f = 1485$. Along the sampled time interval other signals are also visible. The first of which is right behind the direct signal. This is attributed to reflections off the side wall as the TOA coincides with this distance traveled. The next two signals have TOA's equal to $t = 0.00130\,s$ and $t = 0.00166s$. These amount to such long paths of travel that it is difficult to deduce what they are reflected off of and the path taken.

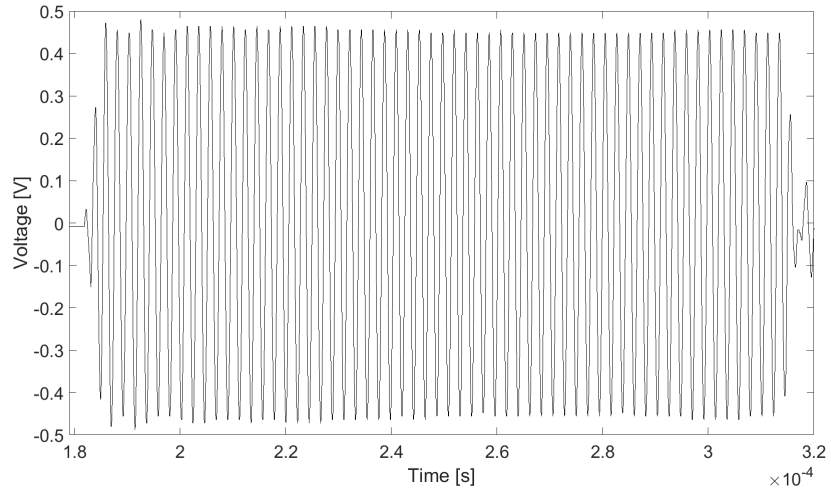

FIGURE 5.40: Zoomed in 5.55, $V(x_0, z_0, t)$. With carrier frequency $455\,kHz$

In Fig. 5.40 the section of the sampled interval from Fig. 5.39 containing the direct signal is shown. The signal has a length of approximately $132\,\mu s$. The start and end of the signal are well defined and the signal strength is very stable throughout.

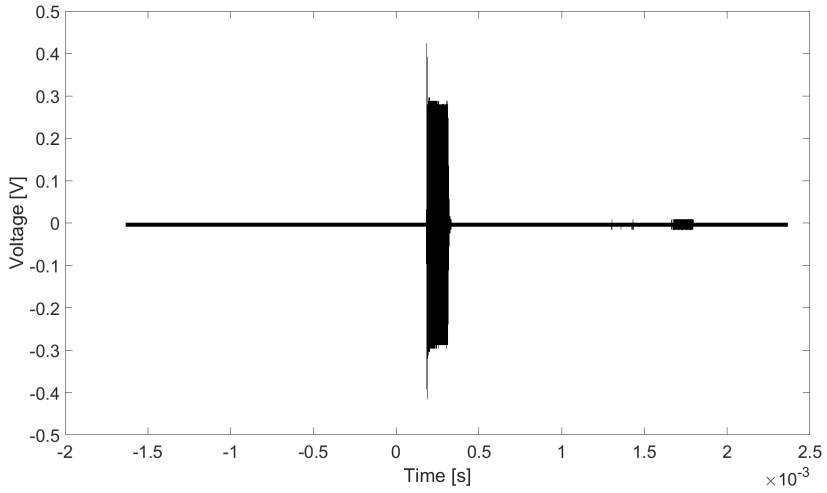

FIGURE 5.41: Sampled voltage, $V(x_0, z_0, t)$. With carrier frequency $700\,kHz$

The sampled time interval for carrier frequency $f_c = 700\,kHz$ at position z_0 is plotted in Fig. 5.41. The first noticeable difference from Fig. 5.39 is the decrease in voltage, this is due to the transducer being most effective around $575\,kHz$ [11]. The two distinct trailing signals have equivalent TOAs of that in Fig. 5.39.

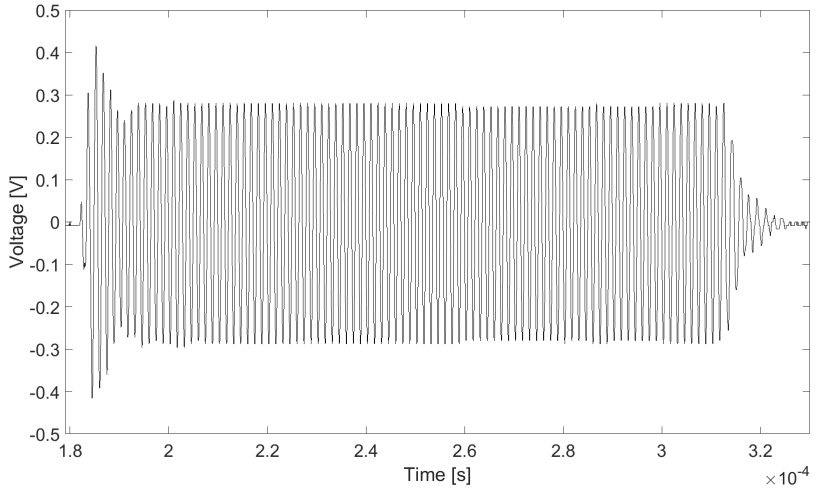

FIGURE 5.42: Zoomed in Fig. 5.41, $V(x_0, z_0, t)$. With carrier frequency $700\,kHz$

The time interval containing the signal from Fig. 5.41 is shown in Fig. 5.42. The TOA is approximately $t \approx 0.000182\,s$ and lasts approximately $140\,\mu s$. This increase in signal length is caused by the trail seen towards the end of the signal. This trail is attributed to the same reflection as seen right behind the signal in Fig. 5.39. Compared to Fig. 5.40 we see a sharp increase of the voltage before stabilizing. This is caused by the transient region before the transducer stabilizing. Overall the signal is stable throughout.

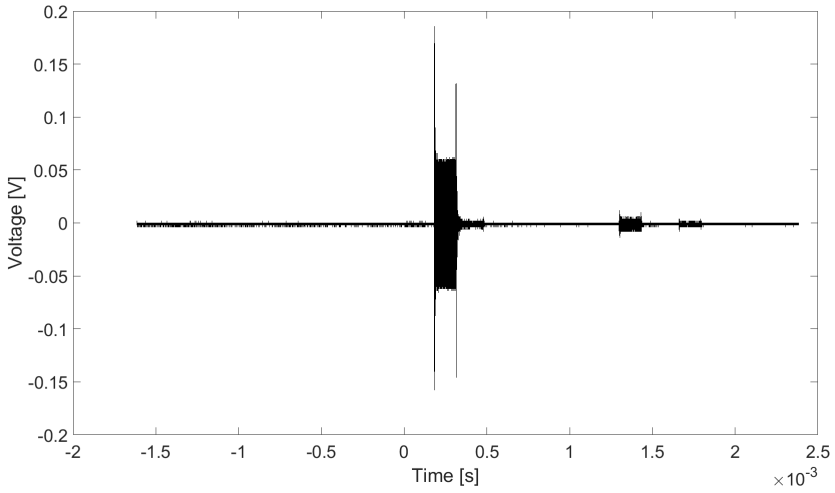

FIGURE 5.43: Sampled voltage, $V(x_0, z_0, t)$. With carrier frequency $955\,kHz$

$V(x_0, z_0, t)$, the sampled time interval with carrier frequency $955\,kHz$ is plotted in Fig. 5.43. Again a significant drop in voltage can be seen when compared to both Figs. 5.39 and 5.41. With two spikes at the start and end of the direct signal caused by the transient region before and after the steady state region. The trail right after the signal is clearly visible here and is attributed to reflections off the side wall. The two distinct signal following the direct signal have equivalent TOAs of that in Figs. 5.39 and 5.41.

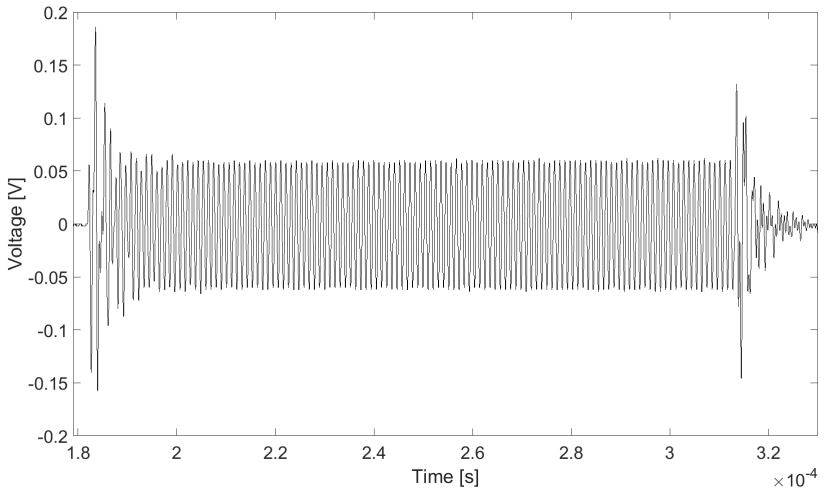

FIGURE 5.44: Zoomed in Fig. 5.43, $V(x_0, z_0, t)$. With carrier frequency $955\,kHz$

In Fig. 5.44 the interval containing the direct signal from 5.43 is shown. The direct signal has a approximate time of arrival $t \approx 0.000182\,s$ and lasting approximately $130\,\mu s$. Here the two spikes at the start and end are visible. The signal is stable throughout the steady state.

Next the sampled waveforms for the received transmitted signal are shown, at position z_2.

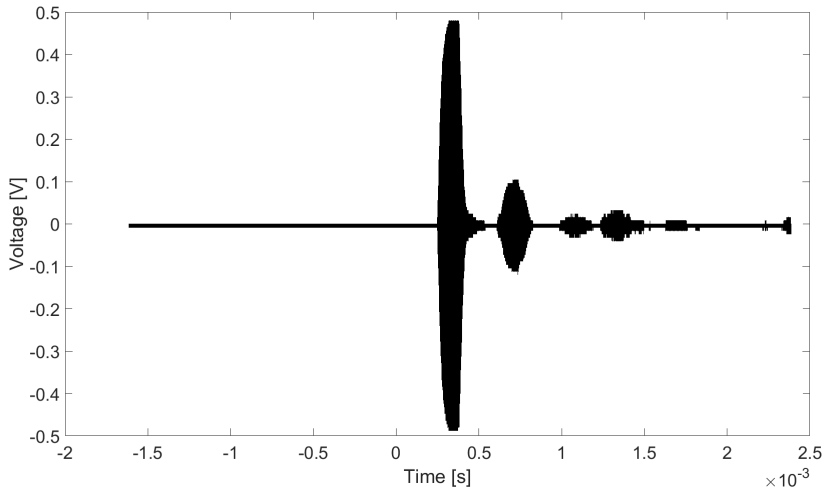

FIGURE 5.45: Sampled voltage, $V(x_0, z_2, t)$ with carrier frequency $455\,kHz$

In Fig. 5.45 sampled interval at position z_2 for carrier frequency $455\,kHz$ is shown. This signal has been transmitted through the steel plate and has been subject to the effects of this, such as dispersion, diffraction and reflection. Here we also see reflected signals trailing the transmitted signal. In addition to reflected signals off walls, reflected signals within the plate can also contribute to this. The longer trail of the signal is most likely caused by these reflections within the plate. The larger signal seen with a TOA $t = 0.00061\,s$ is not seen in any of the z_0 measurements. This means the presence of the plate is causing this signal. However accounting for the time of flight through the fluid, using the distance $z_2 - d$, $0.37m/1485m/s = 0.00025s$. This remaining time results in a distance travelled within the plate amounting to $1.44m$ if using c_l which seems unlikely as the plate is $500\,mm$ wide and would result in multiple reflections within the plate before transmission. What this signal is reflected from is therefore uncertain. There are also three other distinct signals visible after this larger one. These signals have such high TOA's a path is difficult to assign.

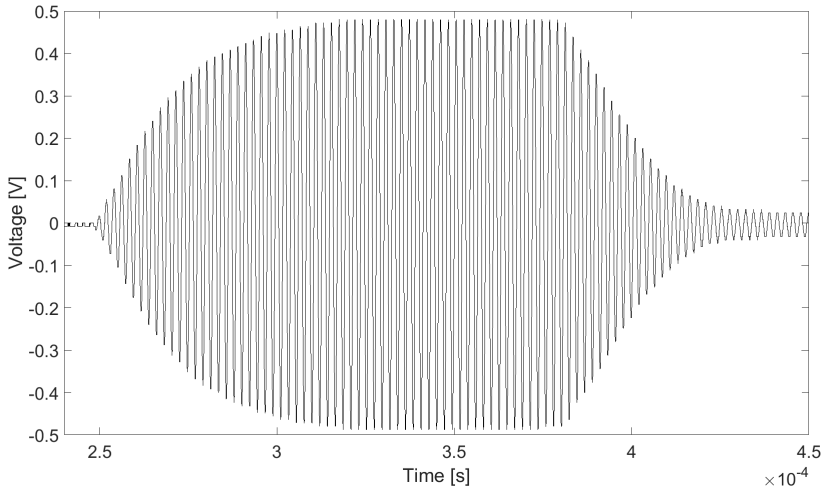

FIGURE 5.46: Zoomed in Fig. 5.45, $V(x_0, z_2, t)$. With carrier frequency $455\,kHz$

In Fig 5.46 the interval containing the transmitted direct signal is plotted. The time of arrival is $t = 0.00025s$, which is close to expected if using an averaged velocity of $c_a = 1515\,m/s$. This velocity is described in Sect. 3.4.2. The signal is overall stable.

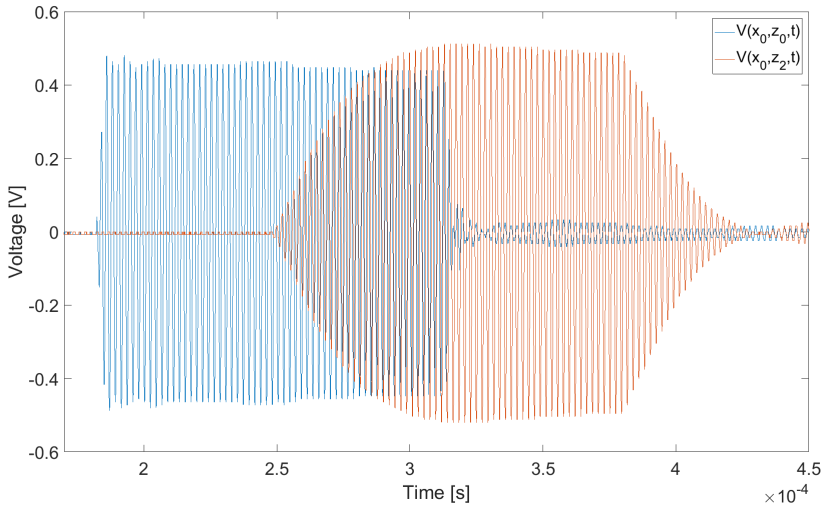

FIGURE 5.47: Zoomed in sampled voltages $V(x_0, z_0, t)$ and $V(x_0, z_2, t)$. With carrier frequency $458\,kHz$

$V(x_0, z_0, t)$ and $V(x_0, z_2, t)$ are plotted in Fig. 5.47. This is with the carrier frequency $458\,kHz$, because this is the frequency of strongest transmission. We can see the time displacement of approximately $\Delta t = 0,00007s$. In addition to the time displacement another effect of signal transmission is observed. The transmitted signal has an increased voltage, which has been noted by others e.g. [11, 27]. This is due to the excitation of leaky Lamb modes. This difference is not however on the scale seen in Fig. 5.15. Here an approximate increase of $1.12\,dB$ is observed. The ASM simulation is lossless and the on axis measurements are subject to slight deviance in position from the main-lobe. This contributes to the values not being equal.

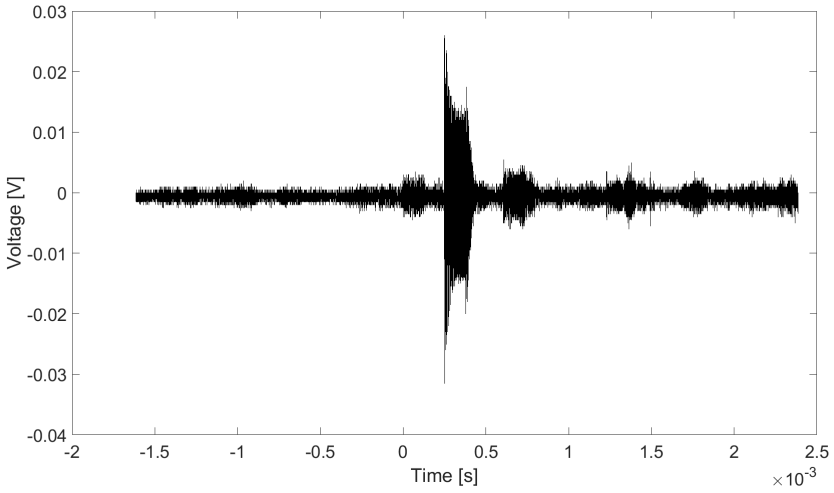

FIGURE 5.48: Sampled voltage, $V(x_0, z_2, t)$. With carrier frequency $700\,kHz$

In Fig. 5.48 the sampled time interval for $V(x_0, z_2, t)$ with $f_c = 700kHz$ is plotted. The voltage here is weaker than in other measurements resulting in the signal to noise ratio (SNR) being low. However what appears to be a signal can be seen at approximately $t = 0$. This is not caused by the direct signal as the oscilloscope is triggered by the signal generator. Compared to the sampled noise of Fig. 5.38 where we do not see the presence of such signals. Meaning they are caused by radiation from the transducer. This indicates that the burst rate of $50\,Hz$ is too high. These may be present in previous measurements, but because the SNR is higher they are not visible. There is also here a signal is visible with a TOA of $t = 0.0006\,s$ similar to Fig. 5.45. The same distinct signals at $t \approx 0.0013\,s$ and $t \approx 0.0016$, but are not as defined as previously.

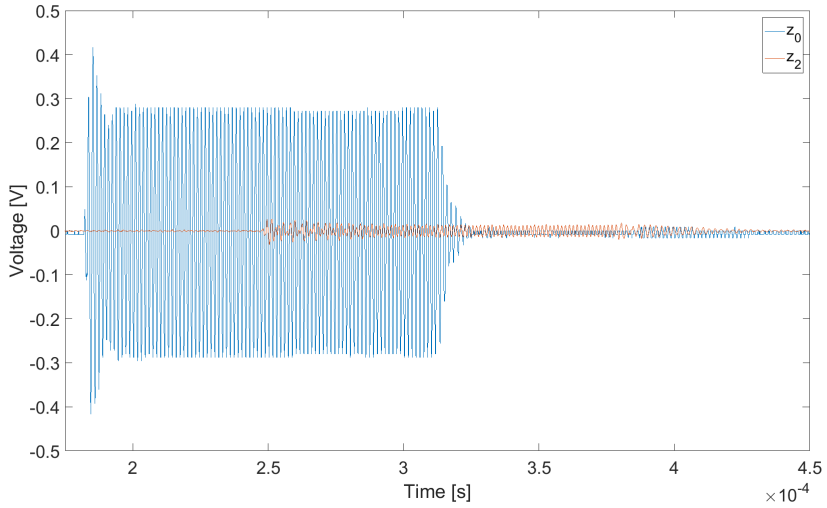

FIGURE 5.49: Zoomed in voltages from Fig 5.41 and 5.48, $V(x_0, z, t)$. With carrier frequency $700\,kHz$

When comparing the z_0 and z_2 voltages, as in Fig. 5.47, for $f = 700\,kHz$ we see in Fig. 5.49 a significant drop of $27,4dB$ between the two measurements. This drop in

voltage is due to little excitation of leaky Lamb waves. Indicating a small $|T|$ for this frequency.

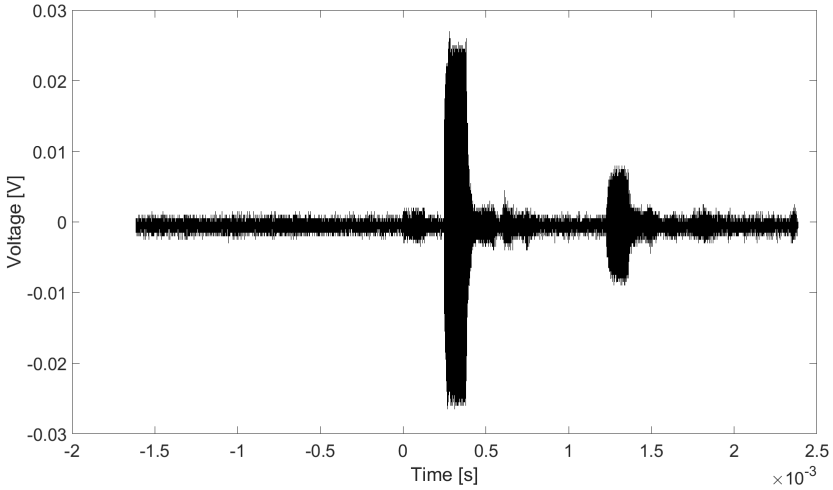

FIGURE 5.50: Sampled voltage, $V(x_0, z_2, t)$. With carrier frequency $955\,kHz$

In Fig. 5.50 the sampled interval at position z_2 , with carrier frequency $955\,kHz$, is plotted. Also here a signal at approximately $t \approx 0$. What differs in Fig. 5.50 from Fig. 5.45 and 5.48 is the lack of a significant signal at $t = 0.0006\,s$. Rather we see a signal at $t = 0.0012\,s$. The cause of this signal is unclear. The differing factor between $f_c = 455\,kHz$ and $f_c = 955kHz$ being what leaky Lamb mode is excited. If this is the cause is uncertain.

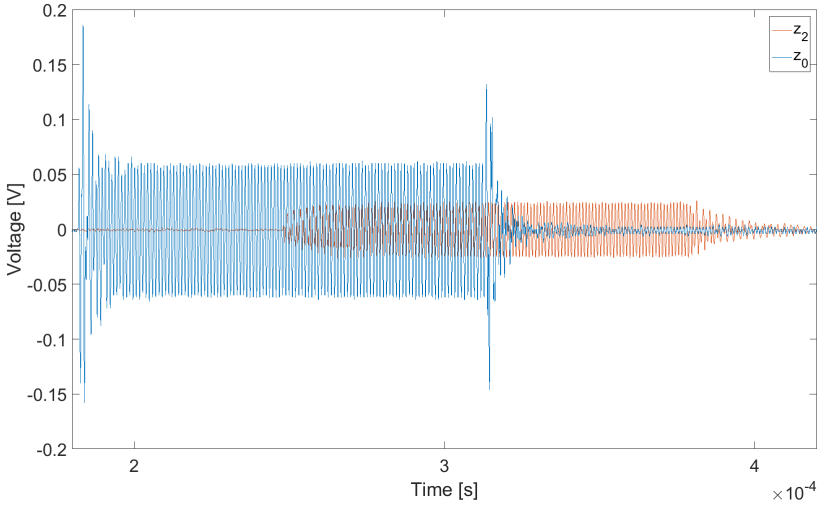

FIGURE 5.51: Zoomed in voltages from Fig 5.43 and 5.50, $V(x_0, z, t)$. With carrier frequency $955\,kHz$

Comparing the voltage at z_0 and z_2 in Fig. 5.51 we see a decrease in voltage, but not on the scale of Fig. 5.49. Here there is a drop of approximately $8,1dB$. This is not as significant a drop as in Fig. 5.49, but not an increase as seen in Fig. 5.47. This indicates a transmission coefficient lower than 1 but not as low as for $f_c = 700\,kHz$.

Through the inspection of the measurement results in the form of these waveforms several effects have been noted. The presence of reflections trailing the direct signal have been seen in all the sampled intervals. The presence of signals with TOA's before the direct signal, seen in Fig. 5.48. Finally signals that appear due to the presence of the plate. These signals do not impact the direct signal and thus do not effect the post-processing of the direct signal.

5.2.2 Pressure-to-Pressure Transfer Function

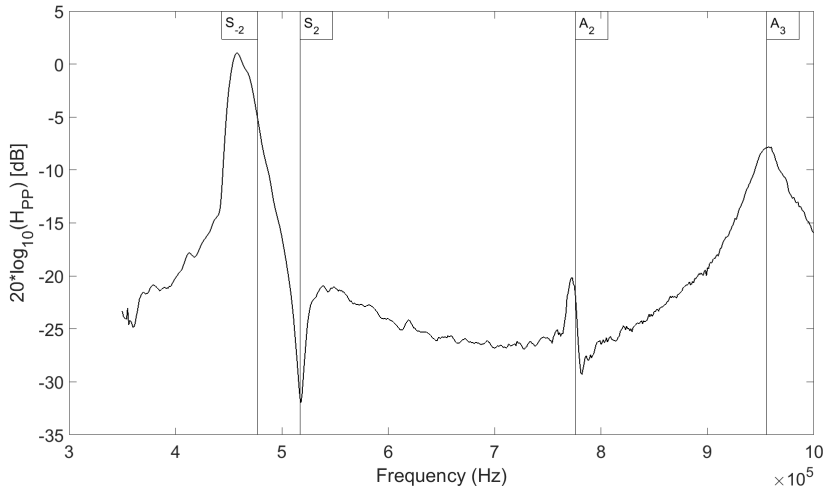

FIGURE 5.52: H_{pp} Transfer function with indicated leaky Lamb modes cut-off frequencies

The post-processing of the results from Sect. 5.2.1 is described in Sect. 3.4.3. Using Eq. 3.2 the H_{pp} transfer function is obtained. The function is plotted as $20log(H_{pp})$ in Fig. 5.52 with the measured frequencies along the horizontal axis. In addition to the the plot the theoretical plane-wave leaky Lamb modes cut-off frequencies are marked. The leaky Lamb modes were labeled previously by e.g. [11, 39, 27]. However, the mode labeled S_{-2} here has previously been labeled S_1. The S_{-2} label is consistent with [14]. The first effect to be noted is the shift in frequency for the maximum transmission from S_{-2}, which is the maximum transmission in the the plane-wave model [11], to $f = 458\,kHz$ in the measurements. This shift is noted by [11, 39, 27] and explained in [27]. The transmission at $f = 458\,kHz$ does exceed unity. This means the ratio $20log(V(x_0, z_2, 458\,kHz)/V(x_0, z_0, 458\,kHz)$ exceeds 0. The effect is explained by among others Aanes [11]. The S_{-2} mode (S_1 in [11]) is exited by plane-waves at small incidence angles at lower frequencies. A transducer with with a wide beam with none-zero incident plane-wave components will excite the S_{-2} mode at lower frequencies. The leaky Lamb modes can be regarded as narrow band pass filters in the frequency-wavenumber domain, allowing for only a small number of incident plane-wave components through the plate. But due to the behaviour of the S_{-2} mode at lower frequencies this allows for a wider range of incident plane-wave components through when the beam is at low incident angles. This is why the maximum near the S_{-2} mode exceeds unity.

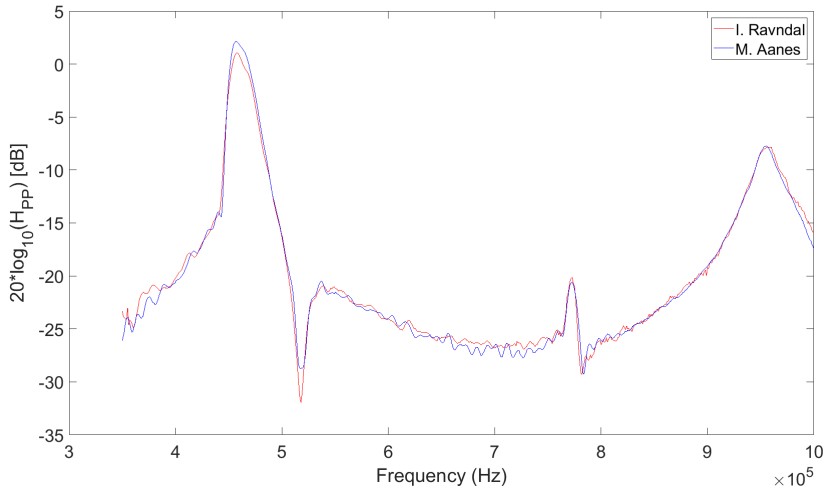

FIGURE 5.53: Comparison of H_{pp}-transfer function from Fig. 5.52 and Aanes' results [11]

In Fig. 5.53 a measurement result from Aanes [11], with permission from Aanes, is plotted against the previous plot, 5.52. There is general consensus between the results. Although at the maximum transmission Aanes' results show a higher value. This can have been caused by numerous reasons in this measurement. The positioning of the hydrophone may not have been optimal or the transducer may have been at an angle. Another discrepancy between the results is the measured maximum near the S_{-2} mode. As stated previously the the maximum was measured to $f = 458\,kHz$, while Aanes measured it to $f = 457\,kHz$, this discrepancy is prevalent on the other modes as well. The different maximums measured here and by Aanes along with simulation results done by Aanes [11] are included in Table. 5.1.

TABLE 5.1: leaky Lamb modes measured and simulated

Symbol	Frequency [kHz]			S/A	Type
	Measured	Measured M.A. [11]	Simulated (FEM) M. A. [11]		
f_{l1}^{S}	458	457	459	S_{-2}	TE
f_{t1}^{S}	518	519	518	S_2	TS
f_{t2}^{A}	773	774	774,5	A_2	TS
f_{l1}^{A}	956	955	957	A_3	TE

5.3 Transverse Measurements Results

In this section the results from the transverse measurement are presented. Firstly some waveforms are presented followed by post-processed results.

5.3.1 Transverse Waveforms

In this section som of the sampled waveforms, $V(x, z, t)$, from transverse measurements will be presented. The waveforms from positions $x = 0\,mm$, $x = 100\,mm$ and $x = 320\,mm$ will be shown for the carrier frequencies, $f_c = 455\,kHz$, $700\,kHz$ and $900\,kHz$. The waveforms are shown in order to discuss the effects that can be observed, and what impact the sampled results can have on the post-processing. Before the waveforms used in post-processing are presented results from a failed experiment are shown. These are shown because this impacts what was available for post-processing and the final results.

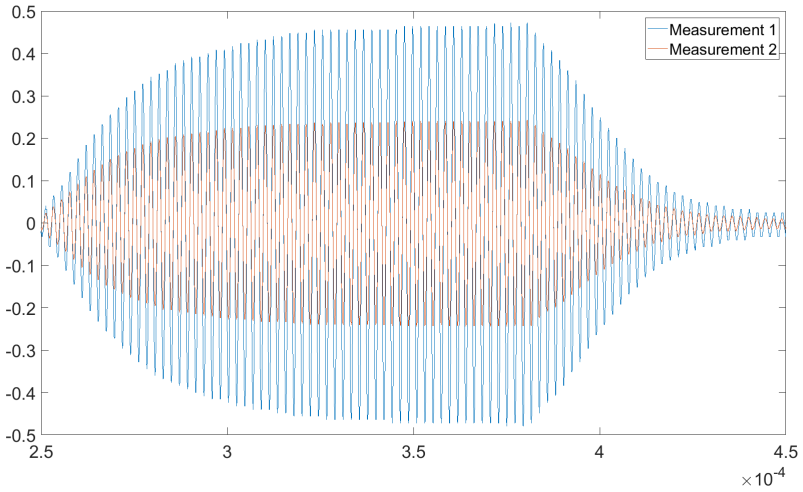

FIGURE 5.54: Comparison between Sampled voltages, $V(x_0, z_2, t)$ with carrier frequency $455\,kHz$

The two waveforms shown in Fig. 5.54 are from the transmission measurements of measurement 1 and measurement 2, detailed in Sect. 3.2.6, for the same carrier frequency $455\,kHz$ and position (x_0, z_2). A clear drop in voltage is visible between the two measurements. This drop in voltage is present for all frequencies at z_2 in measurement 2. The drop in voltage is too significant to be caused by a misplaced hydrophone or transducer and through inspection of the transmission results of measurement 2 these are deemed unusable. Therefore the results of measurement 3 are utilized for the carrier frequencies $700\,kHz$ and $955\,kHz$. The positions of the presented measurements are $x = 100\,mm$ and $x = 210\,mm$. The effects of this are discussed later on. For the $f_c = 455\,kHz$ the results from measurement 1 are used.

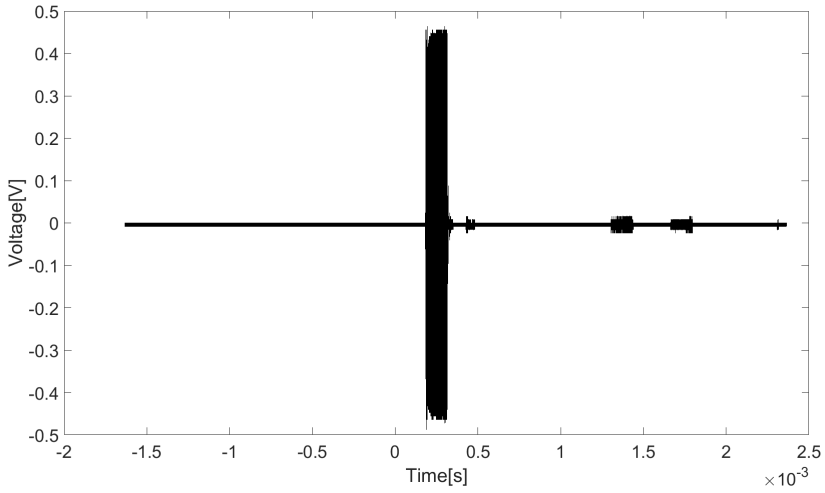

FIGURE 5.55: Sampled voltage, $V(x_0, z_0, t)$ with carrier frequency $455\,kHz$

In Fig. 5.55 the entire sampled interval for $V(x_0, z_0, t)$ with $f_c = 455\,kHz$ from the transverse measurement is plotted. When compared to Fig. 5.39 they are very similar, which is to be expected. The trailing signals have however shifted in location. This is most likely due to the change in placement of the transducer, detailed in Sect. 3.2.3.

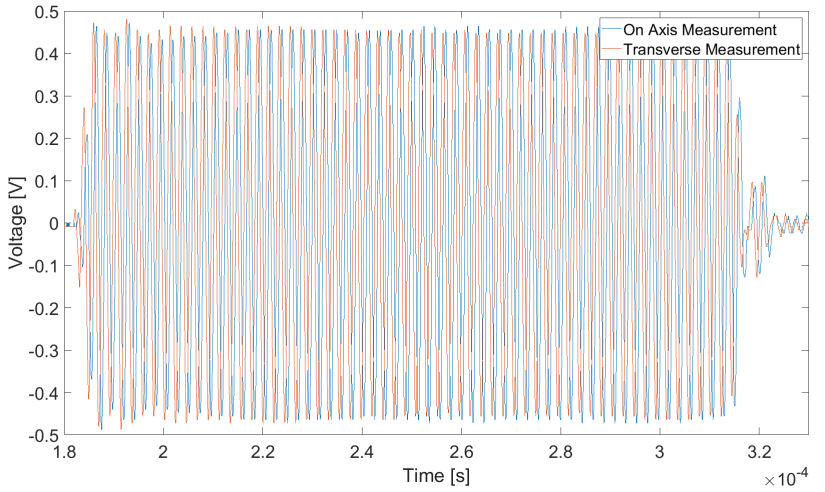

FIGURE 5.56: Comparison of sampled voltage, $V(x_0, z_0, t)$ from Fig. 5.39 and Fig. 5.55

$V(x_0, z_2, t)$ from the on-axis measurement, Fig. 5.39, and the transverse free field measurement, from Fig. 5.55 are compared in Fig. 5.56. The time of arrival differs slightly from the two signals. This can be caused by slight differences of the positioning of the hydrophone. Another possible cause can be the temperature of the water. This is logged for the on-axis measurement, but not for the transverse. The on-axis measurement had a temperature of 21.7° Celsius. The temperature for the transverse measurement is not logged as it is subject to change over the entirety of the measurement. The on-axis measurement was conducted in December and the transverse measurement was conducted in late April, so a difference in temperature of the water is not unlikely. In May the temperature of the water was logged at 23.0°

Celsius a week after the transverse measurement. This difference in temperature does influence the fluid velocity, and thereby influencing the TOA of the direct signal. For the other sampled waveforms at (x_0, z_0) and (x_0, z_2) the results from the on-axis measurements of Sect. 5.2.1 are representative.

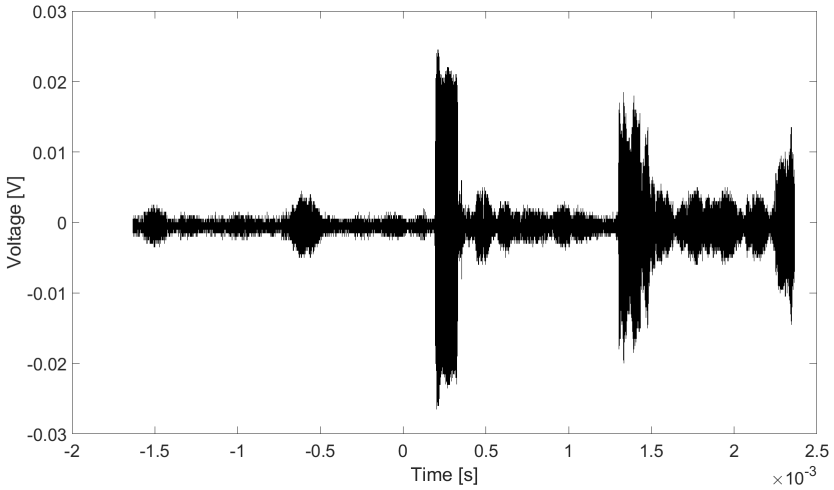

FIGURE 5.57: Sampled Voltage, $V(100mm, z_0, t)$. With carrier frequency $455\,kHz$

In Fig. 5.57 the sampled interval for $V(100, z_0, t)$ with $f_c = 455\,kHz$ is plotted. The signal is prominent with a TOA at $t = 0,000192s$ which is expected. The approximate TOA for the transverse measurement uses the Pythagorean theorem and c_f. The voltage is significantly lower when compared to that at $x = 0$ from fig 5.55. In addition to this signals can be seen on the negative side of the time axis as in Fig. 5.48. The signals in the negative t direction are also more prominent and have shifted position. This may be caused by the change in position of the transducer. The trailing signals have become more prominent as well, when compared to previous sampled intervals. This may be caused by the movement of the hydrophone and the magnitude of these signals being larger at these positions.

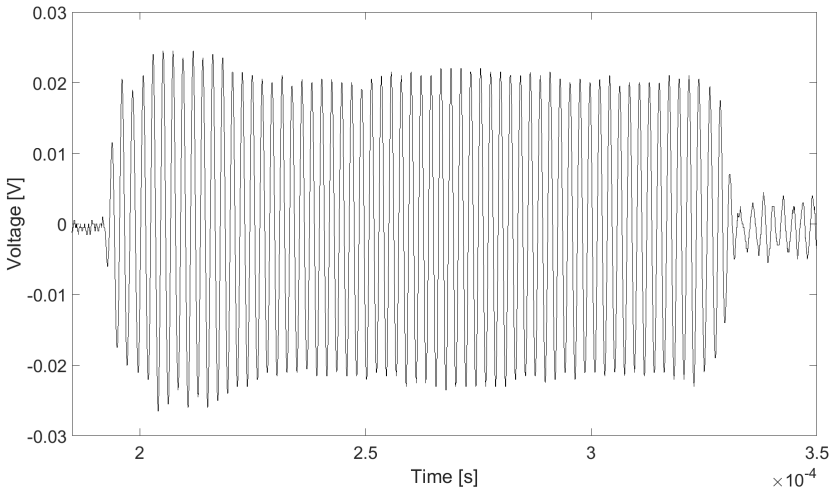

FIGURE 5.58: Zoomed in Fig. 5.57, $V(100\,mm, z_0, t)$. With carrier frequency $455\,kHz$

In Fig. 5.58 the interval containing the direct signal is plotted. When compared to 5.55 we see a significant drop in voltage. The signal has slight fluctuation, but is stable.

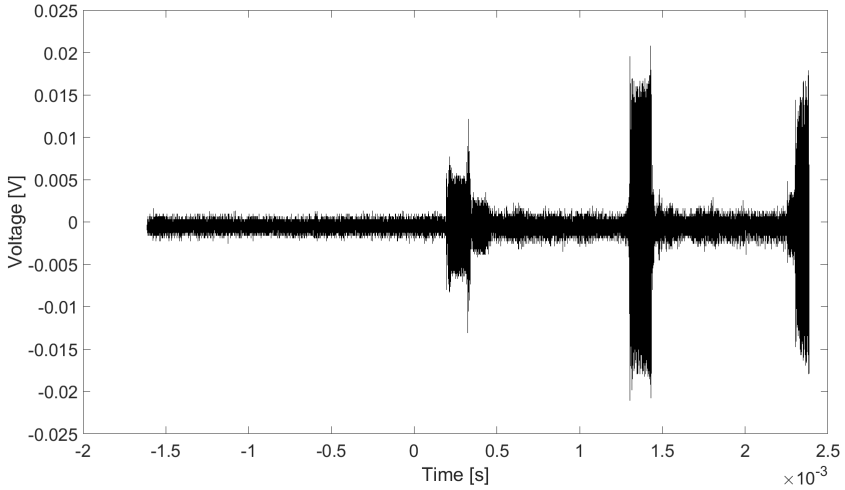

FIGURE 5.59: Sampled voltage, $V(100mm, z_0, t)$. With carrier frequency $700\,kHz$

The sampled interval $V(100, z_0, t)$ with $f_c = 700\,kHz$ is plotted in Fig. 5.59. This is from measurement 3. The transducer position is therefore in the middle of the tank, instead of to the side as in measurement 1. The signal is visible but also significantly weaker than in Fig. 5.41. Here the direct signal is closely followed by the arrival of a another signal, possibly caused by the reflection off the wall. We can discern the direct signal with a calculated approximate time of arrival of $t = 0,00019\,s$. Following the direct signal we see a stronger signal with a TOA of $t = 0.0013\,s$. This signal is $9.4\,dB$ stronger than the direct signal. This may be caused by a reflection with an incident angle to the hydrophone closer to zero. As the tolerance angle of the hydrophone is noted in Sect. 3.1.2.

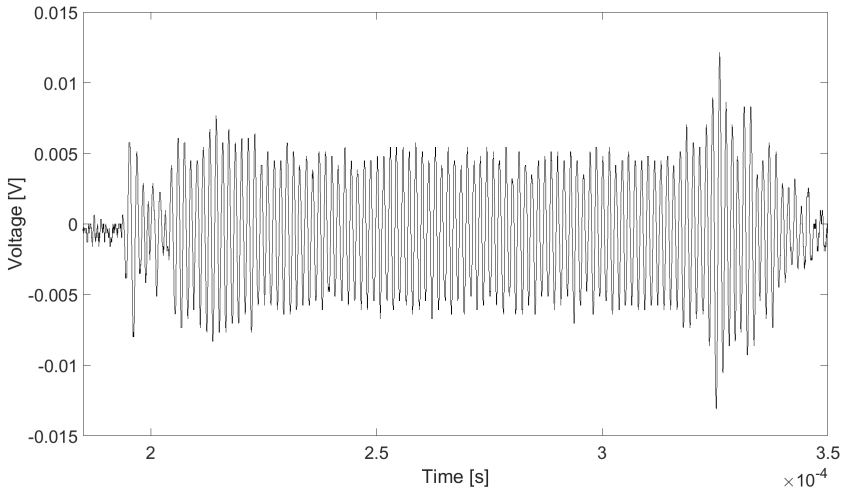

FIGURE 5.60: Zoomed in Fig. 5.59, $V(100\,mm, z_0, t)$. With carrier frequency $700\,kHz$

Zooming in on the signal portion of the sampled interval the signal in Fig.5.60 is still visible. The signal strength has also dropped by a significant margin compared to Fig. 5.42. The signal is however still reasonably stable.

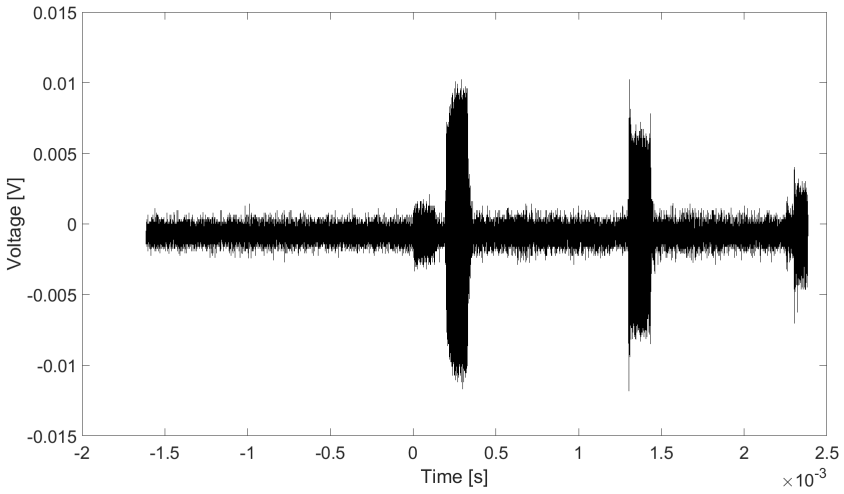

FIGURE 5.61: Sampled voltage, $V(100\,mm, z_0, t)$ with carrier frequency $f = 955\,kHz$

$V(100, z_0, t)$ with carrier frequency $f_c = 955\,kHz$ is plotted in Fig. 5.61. This measurement is from measurement 3, with the transducer in the middle of the tank. Here the signal at approximately $t \approx 0$ is visible as in previous plots. The effect noted in Fig. 5.59 where the trailing signal is stronger than the direct signal is not observed. Although the trailing signal has a TOA of $t = 0.0013\,s$, the same as in Fig. 5.59. Here again the incident angle may be factor in the magnitude of the trailing signal.

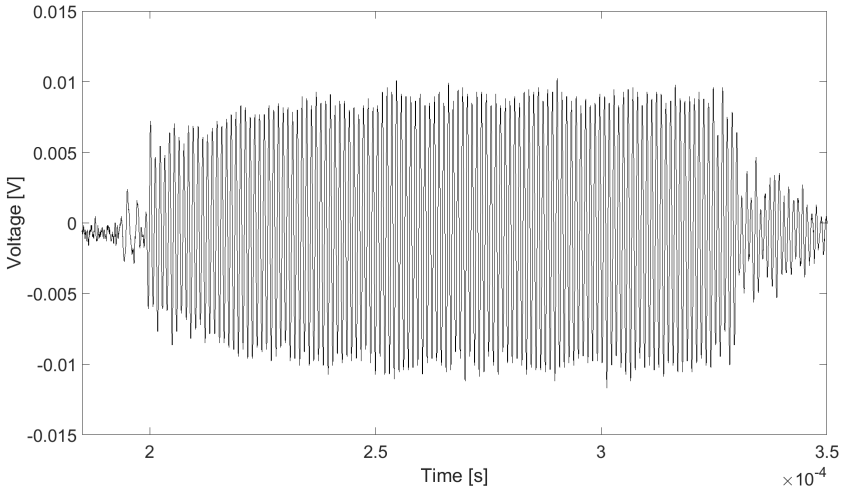

FIGURE 5.62: Zoomed in Fig. 5.61, $V(100\,mm, z_0, t)$. With carrier frequency $955\,kHz$

In Fig. 5.62 the direct signal from Fig 5.61 is shown. Compared to Fig. 5.43 the signal strength has dropped. However the signal is still stable and distinct from the noise.

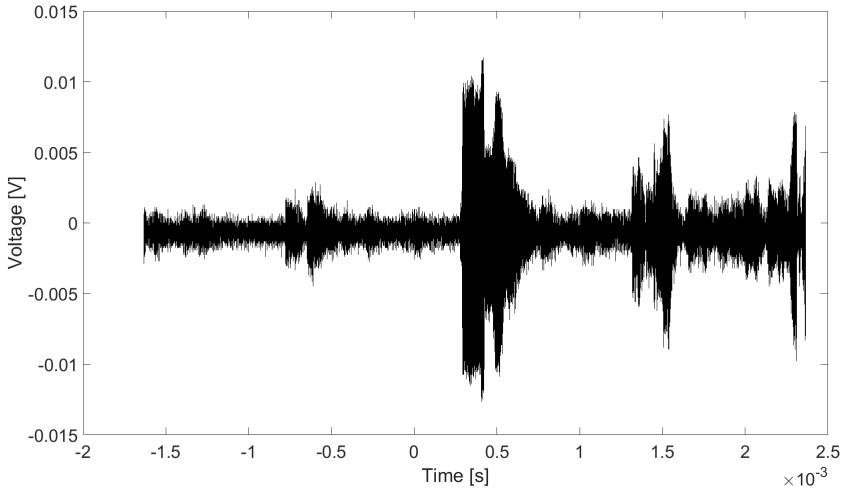

FIGURE 5.63: Sampled voltage, $V(320\,mm, z_0, t)$ with carrier frequency $f = 455\,kHz$

Fig. 5.63 shows the entirety of the sampled interval $V(320\,mm, z_0, 455\,kHz)$. Here the signal is visible with a time of arrival of $t = 0,000283$ which is expected. The signal is closely followed by what is assumed to be a reflection. Signals can be seen on the negative side of the time axis as seen previously.

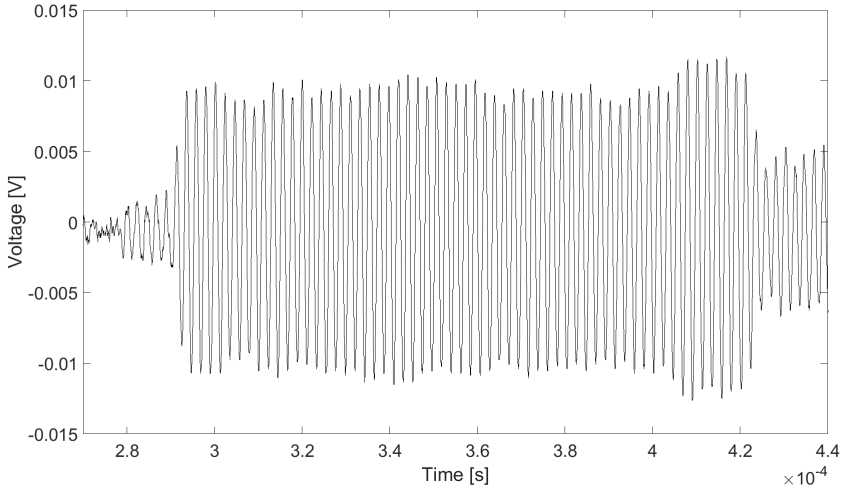

FIGURE 5.64: Zoomed in Fig. 5.63, $V(320\,mm, z_0, t)$. With carrier frequency $455\,kHz$

Looking at the direct signal from 5.63 closely in Fig. 5.64 the following signal can be seen to the right, but still the direct signal is visible and is reasonably stable.

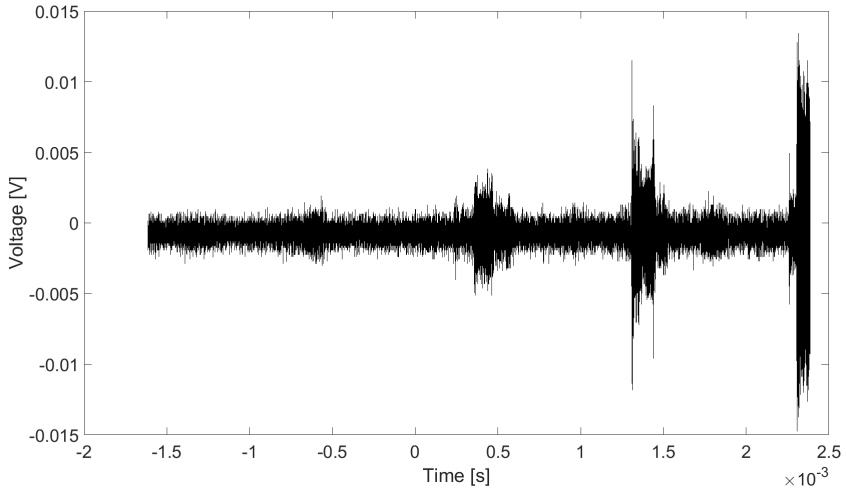

FIGURE 5.65: Sampled voltage, $V(210\,mm, z_0, t)$ with carrier frequency $f = 700\,kHz$

In Fig. 5.65 the sampled time interval of $V(210\,mm, z_0, t)$ with $f_c = 700kHz$ is plotted. The direct signal here is not visible. This is found by the estimated TOA of $t = 0.00023\,s$ for this position. At this time no signal is visible.

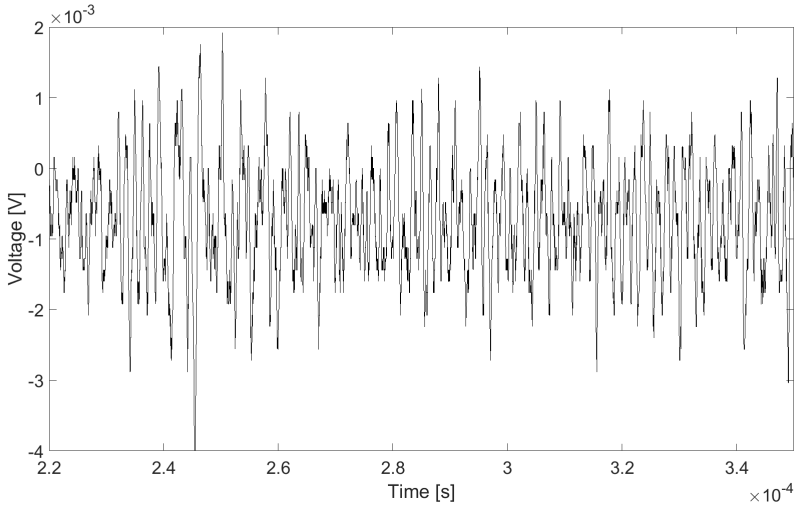

FIGURE 5.66: Zoomed in Fig. 5.65, $V(210\,mm, z_0, t)$. With carrier frequency $700\,kHz$

The time interval from Fig. 5.65 that should contain the direct signal from $V(210\,mm, z_0, t)$ with $f_c = 700kHz$ is shown in Fig. 5.65. In this interval no discernible signal is present. This means that the post-processing window from this position at this carrier frequency may not include the direct signal. In a more robust setup this would be addressed, but in this setup this is not done. Although the magnitude in this interval is minimal compared to other positions and frequencies, meaning the magnitude in the voltage spectrum is minimal as well.

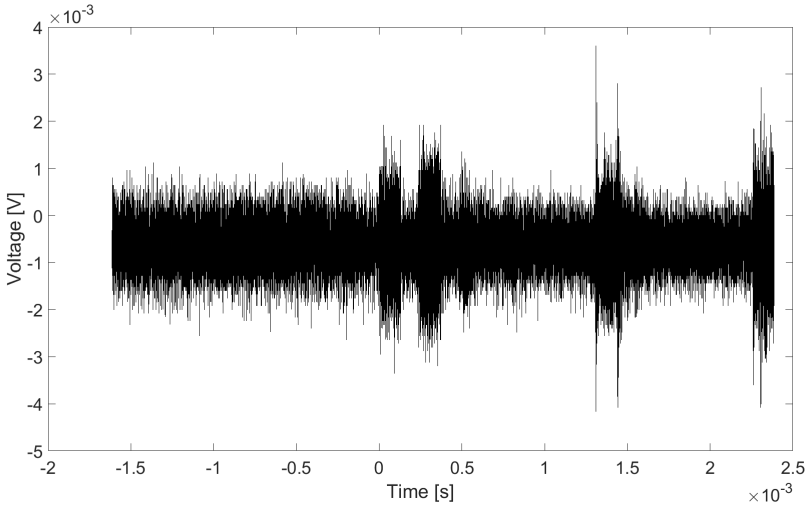

FIGURE 5.67: Sampled voltage, $V(210\,mm, z_0, t)$ with carrier frequency $f = 955\,kHz$

In Fig. 5.67 the sampled time interval of $V(210\,mm, z_0, t)$ with $f_c = 955\,kHz$ is plotted. The voltage has significantly dropped further from Fig. 5.61. The SNR is very low and the direct signal is not discernible from the other signals in the interval. Using the calculated approximate TOA of $t = 0.00023\,s$ we can identify the direct signal.

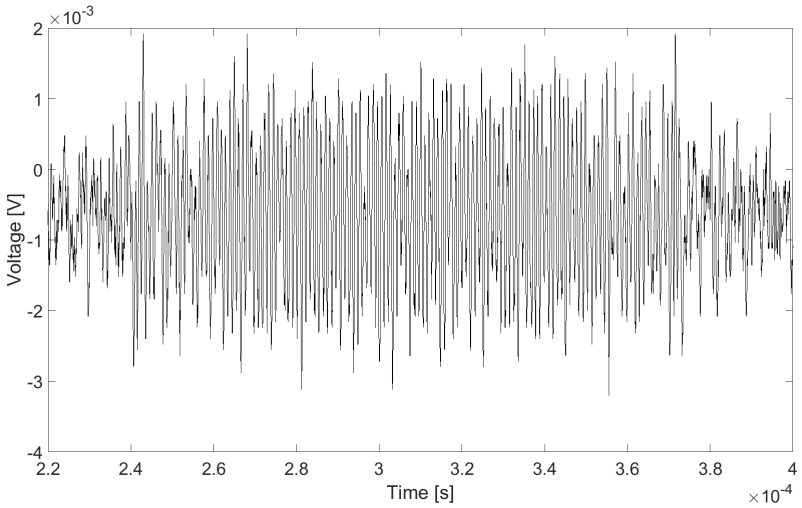

FIGURE 5.68: Zoomed in Fig. 5.67, $V(210\,mm, z_0, t)$. With carrier frequency $955\,kHz$

The interval containing the direct signal from $V(210\,mm, z_0, t)$ with $f_c = 955kHz$ is shown in Fig. 5.68. Here the signal is heavily distorted, although still discernible. This will most likely have effects on the result from the temporal fft discussed in Sect. 3.4.3, especially in regards to the phase.

In this next part the sampled intervals from the transverse transmission measurement are presented. As in the previous figures the results for $f_c = 700\,kHz$, $955kHz$ are from measurement 3 at positions $x = 100\,mm$, $210\,mm$. The results for $f_c = 455\,kHz$ are from measurement 1 at positions $x = 100\,mm$, $320\,mm$.

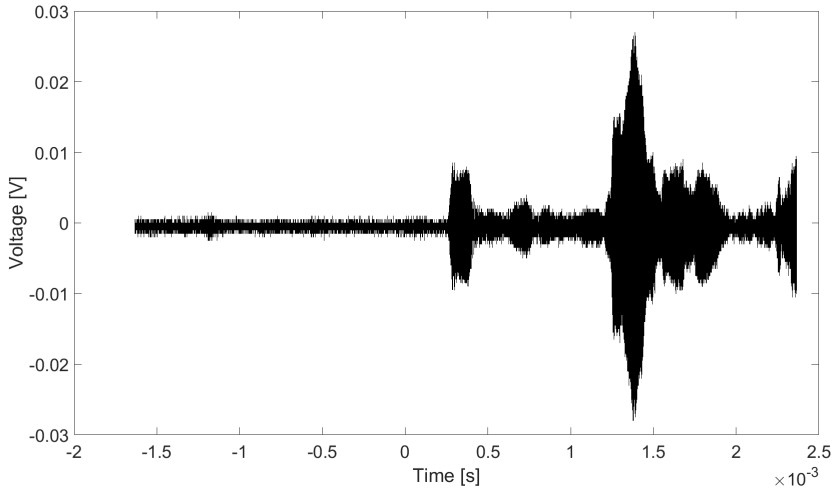

FIGURE 5.69: Sampled voltage, $V(100\,mm, z_2, t)$ with carrier frequency $f = 455\,kHz$

In Fig. 5.69 the sampled voltage for $V(100\,mm, z_2, t)$ with carrier frequency $455\,kHz$ is plotted. The direct signal has a calculated TOA of approximately $t \approx 0.00026\,s$ and is observed with an actual TOA of $t = 0.000265\,s$. Trailing the direct signal several signals from what is assumed to be reflections are seen, one large one in particular has a TOA of approximately $t \approx 0.00125\,s$. This signal is stronger than the direct signal, which may indicate an incident angle closer to zero, but this may also be caused by reflections within the plate. The TOA of this signal is however too large to accurately guess at the path.

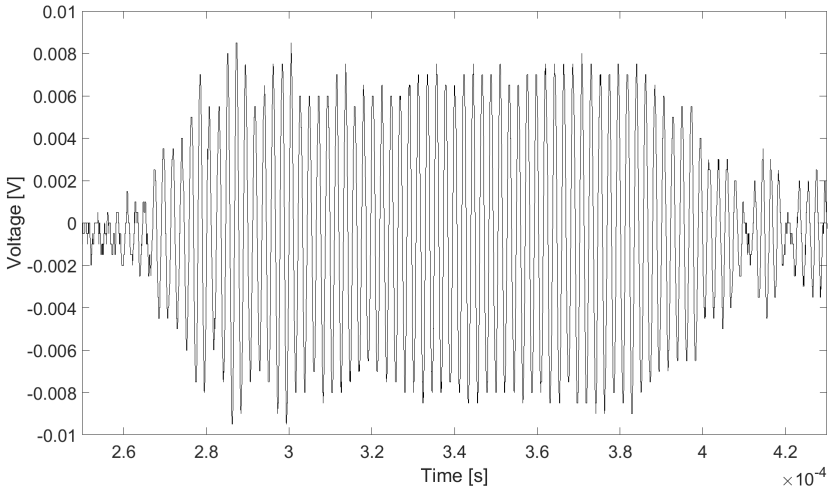

FIGURE 5.70: Zoomed in Fig. 5.69, $V(100\,mm, z_2, t)$. With carrier frequency $455\,kHz$

The interval containing the direct signal from Fig. 5.69 is shown in Fig. 5.70. The voltage shows a slight distortion of the direct signal when compared to Fig. 5.69 and a significant drop in voltage in comparison with $V(100\,mm, z_0, t)$ from Fig. 5.58. The signal is however reasonably stable over the interval.

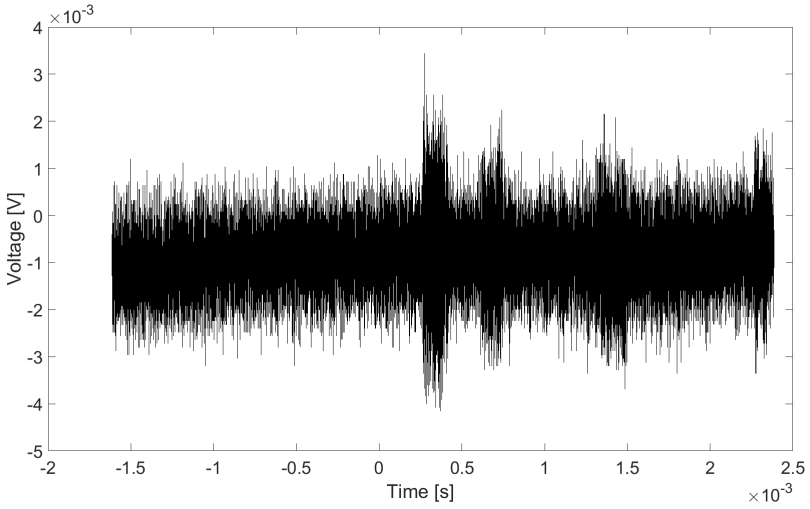

FIGURE 5.71: Sampled voltage, $V(100\,mm, z_0, t)$ with carrier frequency $f = 700\,kHz$

In Fig. 5.71 the sampled interval for $V(100\,mm, z_2)$ with $f_c = 700\,kHz$ is plotted. The direct signal is discernible even though the SNR is low. The calculated approximate TOA is $t = 0.00026\,s$ and is observed with an TOA of approximately $t = 0.000264\,s$. The precise TOA is difficult to assert as the SNR is low. In addition to the trailing signals observed in other sampled intervals what seems to be a fluctuation over the entire sampled interval is observed with a significantly lower frequency. This should be filtered out by the bandpass-filter with a lower threshold of $200\,kHz$. The cause of this fluctuation is only speculated on, but electrical interference seems likely.

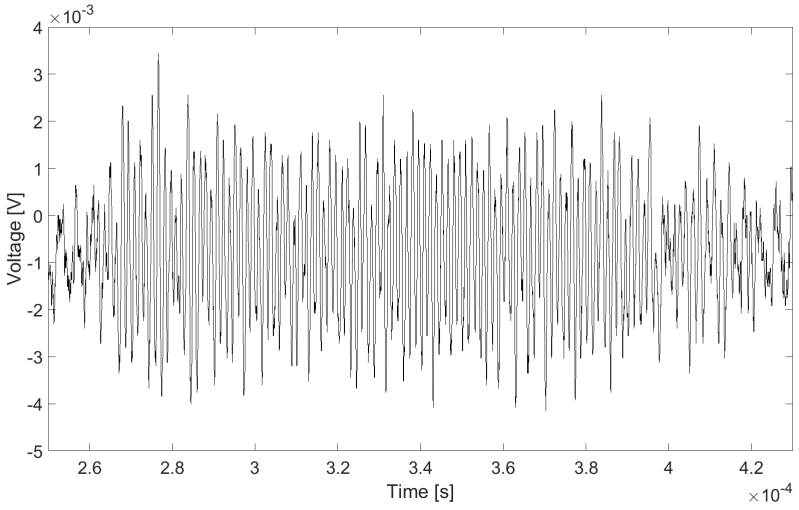

FIGURE 5.72: Zoomed in Fig. 5.71, $V(100\,mm, z_0, t)$. With carrier frequency $700\,kHz$

Fig. 5.72 shows the interval containing the direct signal from Fig. 5.72. The signal is heavily distorted and a stable interval is not observed. This will most likely affect the fft of the assigned post-processing window for this interval.

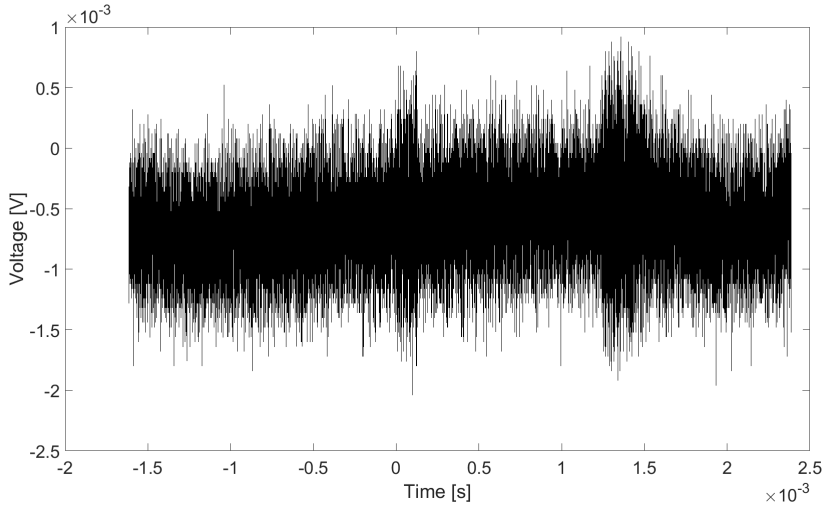

FIGURE 5.73: Sampled voltage, $V(100\,mm, z_0, t)$ with carrier frequency $f = 955\,kHz$

$V(100, z_2, 955\,kHz)$, the sampled interval with $f_c = 955\,kHz$ is plotted in Fig. 5.73. The direct signal is not visible in this plot because it is buried within the noise. This means the post-processing window for this interval may just contain noise. Also visible in the interval is the fluctuation of the entire sampled interval.

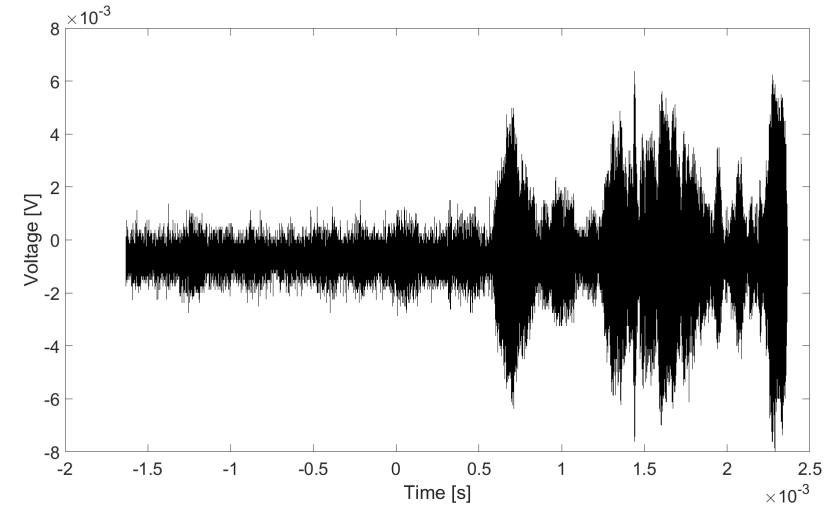

FIGURE 5.74: Sampled voltage, $V(320\,mm, z_0, t)$ with carrier frequency $f = 455\,kHz$

Plotting the sampled interval of $V(320\,mm, z_2, t)$ with $f_c = 455\,kHz$ in Fig. 5.74 a large signal can be seen at approximately $0.0006\,s$ but the calculated approximate time of arrival would place the direct signal around $t \approx 0.00033\,s$. This means the signal is buried in noise, and not visible.

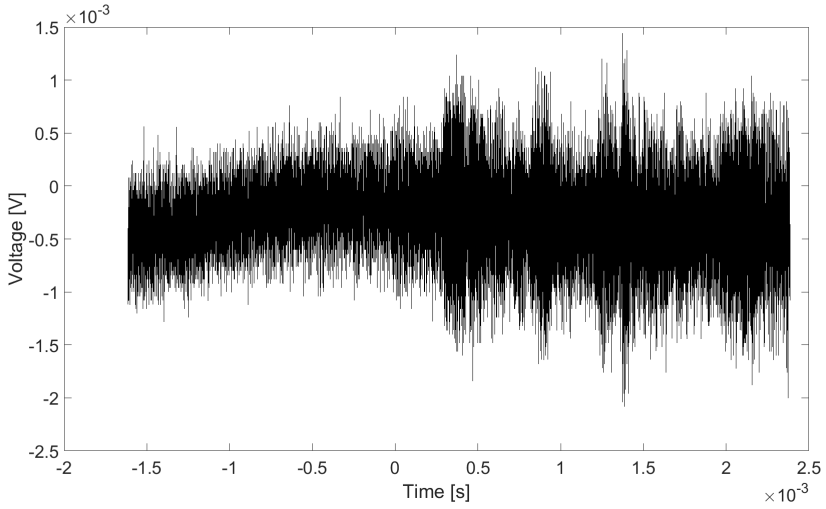

FIGURE 5.75: Sampled voltage, $V(210\,mm, z_2, t)$ with carrier frequency $f = 700\,kHz$

In Fig. 5.75 the sampled interval for $V(210\,mm, z_2, t)$ with $f_c = 700\,kHz$ is plotted. The direct signal has a calculated approximate TOA of $t = 0.000284\,s$ and a signal with an observed TOA of $t = 0.000291$ is visible. The underlying fluctuation here is noticeable and shifts the centre of the sampled interval below zero.

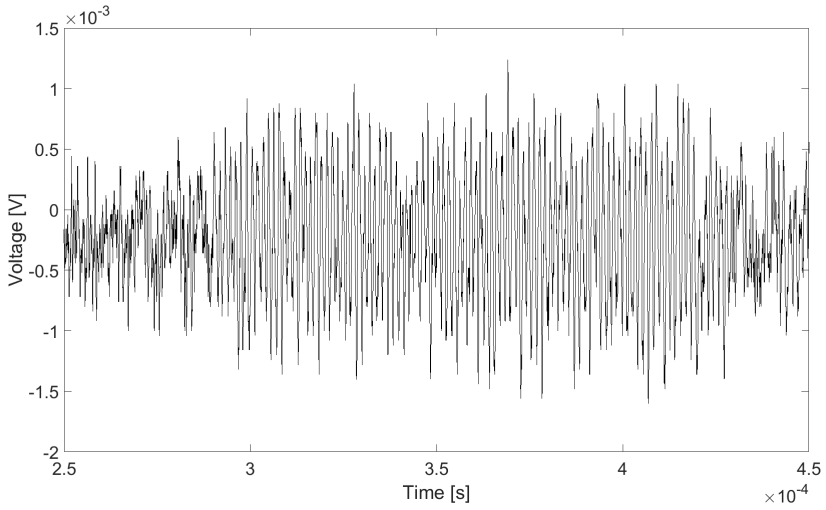

FIGURE 5.76: Zoomed in Fig. 5.65, $V(210\,mm, z_2, t)$. With carrier frequency $700\,kHz$

Fig. 5.76 shows the interval containing the direct signal from Fig. 5.75. The signal is heavily distorted but still visible.

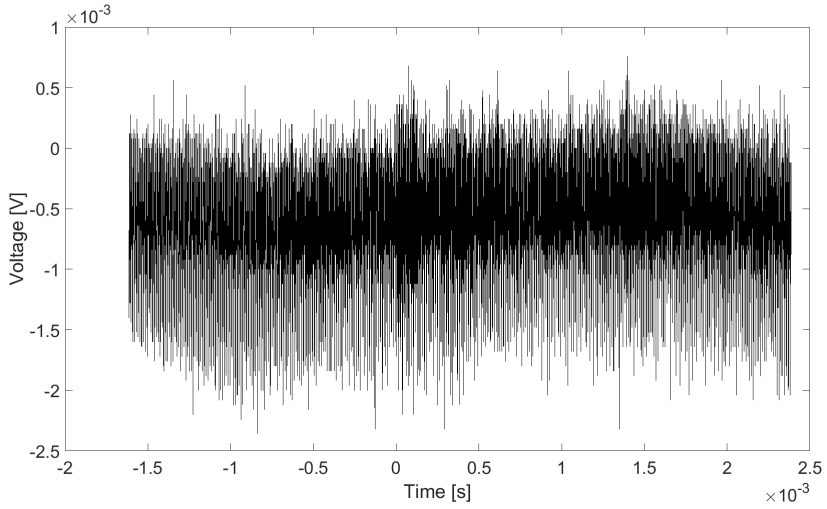

FIGURE 5.77: Sampled voltage, $V(210\,mm, z_2, t)$ with carrier frequency $f = 955\,kHz$

In Fig. 5.77 the sampled interval $V(210\,mm, z_2, 955\,kHz)$ is plotted. No distinguishable signal is visible within the interval. The fluctuation of the sampled interval is visible throughout. Another effect of this fluctuation is observable where $V = 0\,V$ is not the center value of $V(210\,mm, z_2, t)$.

Through the inspection of the sampled intervals of $V(x, z, t)$ from the transverse measurements many effects have been noted. Some of which were also noted in the on-axis results. The main effect impacting the post-processing of the results is the distortion of the received signals and lack of visible signals all together. As has been mentioned previously, the assignment of the post-processing window does not address these effects. The magnitude of the processed results in the areas of high SNR should not be affected by this, but areas of low SNR and especially where the signal is not visible are most likely affected. This could be artificially higher magnitude at a position for a frequency. The fluctuation of the sampled interval may also have this effect on the post-processed results. These effects likely contributed to the phase of the processed signals being unusable.

5.3.2 Symmetrical Transverse Measurement Results

The post-processed results of measurement 3 are shown here. The measurement is detailed in Sect. 3.2.5. Examples of the waveforms are shown in Sect. 5.3.1. Using the fft function of Matlab and extracting the maximum voltage amplitude and phase, detailed in 3.4.3, we obtain the the voltage spectrum $V(x, z, f)$.

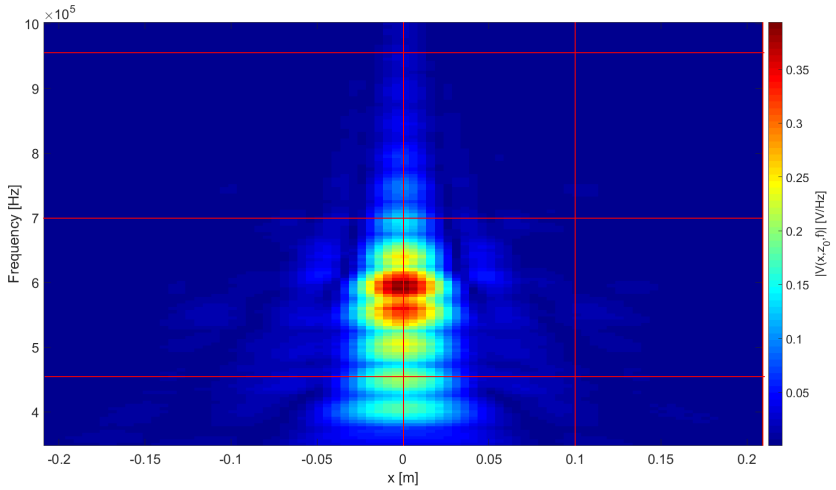

FIGURE 5.78: Measured voltage spectrum magnitude, $|V(x, z_0, f)|$

The magnitude of the measured voltage spectrum, $V(x, z_0, f)$ is plotted in Fig. 5.78. Along the vertical axis of the plot is the frequency, along the horizontal axis is the hydrophone position x and the colour-bar indicates the magnitude of $V(x, z, f)$. What we see in Fig. 5.78 is the transducers output for each frequency. The lines indicate at what frequency and position the waveforms were shown. Although the waveforms for $f_c = 455\,kHz$ were from measurement 1 and at $x = 320\,mm$, not $x = 210\,mm$. As expected the maximum output of the transducer is at $f = 575\,kHz$ [11]. We also see slight minimums along the frequency axis at x_0.

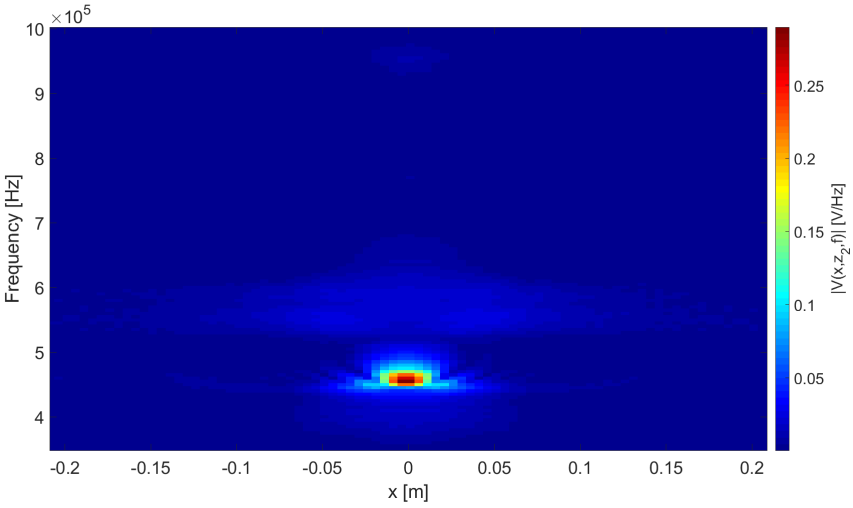

FIGURE 5.79: Measured voltage spectrum magnitude, $|V(x, z_2, f)|$

In Fig. 5.79 the magnitude of the measured transmitted voltage spectrum $V(x, z_2, f)$ is plotted. The lines from Fig. 5.78 are also applicable in this figure. In this figure

we see a small area of high voltage magnitude. This area surrounds the measured frequency of maximum transmission, from Fig. 5.52, and extends slightly along the x-axis before decreasing rapidly. We also see a larger area lower voltage around the frequency 575 kHz which is to be expected as this correspond to the most efficient frequencies of the transducer [11].

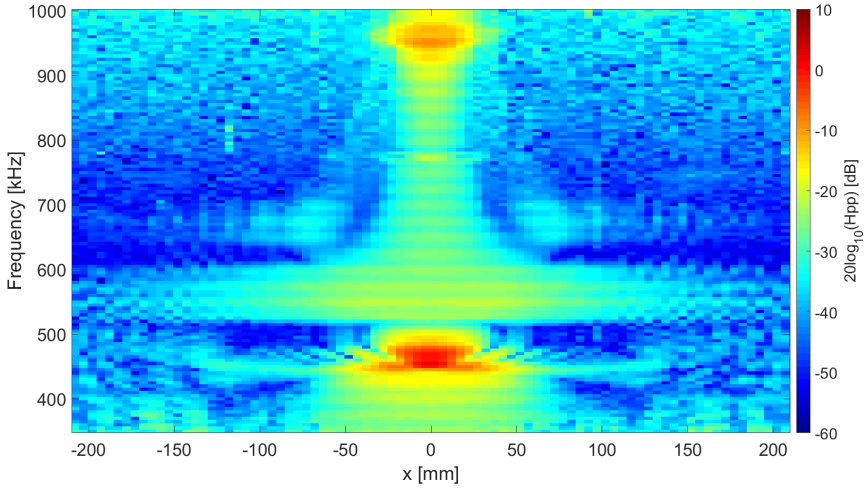

FIGURE 5.80: Measured magnitude of the H_{pp} transfer function

With the measurements from Fig. 5.79 and the measurements along the x_0-line from Fig. 5.78, and using the pressure-to-pressure transfer function Eq. 3.2. We can map the magnitude of the H_{pp} transfer function as a function of frequency and position In Fig. 5.80. Here we see for what positions and frequencies there is the greatest amount of transmission. The segment stretching from $f = 350\,kHz$ to $1\,MHz$ along x_0 is the H_{pp} of the plot in Fig. 5.52. We see the greatest amount of transmission along x_0. Although other areas such as just below the measured S_{-2} and between $500\,kHz$ and $600\,kHz$ have wider areas, in the x-domain, of transmission. This plot was also presented by M. Aanes using a FEM simulation [11]. In this simulation the transducer was modelled after the piezoelectric transducer used in these measurements.

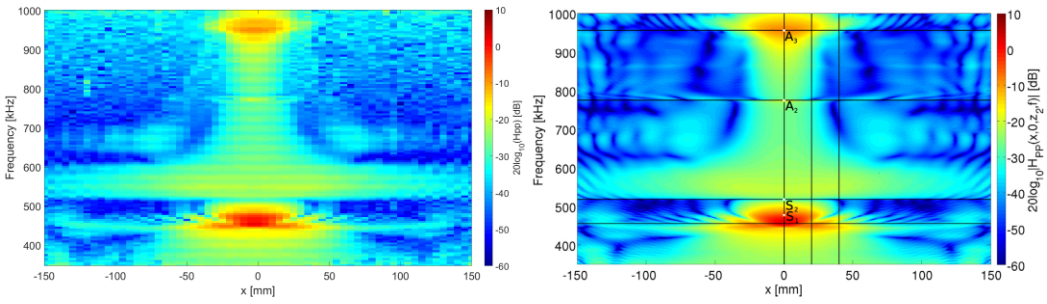

FIGURE 5.81: left: Measured magnitude of the H_{pp} transfer function Right: FEM simulated magnitude of the H_{pp} transfer function by Aanes [11] with leaky Lamb modes marked

In Fig. 5.81 the measured plot from Fig. 5.80 (left) and Aanes' simulated results [11] (right) are compared. The x-extent of 5.80 has been shortened in order to match Aanes' results. The comparison is only possible visually as the data for this simulation were not available. However they are visually very similar. The measured

plot has a lower resolution because of the parameters of the measurement. Aanes' simulation marks the simulated leaky Lamb modes. These are also visible in the measured results with the same shape of the area around the S_{-2} mode (S_1 in [11]). The larger area of transmission between 500 kHz and 600 kHz is also visible in both plots. A slight difference can be seen in the area between 350 kHz and 420 kHz. Here the simulation shows a wider range of transmission in the x-domain.

5.3.3 Voltage Spectrum Components

After the temporal Fourier transform described in 3.4.3, we can plot the magnitude of the $V(x, z, f)$ components for each frequency. In this section the magnitude of the voltage spectrum components for the carrier frequencies from Sect. 5.3.1 will be presented. These plots show the magnitude of the values that are used in Hankel transformation described in Sect. 4.2.3. All the plots are adjusted if needed along the horizontal axis such that the highest voltage value is at $x = 0$ which is needed for the Hankel transformation. Because the results of measurement 2 were not used, the results from measurement 3 are utilized. Because the Hankel transformation assumes symmetry around the z-axis only the positive x-values from measurement 3 are used in the Hankel transformation.

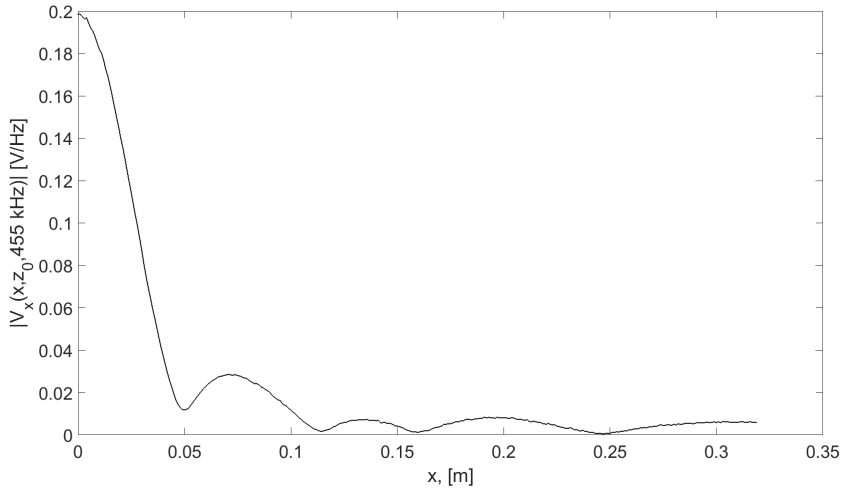

FIGURE 5.82: Magnitude of voltage spectrum component $V(x, z_0, 455kHz)$, from measurement 1

In Fig. 5.82 the magnitude of the voltage spectrum component $V(x, z_0, 455\,kHz)$ is plotted. These results are obtained from measurement 1. This is the corresponding measurement result to the simulation result in Fig. 5.14. A clear main-lobe is visible with defined side-lobes. The peak of $|V(x, z_0, 455\,kHz)|$ was 1 mm off $x = 0$ and was shifted 1 mm in the negative x-direction. At $|V(320\,mm, z_0, 455\,kHz)|$ the magnitude is 5.8 V/Hz. This may cause issues in the Hankel transformation that will be discussed in the next section, Sect. 5.3.4.

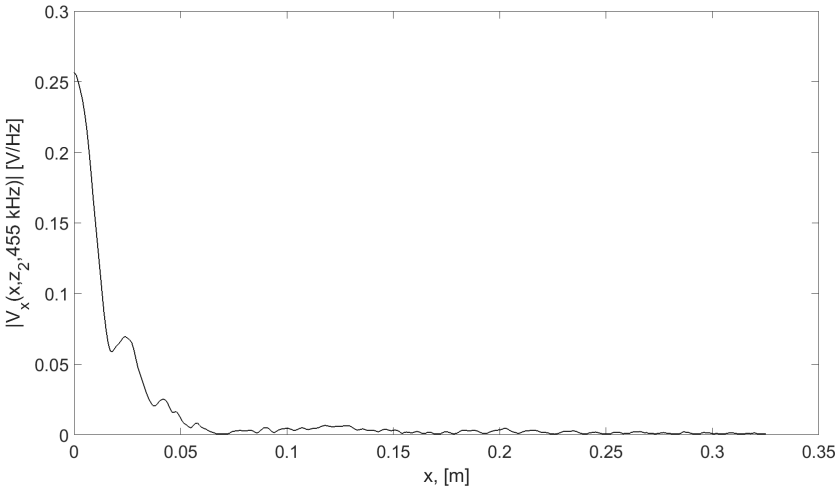

FIGURE 5.83: Magnitude of voltage spectrum component $V(x, z_2, 455kHz)$, from measurement 1

The magnitude of the voltage spectrum component $V(x, z_2, 455\,kHz)$ is plotted in Fig. 5.83. This result is from measurement 1. This is the corresponding measurement result to the simulation result in Fig. 5.15. In the plot a clear main-lobe is visible with a secondary peak at $x = 24\,mm$. We see the effects of transmission near the S_{-2} mode discussed in Sect. 5.2.2. The main lobe is narrower than in Fig. 5.82 and an increase in voltage is observed. This is not at the measured transmission measurement maximum of $458\,kHz$, but the effects are observable in Figs. 5.82 and 5.83. The maximum of $|V(x, z_2, 455\,kHz)|$ was off by $-5\,mm$ and was shifted $5\,mm$ in the positive x-direction. This means the x-limit for the Hankel transformation of $V(x, z_2, 455\,kHz)$ is $325\,mm$, but because the the limits of the z_0 and z_2 measurements need to be equal, the x-limit is set to $319\,mm$. This results in a resolution in the wavenumber-domain of $\Delta h_x = 19.7\,rad/m$. With a spatial step of $\Delta x = 1\,mm$ the extent in the wavenumber-domain is $h_{x,max} = 6283.2\,rad/m$

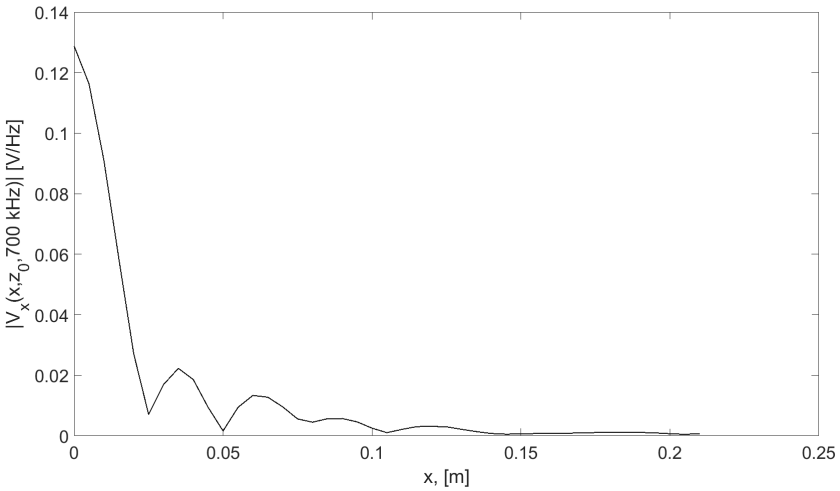

FIGURE 5.84: Magnitude of voltage spectrum component $V(x, z_0, 700kHz)$, from measurement 3

In Fig. 5.84 the magnitude of the voltage spectrum component $V(x, z_0, 700\,kHz)$ is plotted. This result is from measurement 3. This is the corresponding measurement

result to the simulation result of Fig. 5.16. The lack spatial resolution of measurement 3, $\Delta x = 5\,mm$, can be observed here when compared to Fig. 5.82 which has a spatial resolution of $1\,mm$. The maximum of $V(x, z, 700\,kHz)$ was found at $x = 0$, so no shift was needed.

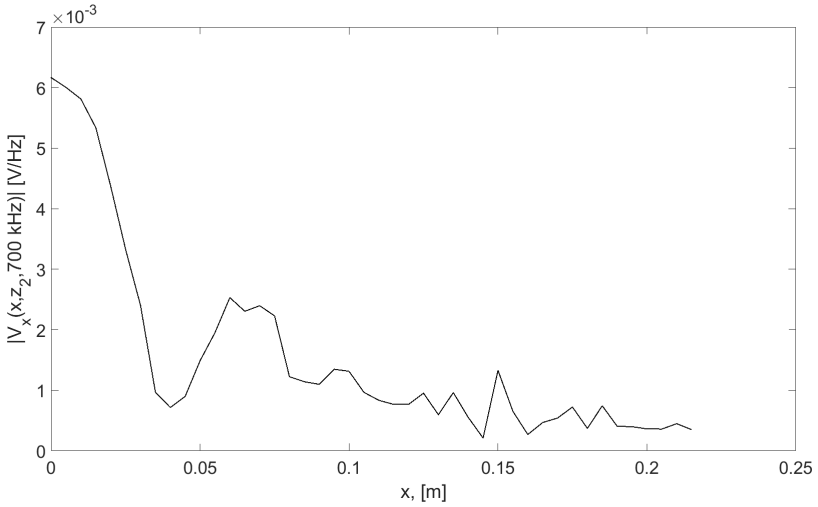

FIGURE 5.85: Magnitude of voltage spectrum component $V(x, z_2, 700kHz)$, from measurement 3

In Fig. 5.85 the magnitude of the voltage spectrum component $V(x, z_2, 700\,kHz)$ is plotted. These results are from measurement 3. This plot are the corresponding measurement results to the simulation results in Fig. 5.17. The maximum of $|V(x, z_2, 700\,kHz)|$ was found at $-5\,mm$. The plot was shifted $5\,mm$ in the positive x-direction.

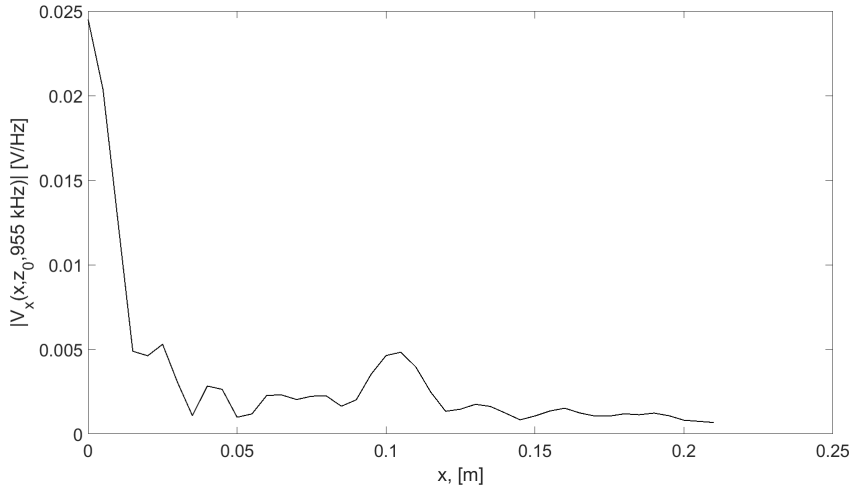

FIGURE 5.86: Magnitude of voltage spectrum component $V(x, z_0, 955kHz)$, from measurement 3

The magnitude of $V(x, z_0, 955\,kHz)$ is plotted in Fig. 5.86. These results are from measurement 3. This is the corresponding measurement result to the simulation result in Fig. 5.18. As in Fig. 5.84 the peak was observed at $x = 0\,mm$, so no shift is needed.

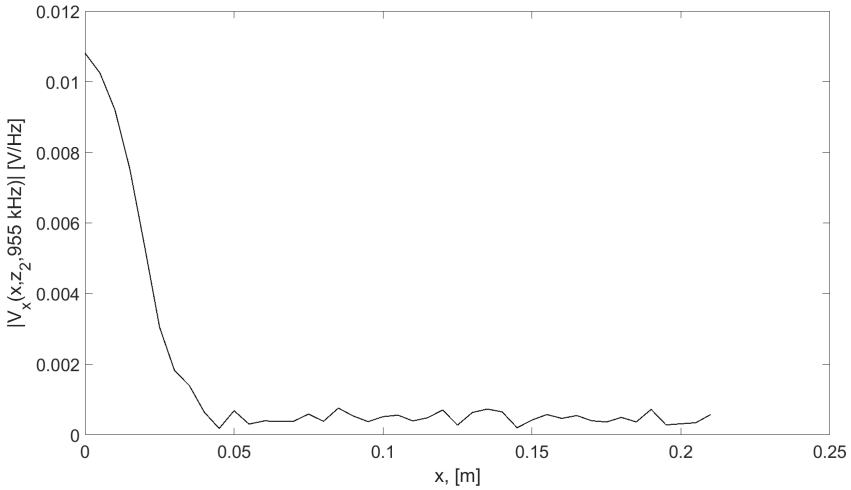

FIGURE 5.87: Magnitude of voltage spectrum component $V(x, z_2, 955kHz)$, from measurement 3

In Fig. 5.87 the magnitude of the voltage spectrum component $V(x, z_2, 955\,kHz)$ is plotted. These results are from measurement 3. These are the measurement results corresponding to the simulation results of Fig. 5.19. An effect of the lower spacial resolution is observed in this plot when compared to Fig. 5.92. Here the maximum of $|V(x, z_0, 955\,kHz)|$ is observed at $x = 0\,mm$ compared to $x = -5\,mm$ of $V(x, z_2, 700\,kHz)$. This can not have been caused by movement of the hydrophone as it is not moved between measurements at the same x-position. This is most likely caused by the actual maximum being somewhere between $x = -5$ and $x = 0$. Due to this fact the value of x_0 is not shifted. This results in an x-limit for the Hankel transformation of $210\,mm$ for measurement 3. The resolution in the wavenumber-domain is $\Delta h_x = 29.9\,rad/m$. With a spatial resolution of $\Delta x = 5\,mm$ the extent in the wavenumber domain is $h_{x,max} = 1256.6\,rad/m$. This also results in the peak of $V(x, z_2, 700\,kHz)$ not being included in the transformation.

5.3.4 Voltage Wavenumber Spectrum

In this section the voltage wavenumber spectra $V(h_x, z, f)$ obtained through the Hankel transformation of the voltage spectrum components of $V(x, z, f)$ from Sect. 5.3.3. The Hankel transformation is detailed in Sect. 5.3.4. These plots are the equivalent measured results to the pressure wavenumber spectrum, $|P(\eta_r, z, f)|$.

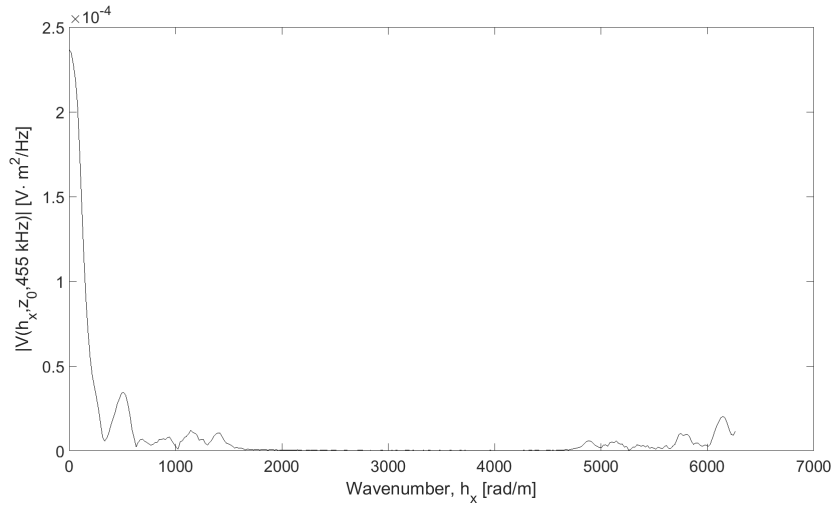

FIGURE 5.88: Voltage wavenumber spectrum, $|V(h_x, z_0, 455kHz)|$

The magnitude of the voltage wavenumber spectrum $V(h_x, z_0, 455\,kHz)$ is plotted in Fig. 5.88. Along the horizontal axis is the horizontal wavenumber h_x and along the vertical axis is the magnitude of $V(h_x, z_0, 455\,kHz)$. $V(h_x, z_0, 455\,kHz)$ was Hankel transformed from the spatial distribution $V(x, z_0, 455\,kHz)$ of Fig. 5.82 along with the complex component of the phase. The resolution and extent of this plot is $\Delta h_x = 19.7\,rad/m$ and $h_{x,max} = 6283.2\,rad/m$. $V(h_x, z_0, 455\,kHz)$ has a clear peak at $h_x = 0$ and smaller peaks further along h_x. From theory we know for this frequency $h_f = 1925.2\,rad/m$ meaning the values above this should be zero as this is the evanescent region. However we see an increase in magnitude towards the end of h_x-axis. As mentioned in Sect. 5.3.3 the magnitude at x_{max} for $V(x, z_0, 455\,kHz)$ is not zero. This abrupt end in the voltage spectrum component can cause this rise in magnitude of $V(h_x, z_0, 455\,kHz)$ at larger h_x-values as an aliasing effect. This increase is also seen in the simulated results from Sect. 5.1.5 in Fig. 5.26, but not to this degree, although the simulated results were not simulated to $6283\,rad/m$.

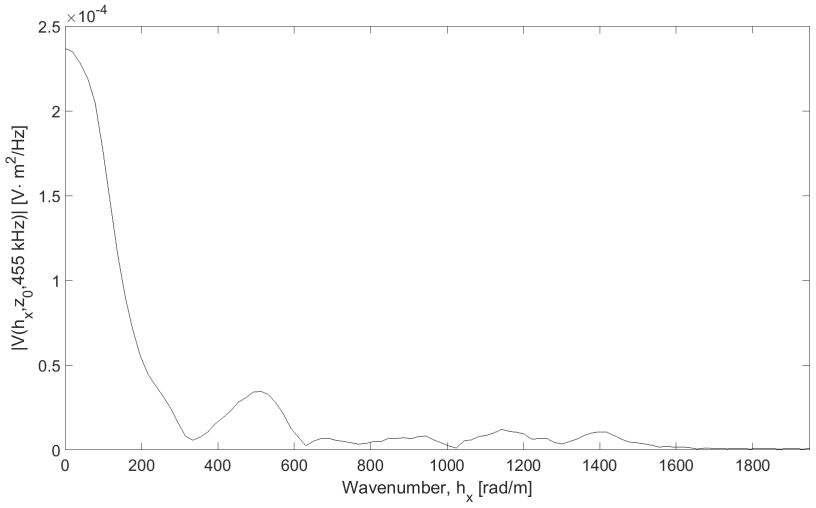

FIGURE 5.89: Zoomed in $|V(h_x, z_0, 455kHz)|$, from Fig. 5.88

In Fig. 5.89 we see the voltage wavenumber spectrum up to the theoretical singularity point of $\eta = h_f$ from Fig. 5.88. No increase in magnitude is seen towards $h_x = h_f$.

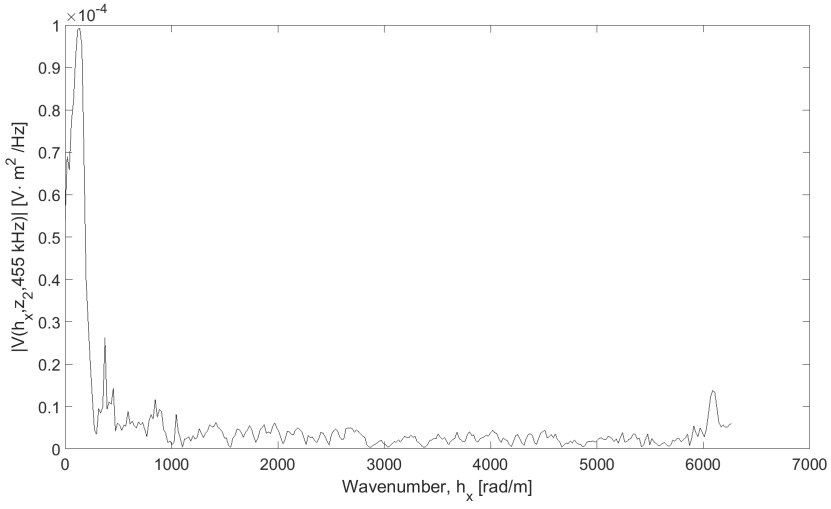

FIGURE 5.90: Voltage wavenumber spectrum, $|V(h_x, z_2, 455kHz)|$

In Fig. 5.90 the magnitude of the voltage wavenumber spectrum $V(h_x, z_0, 455\,kHz)$ is plotted. This is the measurement result equivalent to the simulation result of Fig. 5.28 and was Hankel transformed from the voltage spectrum component in Fig. 5.102 along with the phase component. In Fig. 5.90 we see the maximum is not at $h_x = 0$ which is in agreement with the simulation in Fig. 5.28 and the theoretical transmission coefficient. Here we also see an increase in magnitude further along the h_x-axis. Although the magnitude does not seem to approach zero throughout the spectrum.

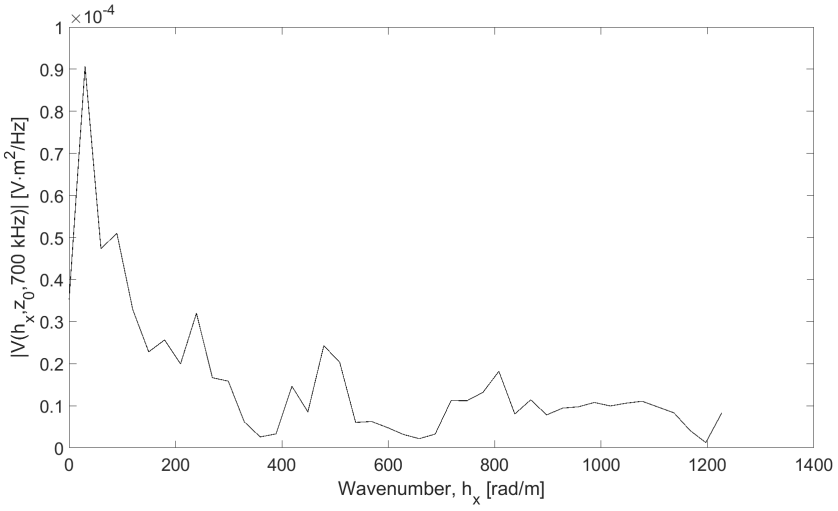

FIGURE 5.91: Voltage wavenumber spectrum $|V(h_x, z_0, 700kHz)|$, from Fig. 5.90

The magnitude of the voltage wavenumber spectrum $|V(h_x, z_0, 700\,kHz)|$ is plotted in Fig. 5.91. This was Hankel transformed from the results shown in Fig. 5.84 along with the phase component. The effect of the measurement parameters from measurement 3 are visible here. The plot ends well before the evanescent region after $\eta_r = h_f$.

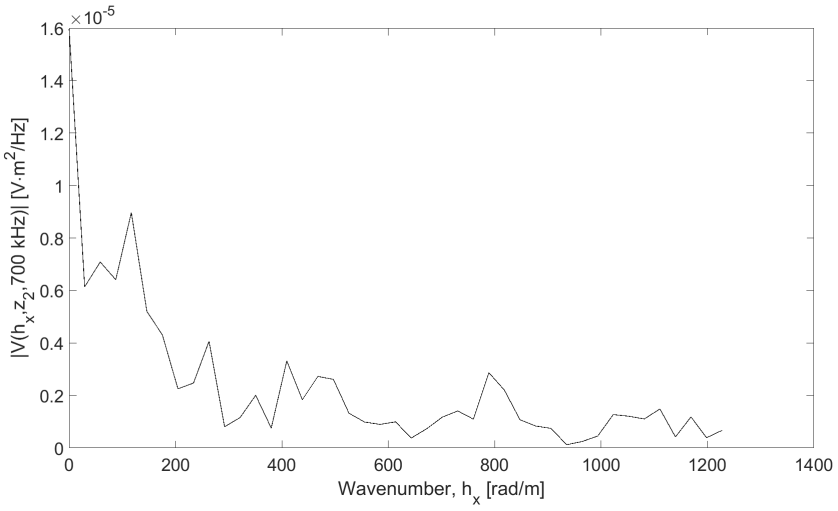

FIGURE 5.92: Voltage wavenumber spectrum $|V(h_x, z_2, 955kHz)|$

In Fig. 5.92 the magnitude of the voltage wavenumber spectrum of $V(h_z, z_2, 700\,kHz)$ is plotted. This was Hankel transformed from the results from Fig. 5.85, but shifted $5\,mm$ in the negative z-direction because of the discrepancy between the maximum of $|V(x, z_2, 700\,kHz)|$ and $|V(x, z_2, 955\,kHz)|$. Here we see a maximum at $h_x = 0\,rad/m$.

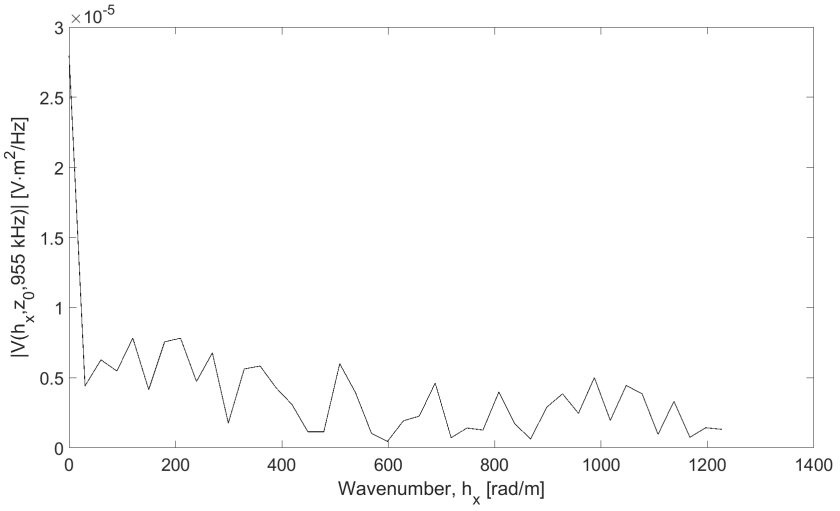

FIGURE 5.93: Voltage wavenumber spectrum $|V(h_x, z_2, 955kHz)|$

In Fig. 5.93 the voltage wavenumber spectrum $|V(h_x, z_0, 955\,kHz)|$ is plotted. The voltage wavenumber spectrum is Hankel transformed from Fig. 5.86 along with the phase component. We see a peak at $h_x = 0$ but no other discernible features. The wavenumber spectrum ends well before $h_x = h_f$ of $4040.7 rad/m$.

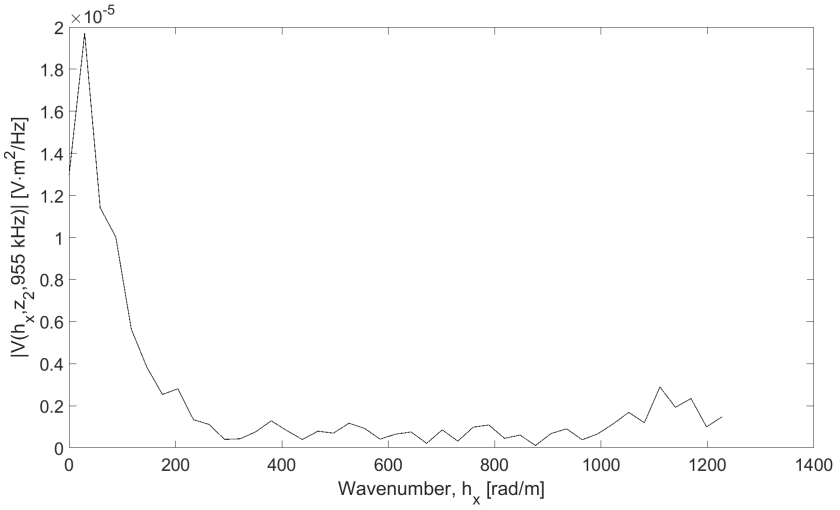

FIGURE 5.94: Voltage wavenumber spectrum $|V(h_x, z_2, 955kHz)|$

In Fig. 5.94 the magnitude of the wavenumber spectrum $V(h_x, z_2, 955\,kHz)$ is plotted. This spectrum was Hankel transformed from the plot in Fig. 5.106 with the phase. Here the plot starts at a local minimum before quickly rising to the maximum magnitude. Further along h_x no other discernible features are present.

5.3.5 Transmission Coefficient

In this section the transmission coefficient calculated from the voltage wavenumber spectra in Sect. 5.3.4 will be presented. The transmission coefficient is calculated using Eq. 3.5 and is detailed in Sect. 3.4.8.

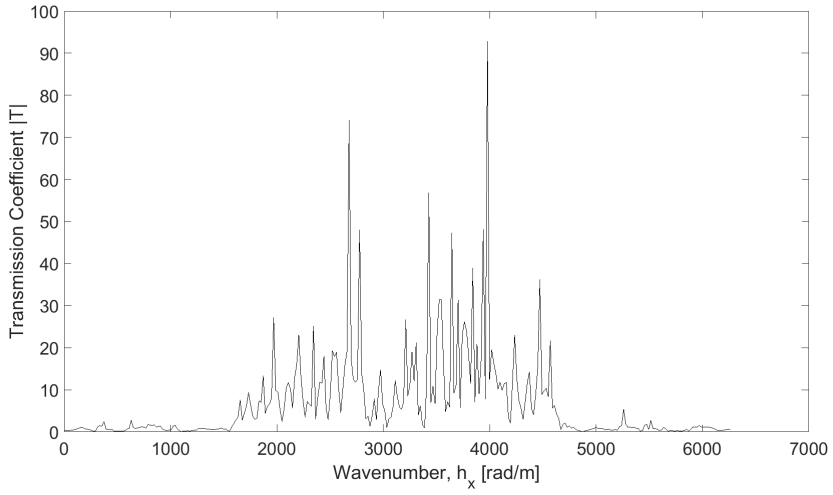

FIGURE 5.95: Magnitude of transmission coefficient $T_M(h_x, 455kHz)$, from measurement 1

In Fig. 5.95 the transmission coefficient for $|T_M(h_x, 455\,kHz)|$ is plotted. The vertical axis shows the magnitude of T_M and the horizontal axis shows the wavenumber h_x. This transmission coefficient is calculated using the voltage wavenumber spectrum $V(h_x, z_0, 455\,kHz)$ from Fig. 5.88 and $V(h_x, z_2, 455\,kHz)$ from Fig. 5.90. The absolute value of transmission is between 0 and 1. As is evident in the figure this limit is exceeded. This is caused by inconsistencies in the voltage wavenumber spectrum. The highest peaks of $|T_M|$ can be found between $h_x = 1500$ and $h_x = 4900$. Theoretically $|T_M|$ should be zero after $h_x = h_f$, which is at $h_x = 1925.2\,rad/m$. This is not however what is observed in Fig. 5.95. This is caused by the voltage wavenumber spectra used in the calculation. In theory the magnitude of these should also be zero in the evanescent region. This is not the case and the result are these very large peaks in $|T_M|$.

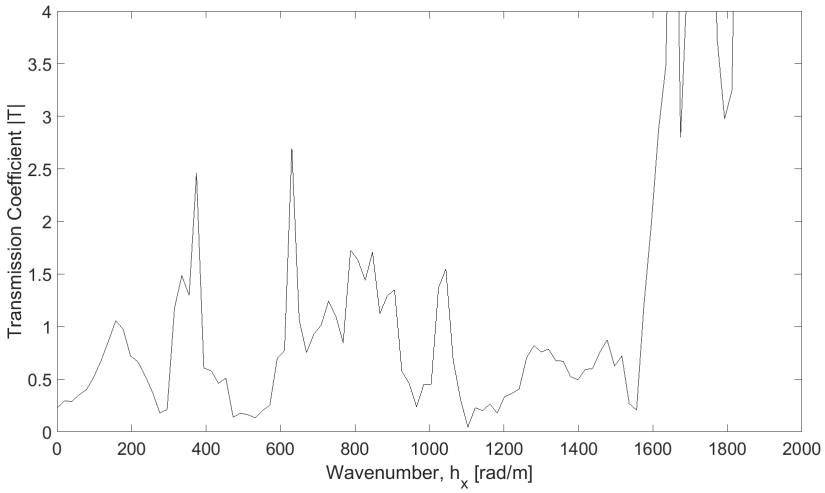

FIGURE 5.96: Zoomed in $|T_M(h_x, 455kHz)|$ from Fig. 5.95

Fig. 5.96 shows the region of $|T_M|$ before the evanescent region of Fig. 5.95. In this interval $|T_M|$ still exceeds unity but by a smaller margin. The first peak of $|T_M|$ has a value of 1.057.

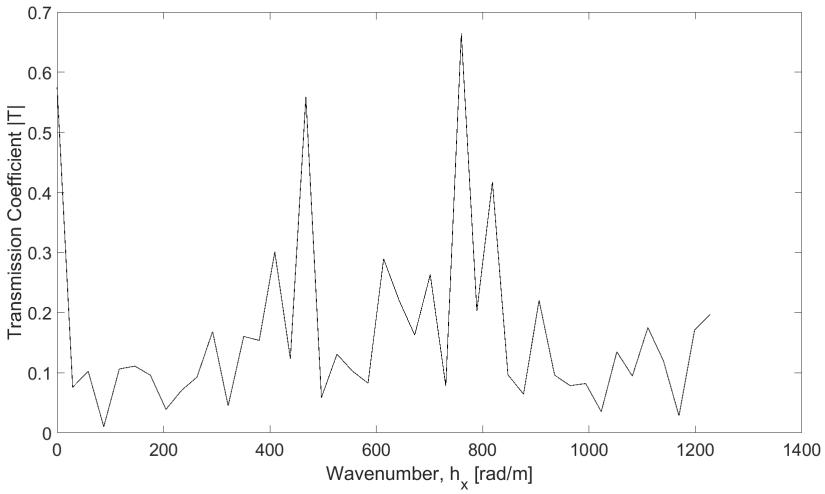

FIGURE 5.97: Magnitude of transmission coefficient $T_M(h_x, 700kHz)$, from measurement 3

The transmission coefficient $T_M(h_x, 700\,kHz)$ calculated from the voltage wavenumber spectra from measurement 3 in Fig. 5.91 and Fig. 5.92 is shown in Fig. 5.97. The transmission coefficient $|T_M|$ never rises above unity for the frequency $f = 700\,kHz$. There is a peak at $h_x = 0$ with a minimum afterwards. Further there are two significant peaks at $h_x = 468\,rad/m$ and $h_x = 760\,rad/m$.

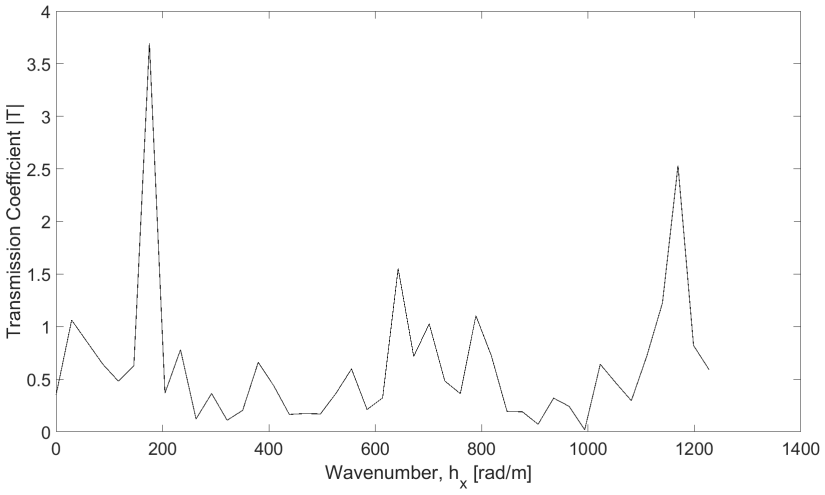

FIGURE 5.98: Magnitude of transmission coefficient $T_M(h_x, 955kHz)$, from measurement 3

In Fig. 5.98 the transmission coefficient $T_M(h_x, 955\,kHz)$ is plotted. This transmission coefficient is calculated from the voltage wavenumber spectra of Figs. 5.93 and 5.94. The plot has a maximum of just above 1, $|T_M| = 1,06$, at $h_x = 29\,rad/m$ but then has a peak far exceeding unity at $h_x = 175\,rad/m$.

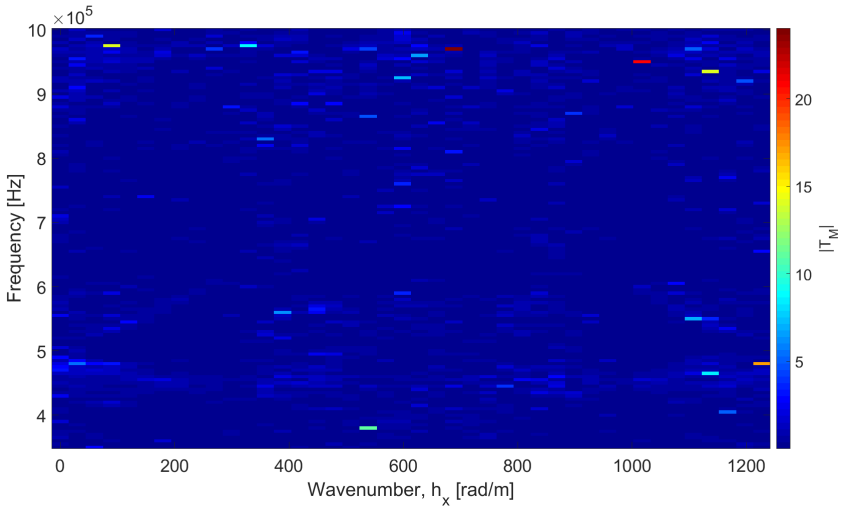

FIGURE 5.99: Magnitude of transmission coefficient T_M, from measurement 3

The entirety of the calculated magnitude transmission coefficient $|T_M|$ is plotted in Fig. 5.99. This is the result from measurement 3. Here the frequency f is plotted along the vertical axis and the wavenumber h_x along the horizontal axis. There aren't many features discernible in this plot as some large peaks of $|T_M|$ diminish other values.

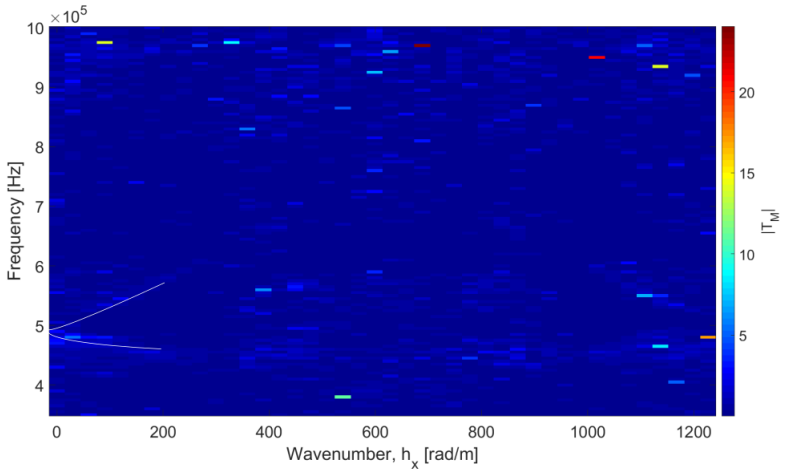

FIGURE 5.100: Magnitude of transmission coefficient T_M from Fig. 5.99. With indicated lines

One feature from Fig. 5.99 worth noting are what seem to be two distinct lines marked here and seen in Fig. 5.99 which start at $h_x = 0$. These lines do follow the same path as the S_{-2} and S_2 modes. This will be compared in the next section.

5.4 Comparison of ASM Results and Measurement Results

In this section the different results from the ASM model and measurements will be compared and discussed. This includes pressure/voltage spectra components, pressure/voltage wavenumber spectra and transmission coefficient. To begin with the pressure/voltage spectra components will be compared.

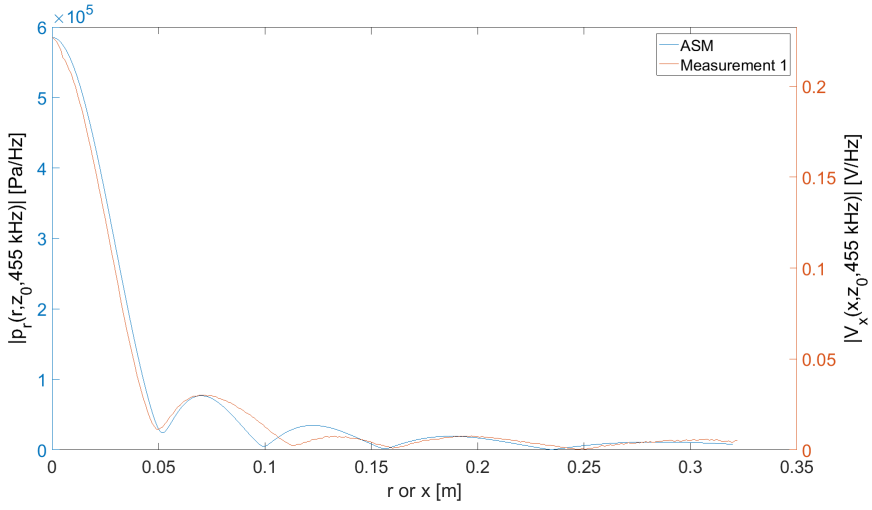

FIGURE 5.101: Magnitude comparison of $p_r(r, z_0, 455kHz)$ from Fig. 5.14 and $V_x(x, z_0, 455kHz)$ from Fig. 5.82

In Fig. 5.101 the magnitude of the simulated pressure spectrum component, $p(r, z_0, 455\,kHz)$ from Fig. 5.14 denoted $|p_r|$, and the magnitude of the measured voltage spectrum component, $V(x, z_0, 455\,kHz)$ from Fig. 5.82 denoted $|V_x|$, are compared. The figure has two different vertical axes, one for each spectrum component. The left axis corresponding to $|p_r|$ and the right axis corresponding to $|V_x|$. This means the plots are

fitted as to be able to compare them, this is a qualitative comparison. Comparing $|p_r|$ and $|V_x|$ they follow a similar path along the main lobe with $|p_r|$ having a minimum at $r = 0.052\,m$ and $|V_x|$ having a minimum at $x = 0.049\,m$. $|p_r|$ has narrower side-lobes compared to $|V_x|$ which results in divergence between the paths. Overall the measured and simulated results are qualitatively similar.

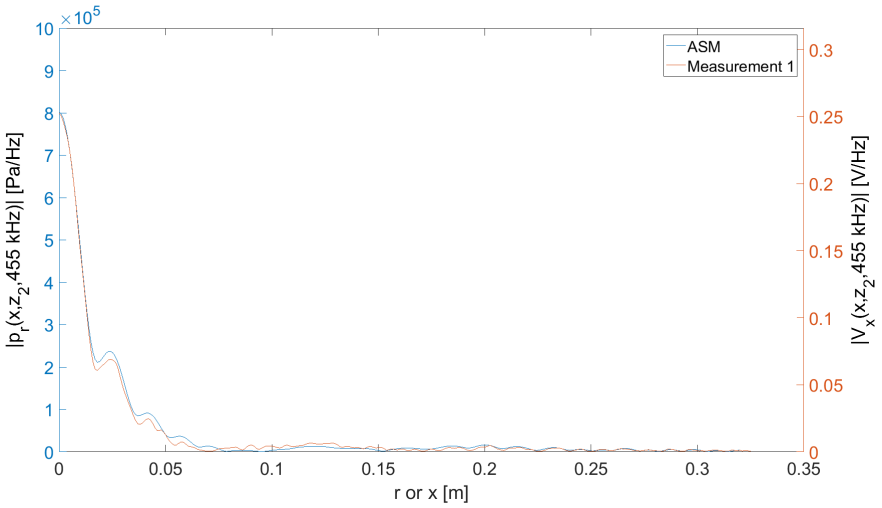

FIGURE 5.102: Magnitude comparison of $p_r(r, z_2, 455kHz)$ from Fig. 5.15 and $V_x(x, z_2, 455kHz)$ from Fig. 5.83

In Fig. 5.102 the magnitude of the simulated pressure spectrum component $p_r(r, z_2, 455\,kHz)$, from Fig. 5.15, and the magnitude of the voltage spectrum component $V_x(x, z_2, 455\,kHz)$, from Fig. 5.83, are compared. Throughout the graph the plots are qualitatively similar. Both $|p_r|$ and $|V_x|$ have a local minimum at $r\,or\,x = 0.018\,m$. More fluctuation is observed in $|V_x|$ further along the x-axis when compared to $|p_r|$.

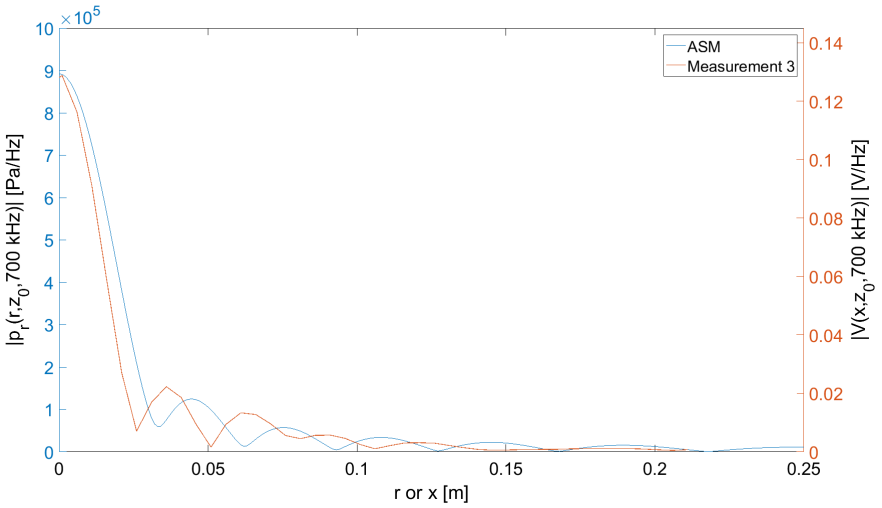

FIGURE 5.103: Magnitude comparison of $p_r(r, z_0, 700kHz)$ from Fig. 5.16 and $V_x(x, z_0, 700kHz)$ from Fig. 5.84

In Fig. 5.103 the simulated pressure spectrum component $|p_r(r, z_0, 700\,kHz)|$ and the voltage spectrum component from measurement 3,$|V_x(x, z_0, 700\,kHz)|$. The measured spectrum component has a narrower main-lobe than that of the simulated one. Both have roughly the same shape and are comparably similar.

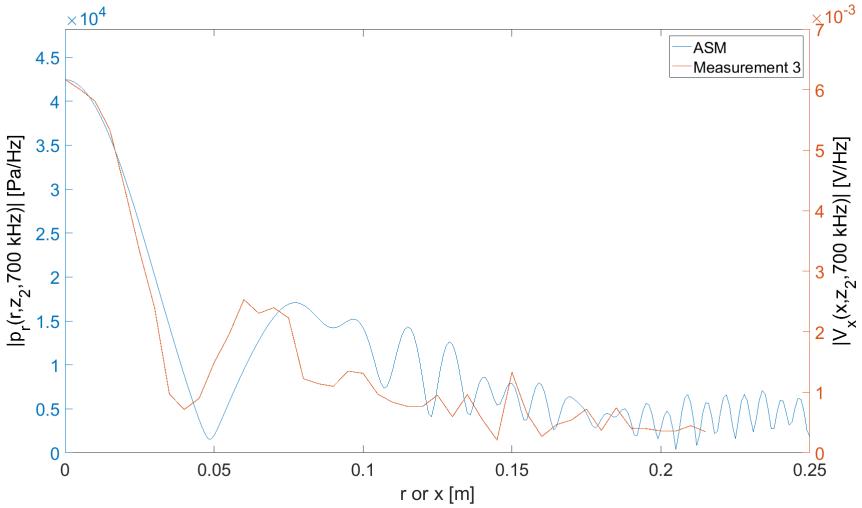

FIGURE 5.104: Magnitude comparison of $p_r(r, z_2, 700kHz)$ from Fig. 5.17 and $V_x(x, z_2, 700kHz)$ from Fig. 5.84

The simulated pressure spectra component $|p_r(r, z_2, 700\,kHz)|$, from Fig. 5.17 and the voltage spectrum component $|V_r(x, z_2, 700\,kHz)|$, from Fig. 5.85, are compared in Fig. 5.104. Both figures show the large drop in pressure when compared to the z_0 position of Fig. 5.103. Both also show the relatively high pressure/voltage compared to the main lobe of the pressure/voltage further along the r *or* x-axis. $|V_x|$ has a $\Delta x = 5\,mm$ and is therefore less detailed than p_r which has a $\Delta r = 1\,mm$. This makes the detail of the spectrum component not possible to sample for $|V_x|$.

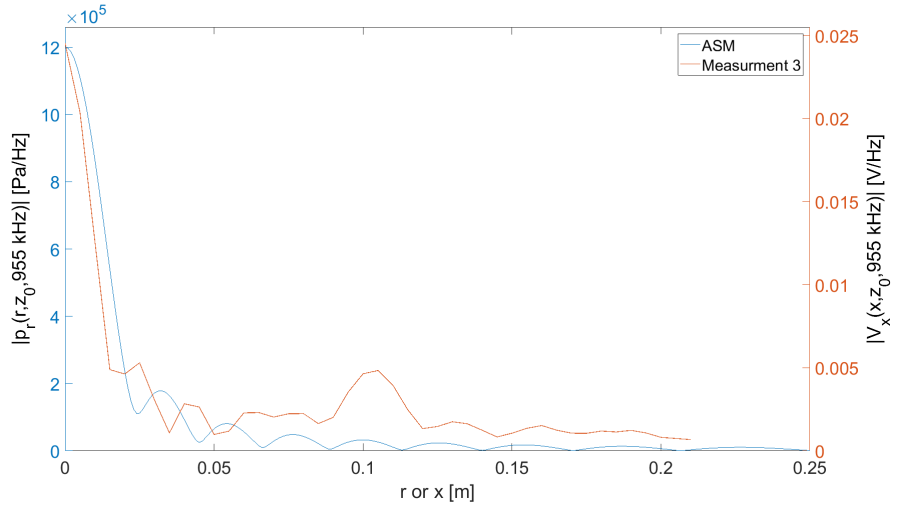

FIGURE 5.105: Magnitude comparison of $p_r(r, z_0, 955kHz)$ from Fig. 5.18 and $V_x(x, z_0, 955kHz)$ from Fig. 5.86

Fig. 5.105 shows the comparison of the magnitude of the simulated pressure spectrum component $p_r(r, z_0, 955kHz)$ from Fig. 5.18 and the magnitude of the voltage spectrum component $V_x(x, z_0, 955\,kHz)$ from Fig. 5.86. Both have a narrower main-lobe when compared to previous frequencies at position z_0. V_x has however an increase in voltage at $x = 0.107\,m$, which is not found in p_r.

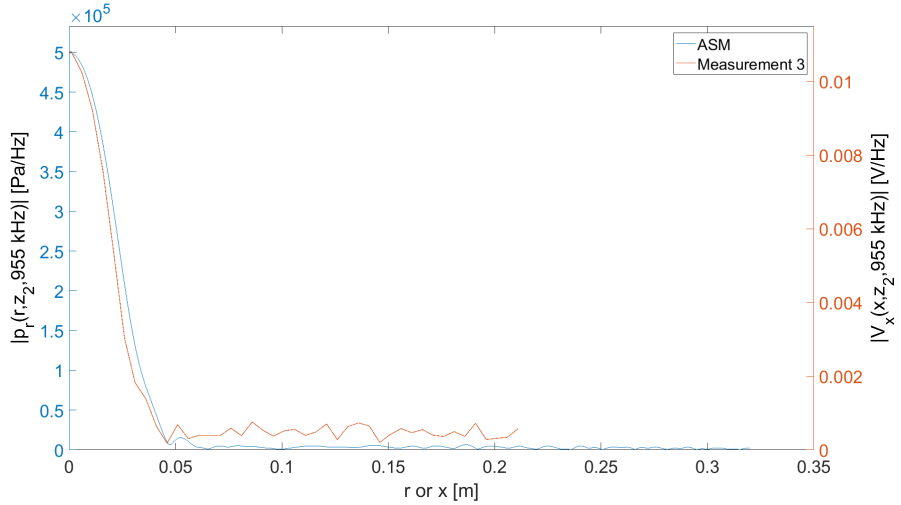

FIGURE 5.106: Magnitude comparison of $p_r(r, z_2, 955kHz)$ from Fig. 5.19 and $V_x(x, z_2, 955kHz)$ from Fig. 5.86

In Fig. 5.106 the magnitude of $p_r(r, z_2, 955\,kHz)$ from the simulated results in Fig. 5.19 is compared with the magnitude of the voltage spectrum component $V_x(x, z_2, 955\,kHz)$ from Fig. 5.87. Both show a large main-lobe, with no discernible features further along the horizontal axis. The voltage of $|V_x|$ further along x is comparably higher than $|p_r|$ when compared to the magnitude at x or $r = 0$. This may be the result of the low SNR at these positions for $V(x, z_0, t)$, which results in artificially high magnitudes.

Overall the simulated pressure spectra component, $|p_r|$, are fair approximations of the measurement results $|V_x|$. There are discrepancies for every frequency, but the main-lobe is in general approximated quite well.

Next the voltage/pressure wavenumber spectra calculated from the measured results, V_M, from Sect. 5.3.4 and the directly calculated spectra from Sect. 5.1.2 are compared. In some figures the Hankel transformed spectrum, P_H discussed in Sect. 4.2.3, is included if it is needed to illustrate an effect. Here there are two vertical axis as well and the plots are fitted in the vertical direction.

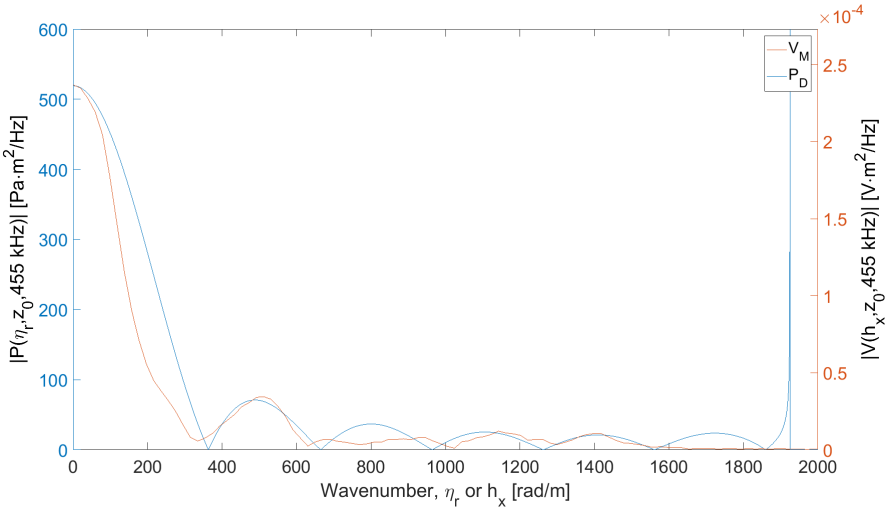

FIGURE 5.107: Magnitude comparison of $P_D(\eta_r, z_0, 455kHz)$ from Fig. 5.2 and $V_M(h_x, z_0, 455kHz)$ from Fig. 5.88

The comparison of $|P_D(\eta, z_0, 455\,kHz)|$ from Fig. 5.2 and $|V_M(h_x, z_0, 455\,kHz|)$ from 5.88 is plotted in Fig. 5.107. Here the right vertical axis corresponds to $|P_D|$ and the left to $|V_M|$. They both have a maximum at $\eta/h_x = 0$ and have diminishing side-lobes. $|V_M|$ has the first minimum at $h_x = 334,8 rad/m$ while P_D has it at $\eta = 363,5 rad/m$. Overall there are similarities between the two wavenumber spectra.

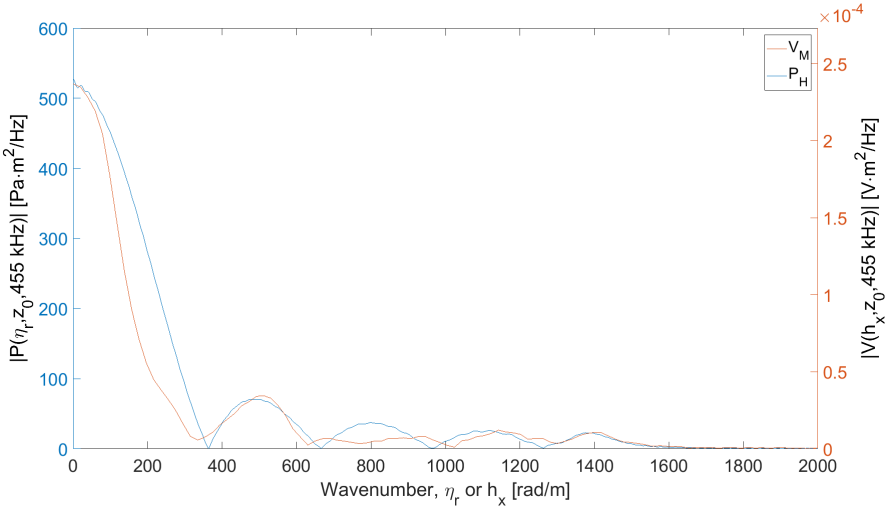

FIGURE 5.108: Magnitude comparison of $P_H(\eta_r, z_0, 455kHz)$ from Fig. 5.26 and $V_M(h_x, z_0, 455kHz)$ from Fig. 5.88

Comparing the magnitude of $P_H(\eta_r, z_0, 455\,kHz)$ and $V_M(\eta_r, z_0, 455\,kHz)$ an interesting similarity is observed. While there are differences between $|P_H|$ and $|V_M|$ both spectra approach zero after $\eta_r\, or\, h_x = 1400\, rad/m$. This indicates that the measurement results are a valid approximation along the same interval as $|P_H|$ is.

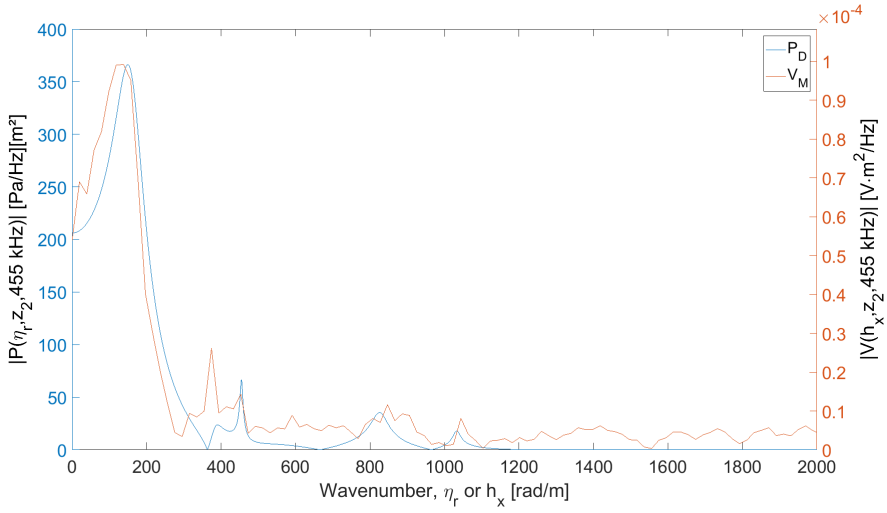

FIGURE 5.109: Magnitude comparison of $P_D(\eta_r, z_2, 455kHz)$ from Fig. 5.28 and $V_M(h_x, z_2, 455kHz)$ from Fig. 5.90

In Fig. 5.109 the transmitted pressure/voltage wavenumber spectra for the frequency $455\,kHz$ are compared. $|P_D|$ has its maximum at $\eta = 150,7 rad/m$, while $|V_M|$ has it at $h_x = 137,9\,rad/m$. $|P_D|$ and $|V_M|$ both start at a lower value before reaching their maximum and quickly descend to a minimum. Further both $|P_D|$ and $|V_M|$ have local maximums and minimums, but do not overlap as well as the first maximum and minimum. Overall we see similarities between these plots before $|P_D|$ approaches zero.

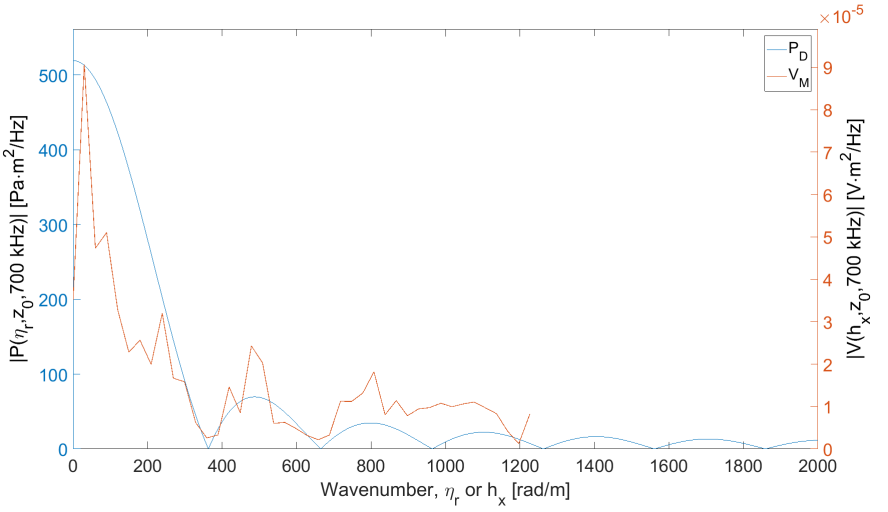

FIGURE 5.110: Magnitude comparison of $P_D(\eta_r, z_0, 700kHz)$ from Fig. 5.32 and $V_M(h_x, z_0, 700kHz)$ from Fig. 5.91

In Fig. 5.110 the magnitude of the directly calculated spectrum P_D and the measured spectrum V_M for the frequency $f = 700\,kHz$ and position $z = z_0$ are plotted. $|V_M|$ does not seem to resemble $|P_D|$ in any significant way.

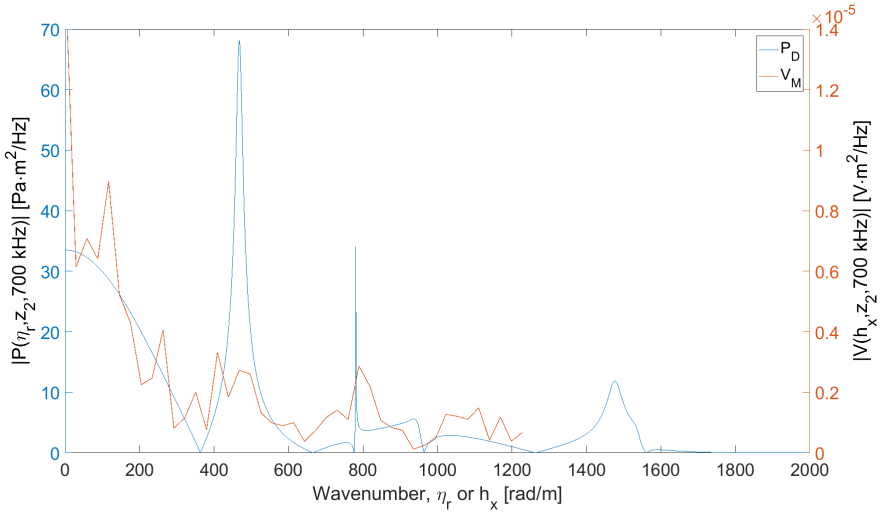

FIGURE 5.111: Magnitude comparison of $P_D(\eta_r, z_2, 700kHz)$ from Fig. 5.33 and $V_M(h_x, z_2, 700kHz)$ from Fig. 5.92

In Fig. 5.104 it is difficult to see any correlation between $|P_D|$ and $|V_M|$. $|V_M|$ starts at a high value and drops quickly before having a slight curve as $|P_D|$, but because of the large variation in $|V_M|$ this is not necessarily indicative of anything. The other peaks of $|P_D|$ are narrow and because of the large Δh_x of $|V_M|$ they can not be represented by $|V_M|$. Lastly the final peak of $|P_D|$ is beyond the extent of $|V_M|$.

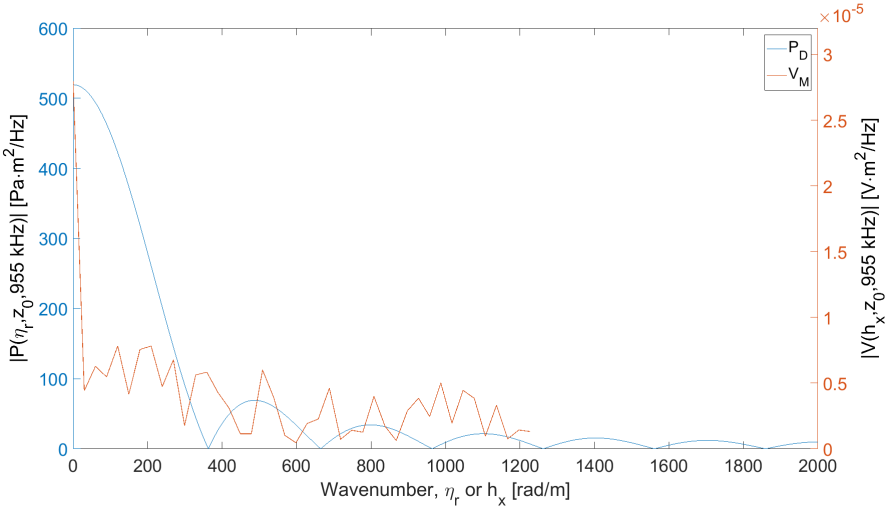

FIGURE 5.112: Magnitude comparison of $P_D(\eta_r, z_0, 955kHz)$ from Fig. 5.35 and $V_M(h_x, z_0, 955kHz)$ from Fig. 5.93

In Fig. 5.112 the pressure/voltage wavenumber spectra for $f = 955\,kHz$ at z_0 are plotted. The shape of $|V_M|$ does not seem to resemble $|P_D|$ in any significant way.

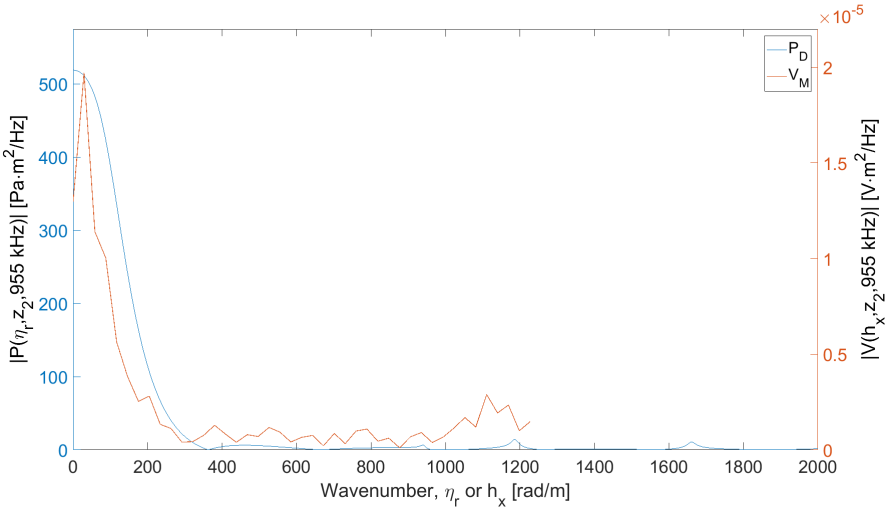

FIGURE 5.113: Magnitude comparison of $P_D(\eta_r, z_2, 955kHz)$ from Fig. 5.36 and $V_M(h_x, z_2, 955kHz)$ from Fig. 5.94

In Fig. 5.113 the pressure/voltage wavenumber spectra for $f = 955\,kHz$ is plotted. The spectrum $|V_M|$ has the same limited extent and resolution as the other spectra from measurement 3. $|V_M|$ does not start at a maximum as $|P_D|$. $|V_M|$ starts lower and rises quickly to a maximum at $h_x = 29$ while $|P_D|$ has its maximum at $\eta = 0$. Following the maximum $|V_M|$ quickly decreases to a local minimum at $h_x = 292\,rad/m$. $|P_D|$ has its first minimum at $\eta = 362,2\,rad/m$. Following the first minimum $|V_M|$ stays at relatively low pressures, but not as low as $|P_D|$ does relative to its maximum.

Through the comparison of the pressure wavenumber spectra from the simulation and the voltage wavenumber spectra from the measurements it was observed that for the results from measurment 1 at the frequency $455\,kHz$ we saw some correlation between the spectra, both for z_0 and z_2. However for the results from measurment 3 at $700\,kHz$ and $900\,kHz$ no meaningful similarity could be observed.

Now the transmission coefficients from the ASM model shown in Sect. 5.1.2 and the transmission coefficient obtained from the measurments shown in Sect. 5.3.5 will be compared.

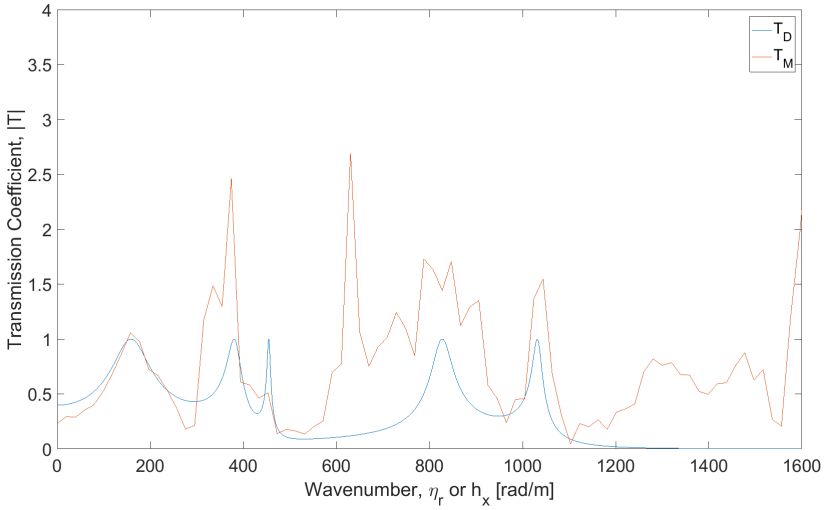

FIGURE 5.114: Comparison of $|T_D(\eta, 455kHz)|$ from Fig. 5.5 and $|T_M(h_x, 455kHz)|$ from Fig. 5.95

Comparing the directly calculated transmission coefficient $|T_D|$ with the measured transmission coefficient $|T_M|$, in Fig. 5.114. Unlike in the pressure spectrum components plots and pressure wavenumber spectra plots, the transmission coefficient is not dependant on units of the input and can therefore be compared on the same scale. Both $|T_D|$ and $|T_M|$ start at a lower $|T|$-value. $|T_D(0, 455\,kHz)| = 0.3977$ while $|T_{M1}(0, 455\,kHz)| = 0.23$. Both $|T_M|$ and $|T_D|$ have a maximum around $\eta\, or\, h_x = 155\,rad/m$ with $|T_M(158\,rad/m, 455\,kHz)| = 1.06$ and $|T_D(159, 3rad/m, 455\,kHz)| = 1$. $|T_M|$ and $|\,T_D|$ are very close in the first maximum of transmission coefficient. Further on $|T_M|$ exceeds unity by a large margin on the next maximums, this indicates that the results are more unreliable in these regions.

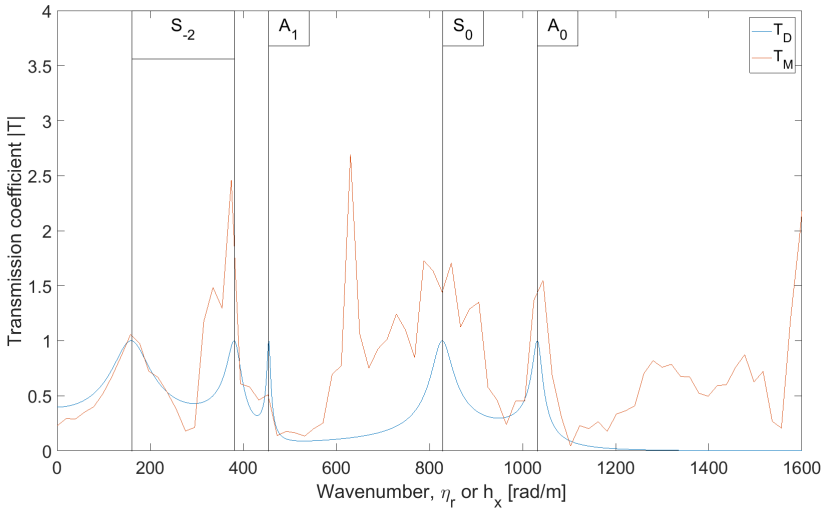

FIGURE 5.115: Comparison of $|T_D(\eta, 455kHz)|$ from Fig. 5.5 and $|T_M(h_x, 455kHz)|$ from Fig. 5.95 with leaky Lamb modes labeled

In Fig. 5.115 the plots from Fig. 5.115 with the modes are labeled. These values are consistent with Fig. 5.1. We can see an indication that the S_{-2}-mode is approximated through measurements for the frequency $455\,kHz$ at $h_x = 158\,rad/m$. The

second part of the S_{-2} mode is not as well reconstructed. $|T_M|$ does have a maximum near, but exceeds unity with $|T_M| = 2.46$, which suggests the data is not as reliable for this wavenumber. The A_1 mode is quite narrow spanning approximately $22\,rad/m$, which is just above $\Delta h_x = 19.7\,rad/m$. This means the mode is unlikely to be approximated with the experimental setup used here. At higher wavenumbers $|T_M|$ is more erratic. The peak at $630\,rad/m$ is at a wavenumber where the transmission in theory should be quite low. There are however peaks near both the S_0 and A_0 modes, how reliable this is however is questionable.

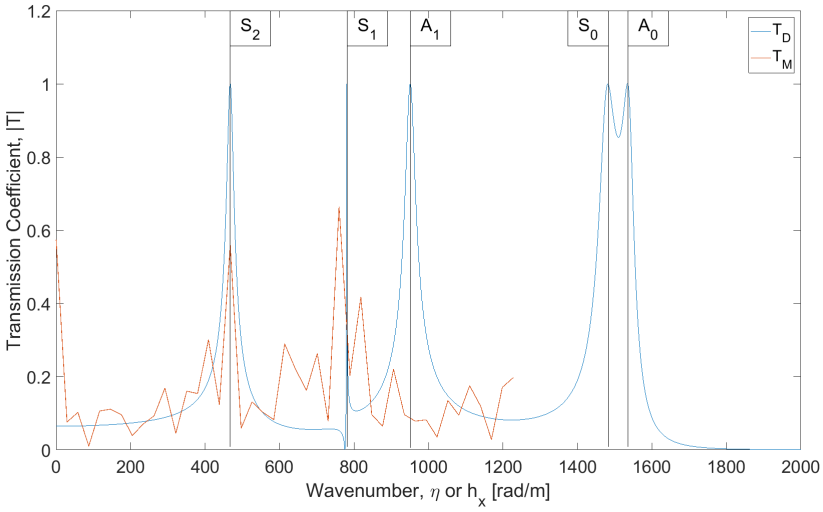

FIGURE 5.116: Comparison of $|T_D(\eta, 700kHz)|$ from Fig. 5.9 and $|T_M(h_x, 700kHz)|$ from Fig. 5.97 with leaky Lamb modes labeled

In Fig. 5.116 the directly calculated transmission coefficient $|T_D|$ from Fig. 5.9 and $|T_M|$, for $f = 700\,kHz$ are plotted. Here the lack of extent in T_M is very evident. The last two modes are outside the interval of T_M. Within the extent of T_M an attribute of $|T_D|$ is noted, most of transmission coefficient resides below 1. While $|T_D|$ starts at $|T_D(0, 700\,kHz)| = 0.065$ T_{M3} starts at $|T_M(0, 700kHz)| = 0,57$. The S_2-mode is the first mode at $700\,kHz$ and can seem to be shown by T_M, but as seen in Figs. 5.110 and 5.111 the results from measurement 3 are not necessarily indicative of anything substantial. The S_1-mode for $700\,kHz$ is very narrow with a width at the bottom of under $10\,rad/m$, significantly below $\Delta h_x = 29.9\,rad/m$, so the peak of T_M at $h_x = 760\,rad/m$ may be insignificant. There is no particular indication of the A_1-mode in T_M.

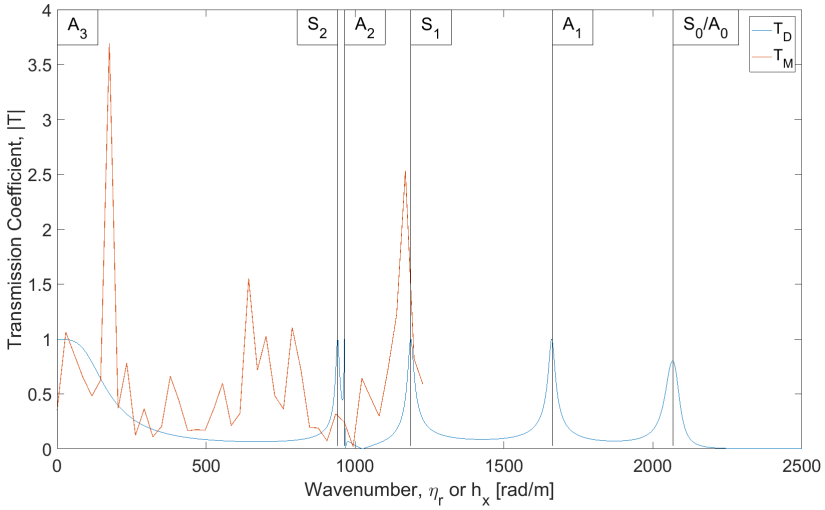

FIGURE 5.117: Comparison of $T_D(\eta, 955kHz)$ from Fig. 5.13 and $T_{M3}(h_x, 955kHz)$ from Fig. 5.98

In Fig. 5.117 the directly calculated transmission coefficient $|T_D|$ from Fig. 5.13 and the transmission coefficient calculated from measurement 3, $|T_M|$ from Fig. 5.98, for $f = 955\,kHz$ are plotted. The extent of $|T_M|$ is far below the needed $h_{x,max}$ for $955\,kHz$ and is very evident in the plot. $|T_D|$ starts at unity, while $|T_M(0,35\,rad/m, 955\,kHz)| = 0.35$. $|T_M|$ quickly rises to a local maximum at $|T_M(29\,rad/m, 955\,kHz)| = 1,06$. If the local maximum of $|T_M|$ indicates the A_3 mode is not certain, especially as $|T_M|$ quickly exceeds unity after. Where $|T_D|$ has a large section of little transmission $|T_M|$ gives little indication if this. The modes S_2 and A_2 are in close proximity and both narrow, meaning any distinction between them would be impossible with the Δh_x of T_M. There is a slight peak close to these peaks, but this can not be asserted with any certainty that it is caused by the modes. S_1 is the last mode within the extent of $|T_M|$, which has a peak close to the mode, however because of the uncertainty of the plot with regards to the other modes this can not be asserted.

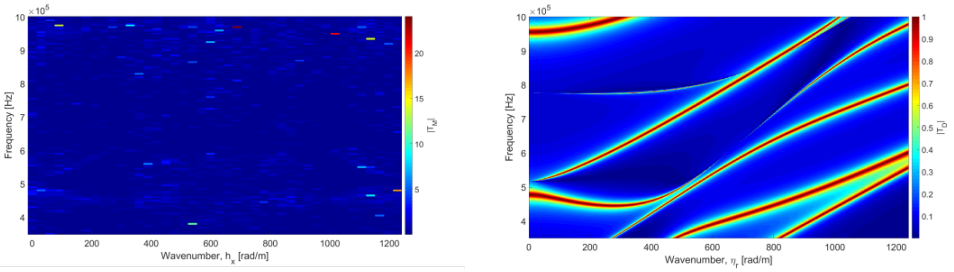

FIGURE 5.118: Comparison of $|T_D|$ from Fig. 5.1 and $|T_M|$ from 5.99

The comparison of the directly calculated transmission coefficient from 5.1 and the one obtained from measurement 3 in Fig. 5.99, is shown in Fig. 5.118. Overall the similarities are not evident. There is only one main section of interest. The area between $f = 400\,kHz$ and $f = 600\,kHz$ below η_r or $h_x = 400\,rad/m$. Here the two faint lines shown in Fig. 5.100 are comparable to the transmission lines of $|T_D|$. In this region we saw from the results of measurement 1, that a more accurate representation of the transmission coefficient was achieved.

5.5 Final Thoughts

The results from the on-axis showed that the effects observed by among others Lohne and Aanes [27, 11] were also observed here. Comparing the results with that of Aanes there were some slight discrepancies between the results, but overall they showed the same effects noted by e.g. [11, 27].

The unexpected failure of measurement 2 meant the intended data used for the reconstruction of the transmission coefficient was not available. Instead the data with the intended parameters was only available for the frequency $455\,kHz$. Luckily measurement 3 was already conducted, although with different parameters, and was usable. There were also issues with the acquisition of the data, in the form of what seemed to be fluctuations of the sampled intervals the cause of which is uncertain. In addition the presence of other signals on the negative side of t was also unexpected, but did not have a direct impact on the processing of the data. Following the data available and the acquisition the processing of this data was also an issue. With less than ideal post-processing of the sampled signal $V(x, z, t)$, the phase of the signal was not usable for any study. This is the direct result of the post-processing window assignment and the need for a more robust method of assigning this. Following the assignment of the post-processing window, the issue of the low SNR observed in some sample intervals is also an area that was not addressed in the post-processing. Lastly the issue of Hankel transforming the voltage spectrum with nonzero magnitudes may have caused aliasing effects. Despite these issues some promising results were acquired. From the comparison of the transverse H_{pp} transfer function with the simulated results from in Sect. 5.3.2 we saw the measurement results showed similar magnitudes to the simulated ones. All the measured voltage spectrum components from Sect. 5.3.3 showed qualitative similarities with the simulated pressure spectrum components from Sect. 5.1.3. Following this the limited resolution and extent of measurement 3 impacted the results of the voltage wavenumber spectra $V_M(h_x, z, f)$ of Sect. 5.3.4. However the voltage wavenumber spectrum for $f = 455\,kHz$ from measurement 1 in Figs. 5.88 and 5.90, showed comparable results to the simulated results especially with $|P_H|$. The transmission coefficient from measurement 1, in Fig. 5.95 showed promising results when compared with the simulated transmission coefficient in Fig. 5.5. This was seen in the lower wavenumbers, which was expected when considering the effect seen in Fig. 5.108. Here we saw that with this implementation a full approximation of the pressure/-voltage wavenumber spectrum was not possible, and this was also supported by the simulated $|P_H(\eta_r, z_0, 455\,kHz)|$. Meaning $|T_M|$ is restricted to the same interval. In Fig. 5.118 we saw that results from measurement 3 also had comparable results to the directly calculated transmission coefficient, although in a very limited region.

Chapter 6

Conclusion and Further Work

A short summary of the objective of the thesis and what was achieved is given. Following this som suggestions for further work is given.

6.1 Conclusion

This thesis had as an objective to study the beam transmission through a steel plate both on-axis and traversing along an axis. The on-axis measurement results were compared and showed comparable results to previous work. Using the transverse measurements and the use of the 2D Hankel transformation the measured voltage was transformed to the horizontal wavenumber-domain. Further these results were used to reconstruct the transmission coefficient. In conjunction with simulated results from the ASM model developed by Midtbø [24] several stages of this process were compared. Through the comparison we saw several promising results, particularly from the measurement with the widest extent and highest resolution. The results that were in agreement with the theoretical transmission coefficient were in the lower wavenumbers, well below $h_x = h_f$. The results also showed the need for a more robust post-processing method and how this can affect the results. Overall the results showed promising results for the the objective of reconstructing the transmission coefficient using normal incidence ultrasonic beam transmission and equidistant measurements.

In the middle of march the Covid-19 outbreak resulted in the closing of the university for approximately 6 weeks. This was done understandably to hinder further spread. The closing of the university meant that the measurements being conducted at that time were stopped and any further physical research was not possible. Because of this the final measurements needed were not conducted until late April until the middle of May. When measurement 2 turned out to be unusable there was little time to troubleshoot the issue with the setup and conduct the measurement again.

6.2 Further Work

For further work the proper handling of the post-processing is important. Having a robust method of assigning and processing the post-processing window is highly important in order to have accurate measurements for both the magnitude and the phase. Another possible improvement would be to have rotational control of the hydrophone in order to have the incident angle of the direct signal be as low as possible. Increasing the voltage input to the transducer may also be beneficial to increase the SNR. Addressing the abrupt end of the voltage spectrum components

would also help with aliasing effects in the voltage wavenumber spectrum. The effect of limited spacial extent and resolution was documented throughout the thesis, and an increase of the spacial extent would be beneficial. Modelling the transmission could be done in FEM in order to have a more accurate model of the process if the transducer is recreated in the simulation.

Bibliography

[1] L. Rayleigh, "On the free vibrations of an infinite plate of homogeneous isotropic matter," *London Mathematical Society*, pp. 225–234, 1888.

[2] H. Lamb, "On the flexure of an elastic plate," *London Mathematical society*, pp. 70–91, 1889.

[3] H. Lamb, "On waves in an elastic plate,," *Royal society of London*, pp. 114–128, 1917.

[4] H. Reissner, "Der senkrechte und schäge durchtritt einer in einem flüssigen medium erzeugten ebenen delatations welle durch eie in diesem medium befindliche plan-parallelle feste platte,," *Helv. Phys. Acta*, vol. 11, pp. 140–155, 1938.

[5] M. F. M. Osborne and S. D. Hart, "Transmission, reflection and guiding of an exponential pulse by a steel plate in water.i. theory," *The Journal of Acoustical Society of America*, vol. 17, pp. 1–17, 1945.

[6] M. F. M. Osborne and S. D. Hart, "Transmission, reflection and guiding of an exponential pulse by a steel plate in water.ii. eksperiment," *The Journal of Acoustical Society of America*, vol. 18, pp. 170–184, 1946.

[7] F. H. Sanders, "Transmission of sound through thin plates," *Canadian Journal of Research*, vol. 17, pp. 179–193, 1939.

[8] R. D. Mindlin, M. Onoe, and M. A. Medick, "Mathematical theory of vibrations of elastic plates," *Proc. 11th Ann. Symp. Freq. Contr.*, pp. 17–40, 1957.

[9] S. Rokhlin, D. E. Chimenti, and A. H. Nayfeh, "On the topology of the complex wave spectrum in a fluid-coupled elastic layer," *The journal of the Acoustical Sciences Library*, vol. 85, pp. 1074–1080, 1989.

[10] P. Cawley and B. Hosten, "The use of large ultrasonic transducers to improve transmission coefficient measurements on viscoelastic anisotropic plates," *The Journal of Acoustical Society of America*, vol. 101, pp. 1373–1379, 1997.

[11] M. Aanes, *Interaction of piezoelectric transducer excited ultrasonic pulsed beams with fluid-embedded viscoelastic plate*. PhD thesis, University of Bergen, Department of Physics and Technology, 2013.

[12] K. D. Lohne, P. Lunde, and M. Vestrheim, "Ultrasonic signal transmission in plates: Study of a steel plate immersed in water," *Proceedings of the 31st Scandinavian Symposium on Physical Acoustics*, 2008.

[13] M. Aanes, K. D. Lohne, P. Lunde, and M. Vestrheim, "Finite element analysis of acoustic beam interactions with a plate at normal incidence: Comparison with a 3d angular spectrum method and measurements.," *Proceedings of the 34th Scandinavian Symposium on Physical Acoustics*, 2011.

[14] M. Aanes, K. D. Lohne, P. Lunde, and M. Vestrheim, "Dispersion properties of lamb and leaky lamb modes in elastic and viscoelastic plate," *Proceedings of the 40th Scandinavian Symposium on Physical Acoustics*, 2017.

[15] J. Jocker and D. Smeulders, "Minimization of finite beam effects in the determination of reflection and transmission coefficients of an elastic layer," *Ultrasonics*, vol. 46, pp. 42–50, 2007.

[16] A. Safaeinili and O. I. L. D. E. Chimenti, "Quantitative materials characterization using air coupled leaky lamb waves," *Ultrasonics*, vol. 46, pp. 42–50, 2007.

[17] Y. Bouzidi and D. R. Schmitt, "Quantitative modelling of reflected ultrasonic bounded beams and a new estimate of the schoch shift," *IEEE transactions on ultrasonics, ferroelectrics, and frequency control*, vol. 55, no. 12, pp. 1963–1971, 2008.

[18] W. Ke, M. Castaings, and C. Bacon, "3d finite element simulations of an air coupled ultrasonic ndt system," *Ultrasonics*, vol. 42, no. 6, pp. 524–533, 2009.

[19] B. C. Lee and W. J. Staszewski, "Modelling of lamb waves for damage detection in metallic structures: Part i. wave propogation," *Smart Materials and Structures*, vol. 12, no. 5, pp. 804–814, 2003.

[20] S. Banerjee, T. Kundu, and N. A. Alnuaini, "Dpsm technique for ultrasonic field modelling near fluid solid interface," *Ultrasonic*, vol. 46, no. 3, pp. 2486–2492, 2009.

[21] R. K. Johnson and A. J. Devaney, "Transducer model for a plate thickness measurement," *IEEE ultrasonics symposium*, pp. 502–504, 1982.

[22] D. P. Orofino and P. Pedersen, "Evaluation of angle-dependent spectral distortion for infinite planar elastic media via angular spectrum decomposition," *The Journal of Acoustical Society of America*, vol. 93, no. 3, pp. 1235–1248, 1993.

[23] J. Kocbach, *FEMP - Finite Element Modelling of Piezoelectric Structures. Theory and Verification for Piezoceramic Disks*. PhD thesis, University of Bergen, Department of Physics and Technology, 1999.

[24] S. Midtbø, "Beam diffraction effects in guided-wave transmission of fluid embedded elastic plate: Influence of receiver distance and finite aperture," Master's thesis, University of Bergen, Department of Physics and Technology, Bergen, Norway, 2018.

[25] M. J. Anderson and P. R. Martin, "Resonant transmission of a three-dimensional acoustic sound beam through a solid plate in air: theory and measurment," *The Journal of the Acoustical Society of America*, vol. 98, no. 5, pp. 2628–2638, 1995.

[26] M. Eileraas, "Lydhastighetsmålinger med og uten resonanseffekter i en viskoelastisk stålplate i vann," Master's thesis, University of Bergen, Department of Physics and Technology, Bergen, Norway, 2019.

[27] K. D. Lohne, P. Lunde, and M. Vestrheim, "Measurements and 3d simulations of ultrasonic directive beam transmission through water-immersed steel plate,," *Proceedings of the 34th Scandinavian Symposium on Physical Acoustics*, 2011.

[28] M. Aanes, P. Lunde, and M. Vestrheim, "Ultrasonic beam transmission through a steel plate at oblique incidence: Uniform piston vs. piezoelectric transducer.," *Proceedings of the 36th Scandinavian Symposium on Physical Acoustics*, 2013.

[29] Z. Su and L. Ye, *Identification of Damage Using Lamb Waves Vol 48*. Berlin: Springer, 2009.

[30] J. D. Achenbach, *Wave propagation in elastic solids*. Amsterdam, Holland: North Holland Publishing, 1973.

[31] P. Lunde, "Phys 374, lecture notes." University of Bergen, Department of Physics and technology, Bergen, Norway, 2006.

[32] E. G. Williams, *Fourier Acoustics: Sound Radiation and Nearfield Acoustical Holography*. Washington D.C, USA: Naval Research Laboratory, 1999.

[33] I. A. Viktorov, "Rayleigh and lamb waves. physical theory and applications," *Plenum Press*, 1970.

[34] J. Rose, *Ultrasonic waves in solid media*. United Kingdom: Cambridge University Press, 1999.

[35] L. E. Kinsler, A. R. Frey, A. B. Coppens, and J. V. Sanders, *Fundamentals of Acoustics: Fourth edition*. Hoboken, NJ, USA: John Wiley and Sons, 2000.

[36] S. P. Dawson, *Certificate of Calibration - Precision Acoustics PVDF Hydrophone Serial Number 1820*. National Physical Laboratory, Dorset, England, 2011.

[37] J. Oberfell, *AB 09-0987 Uni Bergen SMC Hydra TT Additional info LMS-100 PRS-110 V2*. Micos GmbH, Eschbach, Germany, 2009.

[38] Parker Automation, USA, *404XE Linear Positioning Tables, Catalogue 8087/USA*, 2006.

[39] M. Aanes, K. D. Lohne, P. Lunde, and M. Vestrheim, "Beam transmission of water-embedded steel plate at normal incidence. diffraction effects in the s_1 to s_3 region," *Proceedings of the 38th Scandinavian Symposium on Physical Acoustics*, 2015.

Appendix A

Transverse Measurement Script

```
x_start = -10   %start of measurement
x_end = 320     %end of measurement
delta_x = 1     %step interval
x_tot = (x_start:delta_x:x_end);


for i = 1:length(x_tot)

    x_pos = x_tot(i);

    pw = pwd;
    addpath(genpath(pw));

    %%%%%%%%%%%%%%%%%%%%%%%%written by M. Aanes

    id_sig = visa('ni', 'GPIB0::12::INSTR');

    DPORead_par.Samples = 100e3; % antall samples pï¿ skop
    DPORead_par.Ch=2; % Lese fra kanal 2 pï¿ skop
    DPORead_par.Average = 256;
    DPORead_par.burst_rate = 50;
    DPORead_par.screenRows = 4;
    DPORead_par.verticalScalings = [1e-3 10];

    ScopeOffset_par.OffsetMethod='ScopeZero';  %mode,mean,ScopeZero,Fourier
    ScopeOffset_par.SampleMethod='sample';  %sample, time, periods, auto
    ScopeOffset_par.StartStop=[1 100000];
    % ScopeOffset_par.Freq= 500e3;  %frequency

    id_scope = visa('agilent','USB0::0x0699::0x0410::C024017::0::INSTR'); % new
    id_scope.InputBufferSize = DPORead_par.Samples;
    id_scope.OutputBufferSize = DPORead_par.Samples;

    freq = 700e3:255e3:955e3;        %frequency range
    timeSig_gen = 130e-6;   % cycles freq * timeSig_gen = 1/T * tid

    %% Program starts
    fopen(id_sig);
    for ii = 1:length(freq)
```

```
        fprintf(id_sig,['FREQ ', num2str(freq(ii))]);
        fprintf(id_sig,['BM:NCYC ', num2str(ceil(freq(ii)*timeSig_gen))]);
        read_tmp = adjustAmplitudeScope_rev02(id_scope,DPORead_par,ScopeOffset_par);
        wf_save{ii} = read_tmp{2};
        x_save{ii} = read_tmp{1};
        ii
    end




    fclose(id_sig);
    fopen(id_scope);
    samleRate = query(id_scope,'HORizontal:MAIn:SAMPLERate?');
    fclose(id_scope);

    %%%%%%%%%%%%%%%%%%%%%%%%%

    name = ['Dispersjon' num2str(x_pos) '.mat']; %Make filename
    save (name, 'x_save', 'wf_save', 'x_pos', 'freq'); %Save relevant variables

    Micosstep(delta_x,1,0) %flytt hydrofon



end
```

Appendix B

Hankel transformation

```
%Program for Hankel transform
clear;
addpath(genpath('../subRutines'))
v_w = 1485; %fluid velocity
av_v = 1515; %average velocity
direct_pathz0 = 0.27; %path from transducer to plate
direct_path = 0.37605; %path from transducer to (x_0,z_2)
pps = 25000000; %Samples per second
periodFracJump = 1/16;
i = sqrt(-1);
samplestart_pl = 49e3; %Start sample for plate measurement
sampleend_pl = 49.5e3; %End sample for plate measurement
samplestart_wa = 47e3; % Start sample for water measurement
sampleend_wa = 47.5e3; %End sample for water measurement

min_freq = 350e3; %Start frequency
freq_step = 5e3; %Frequency step
max_freq = 1000e3; %End Frequency
frekvens = (min_freq:freq_step:max_freq);


x_step = 5e-3; %Spatial step
xstart2 = 0e-3; %x_0 value plate
xend2 = 210e-3; %x_max value plate
xmax2 = xend2-xstart2;
xstart0 = 0e-3; %x_0 value water
xend0 = 210e-3; %x_max value water
xmax0 = xend0-xstart0;

%Selecting the appropriate x-range
if abs(xmax2)>abs(xmax0)
    xmax = xmax0;
elseif abs(xmax2)<abs(xmax0)
    xmax = xmax2;
else
    xmax = xmax2;
end


x2 = (xstart2:x_step:xend2); %x-range of plate measurements
```

```
x0 = (xstart0:x_step:xend0); %x-range of water measurements
x = (0:x_step:xmax); %x-range of used measurements
fs = 1/x_step; %spatial frequency step
s_frek2 = (0:1/xmax:fs-1/xmax); %Spatial frequency range
kx = s_frek2*(2*pi); % horizontal wavenumber

Pn_pl = zeros(length(frekvens),length(kx));
Pn_v = zeros(length(frekvens),length(kx));
count1=1


addpath('Dispersjon.09.01') %Add folder
for ii = 1:length(x)
    av = num2str(x2(ii)*1e3);
    load(['Dispersjon', av , '.mat']) %load file
    freq_pl = freq; % get frequency from file
    x_pl = x_save; %get time from file
    wf_pl = wf_save; %get waveform from file

    displacement = abs(x(ii)); %x-displacement
    ray_path = sqrt(direct_path^2 + displacement^2); %calculate shortest path
    time_displacement = ray_path/av_v - direct_path/av_v; %Timedisplacement
    p_disp = ceil(time_displacement * pps); %pSample displacement

    %%%%%%%%%%%%%%%%%%%%%%%%%%%%%%%%%%%%%%%%%%%%
   %%%%%%% written by M. Aanes %%% edited by I. Ravndal

    %%%%%%%% apply steady state region
    SampleInfoStruct_pl.Start = 'sample'; %
    SampleInfoStruct_pl.StartVal = samplestart_pl + p_disp;
    SampleInfoStruct_pl.End = 'sample';
    SampleInfoStruct_pl.EndVal = sampleend_pl + p_disp;


    for jj = 1:length(freq) %fourier transform
        SigStruct_pl.x = x_pl{jj};
        t01 = x_pl{jj}(samplestart_pl+p_disp)

        SigStruct_pl.y = wf_pl{jj};
        SigStruct_pl.SigFreq = freq_pl(jj);

        CutOffIndxs  = find_index_in_sig(SigStruct_pl,SampleInfoStruct_pl);
        wf_pl_reg = wf_pl{jj}(CutOffIndxs(2):CutOffIndxs(3));
        FT_tmp_pl = fourier_transform(SigStruct_pl.x,wf_pl_reg,1); % call on subrutine

        ff = abs(FT_tmp_pl{2}).*exp(i*angle(FT_tmp_pl{2}) -i*(freq(jj)*(2*pi))*t01);
        matrix.f2{jj,count1}=ff;
        [a,b_indx] = max(abs(ff));
        MagFT_pl = ff(b_indx);
        ww = (i*angle(FT_tmp_pl{2}) -i*(freq(jj)*(2*pi))*t01);
        phasez2{jj,count1} = ww;
```

```
        matrix.z2(jj,count1) = MagFT_pl; %legger til i matrise

    end
    %%%%%%%%%%%%%%%%%%%%%%%%
    count1 = count1+1
end
rmpath('Dispersjon.09.01')


% % Same prcoess as previous loop
count2 = 1
addpath('Platetransverse.30.01')

for kk = 1:length(x)
    av = num2str(x0(kk)*1e3);
    load(['Dispersjon', av , '.mat']) %load filen
    freq_v = freq;
    x_v = x_save;
    wf_v = wf_save;

    displacement = abs(x(kk));
    ray_path = sqrt(direct_pathz0^2 + displacement^2);
    time_displacement = ray_path/v_w - direct_pathz0/v_w;
    p_disp = ceil(time_displacement * pps);

    SampleInfoStruct_v.Start = 'sample';
    SampleInfoStruct_v.StartVal = samplestart_wa + p_disp;
    SampleInfoStruct_v.End = 'sample';
    SampleInfoStruct_v.EndVal = sampleend_wa + p_disp;


    for ll = 1:length(freq)
        SigStruct_v.x = x_v{ll};
        t02 = x_v{ll}(samplestart_wa+p_disp);
        SigStruct_v.y = wf_v{ll};
        SigStruct_v.SigFreq = freq_v(ll);

        CutOffIndxs  = find_index_in_sig(SigStruct_v,SampleInfoStruct_v);
        wf_v_reg = wf_v{ll}(CutOffIndxs(2):CutOffIndxs(3));
        FT_tmp_v = fourier_transform(SigStruct_v.x,wf_v_reg,1);
        ff = abs(FT_tmp_v{2}).*exp(i*angle(FT_tmp_v{2}) -i*(freq(ll)*(2*pi))*t02)  ;
        matrix.f0{ll,count2}=ff;
        [a,b_indx] = max(abs(ff));
        MagFT_v = ff(b_indx);
        %MagFT_v = max(FT_tmp_v{2})*exp(-i*(freq(ll)*(2*pi))*t02);


        matrix.z0(ll,count2) = MagFT_v;
```

```
    end
    count2 = count2+1
end
rmpath('Platetransverse.30.01')

%%%%%%Hankel transform
count3 = 1
for ff = 1:length(frekvens)
     pf_pl = matrix.z2(ff,:);
     pf_v = matrix.z0(ff,:);
     for nn = 1:length(kx)
         et = kx(nn);
         Jnll = besselj(0,x.*et);
         P_pl = 2*pi.*pf_pl.*Jnll.*x;
         P_v = 2*pi.*pf_v.*Jnll.*x;
         step = x_step;

         y_mid_pl = 1/2*(P_pl(1:end-1)+P_pl(2:end)); %trapezoidal integration
         Pn_pl(count3,nn)  = sum(y_mid_pl)*step;
         y_mid_v = 1/2*(P_v(1:end-1)+P_v(2:end));
         Pn_v(count3,nn)  = sum(y_mid_v)*step;
     end
 count3=count3+1
 end



dr = num2str(x_step*1e3);
mr = num2str(xmax*1e3);
hf = transpose((frekvens*2*pi)/v_w);

TC = Pn_pl./(Pn_v.*exp(i.*hf*0.37)); % calculation of transmission coefficient
```

Appendix C

ASM model

```
    %Asm
clear
i = sqrt(-1);
rhof = 1000;
rhop = 8000;
d = 6.05e-3;
fmin = 350e3;
fmax = 1000e3;
fstep = 5e3;
freq = (fmin:fstep:fmax);
cf = 1485;
cl = 5780;
cs = 3130;
z0 = 0.270;
z2 = 0.37;
a = 0.01055;
v0 = 1;
Qf = inf;

etamin = 0;
etastep = 1e-3;
etastep2 = 1.33e-8;
etastep_h =1e-3;
etamax = 4250;
eta = (etamin:etastep:etamax);
eta_h = (etamin:etastep_h:etamax);

rmin = 0;
rstep = 1e-3;
rmax = 0.32;

r = (rmin:rstep:rmax);
na = eta*a;
PZ0d = zeros(length(freq),length(eta));
PZ2d = zeros(length(freq),length(eta));
ppz2 = zeros(length(freq),length(r));
ppz0 = zeros(length(freq),length(r));
Pnz2 = zeros(length(freq),length(eta_h));
Pnz0 = zeros(length(freq),length(eta_h));
```

```
J1 =  besselj(1,na);
Jnc = (2*J1)./na;
Jnc(1,1) = 1;
Vz = pi*a^2*v0.*Jnc;


cnt = 1
for ii = 1:length(freq)
    f = freq(ii);
    w = 2*pi*f;
    hf = w/cf;
    hff(cnt,:) = hf;
    hfzN = sqrt(hf^2-eta.^2);

    eta1 = 0:etastep:hf-0.01;
    eta2 = hf-0.01+etastep2:etastep2:hf+0.01-etastep2;
    eta3 = hf+0.01:etastep:etamax;

    hfz1 = sqrt(hf^2-eta1.^2);
    hfz2 = sqrt(hf^2-eta2.^2);
    hfz3 = sqrt(hf^2-eta3.^2);

    na1 = eta1*a;
    na2 = eta2*a;
    na3 = eta3*a;

    J11 = besselj(1,na1);
    Jnc1 = (2*J11)./na1;
    Jnc1(1,1) = 1;
    Vz1 = pi*a^2*v0.*Jnc1;

    J12 = besselj(1,na2);
    Jnc2 =(2*J12)./na2;
    Vz2 = pi*a^2*v0.*Jnc2;

    J13 = besselj(1,na3);
    Jnc3 = (2*J13)./na3;
    Vz3 = pi*a^2*v0.*Jnc3;


    PN = ((rhof*w)./hfzN.*Vz.*exp(i*hfzN*z0));
    PZ0d(cnt,:) = PN;

    P1 =((rhof*w)./hfz1.*Vz1.*exp(i*hfz1*z0));
    P2 =((rhof*w)./hfz2.*Vz2.*exp(i*hfz2*z0));
    P3 =((rhof*w)./hfz3.*Vz3.*exp(i*hfz3*z0));
    int1 = 1
    for mm = 1:length(r)
        rr = r(mm);
        J01 = besselj(0,eta1.*rr);
        J02 = besselj(0,eta2.*rr);
```

```
        J03 = besselj(0,eta3.*rr);
        Integrand1=(1/(2*pi)).*P1.*J01.*eta1;
        Integrand2=(1/(2*pi)).*P2.*J02.*eta2;
        Integrand3=(1/(2*pi)).*P3.*J03.*eta3;
        step1 = etastep;
        step2 = etastep2;
        step3 = etastep;

        ymidt1 = 1/2*(Integrand1(1:end-1)+Integrand1(2:end));
        ymidt2 = 1/2*(Integrand2(1:end-1)+Integrand2(2:end));
        ymidt3 = 1/2*(Integrand3(1:end-1)+Integrand3(2:end));

        ppz0(cnt,mm) = sum(ymidt1)*step1 + sum(ymidt2)*step2 + sum(ymidt3)*step3;
        f
        cnt
        int1 = int1+1
    end
    cnt = cnt+1
end

cont = 1
for jj = 1:length(freq)
    f = freq(jj);
    w = 2*pi*f;
    hf = w/cf;
    hfz2 = sqrt(hf^2-eta.^2);
    alphaf = 0.5*(hf/Qf);
    k = hf + i*alphaf;
    kapfz = sqrt(k^2 - eta.^2);
    kaplz = sqrt((w/cl)^2 - eta.^2);
    kapsz = sqrt((w/cs)^2 - eta.^2);

    tan1 = (sin(kaplz.*(d/2))./(cos(kaplz.*(d/2))));
    tan2 = (sin(kapsz.*(d/2))./(cos(kapsz.*(d/2))));
    cotan1 = 1./tan1;
    cotan2 = 1./tan2;

    AS = ((w/cs)^2-2.*eta.^2).^2.*tan1 + 4.*eta.^2.*kapsz.*kaplz.*tan2;
    S = ((w/cs)^2-2.*eta.^2).^2.*cotan1 + 4.*eta.^2.*kapsz.*kaplz.*cotan2;

    Y = (rhof/rhop).*(kaplz./kapfz).*(w/cs)^4;
    T = (i.*Y.*(AS+S))./((S-i.*Y).*(AS+i.*Y));
    T(isnan(T) | isinf(T)) = 0;



    Pzz2 = ((rhof.*w)./hfz2.*Vz.*T.*exp(i.*hfz2.*z2));
    PZ2d(cont,:) = Pzz2;
    int2 = 1

    for ss = 1:length(r)
```

```
        rr = r(ss);
        J0 = besselj(0,eta.*rr);
        Integrand = (1/(2*pi)).*Pzz2.*J0.*eta;
        step = etastep;

        y_midt = 1/2*(Integrand(1:end-1)+Integrand(2:end));
        ppz2(cont,ss)  = sum(y_midt)*step;
        f
        int2 = int2+1
        cont
    end

    cont = cont+1

end



% plot(abs(ppz2(105,:)));
 count = 1
 for pp = 1:length(freq)
     pz2 = ppz2(pp,:);
     pz0 = ppz0(pp,:);
     int3 = 1
     for nn = 1:length(eta_h)
         et = eta_h(nn);
         Jnll = besselj(0,r.*et);
         integran1 = 2*pi.*pz2.*Jnll.*r;
         integran2 = 2*pi.*pz0.*Jnll.*r;
         step2 = rstep;

         y_mid1 = 1/2*(integran1(1:end-1)+integran1(2:end));
         y_mid2 = 1/2*(integran2(1:end-1)+integran2(2:end));
         Pnz2(count,nn)  = sum(y_mid1)*rstep;
         Pnz0(count,nn) = sum(y_mid2)*rstep;
         count
         int3 = int3 +1
     end
 count=count+1
 end



TCD = PZ2d./(PZ0d.*exp(i*hff*z2));
TCH = Pnz2./(Pnz0.*exp(i*hf*z2));

dr = num2str(rstep*1e3);
mr = num2str(rmax*1e3);
```

Appendix D

On Axis Measurement Script and Post-Processing

```
%%%Program for on-axis measurment%%%%
% 1. Init
% 2. Finne center (Parkerstep) (Micosstep)
% 3. Kjør dette scriptet

% %% Sletting og addpath
% instrreset    % sletter alle lagrede instrumentobjekt
% clear         % sletter data
% clear path
pw = pwd;
addpath(genpath(pw));

%% Aktuelle input verdier

id_sig = visa('ni', 'GPIB0::12::INSTR');

DPORead_par.Samples = 100e3; % antall samples pï¿ skop
DPORead_par.Ch=2; % Lese fra kanal 2 pï¿ skop
DPORead_par.Average = 256;
DPORead_par.burst_rate = 50;
DPORead_par.screenRows = 4;
DPORead_par.verticalScalings = [1e-3 10];

ScopeOffset_par.OffsetMethod='ScopeZero';  %mode,mean,ScopeZero,Fourier
ScopeOffset_par.SampleMethod='sample';  %sample, time, periods, auto
ScopeOffset_par.StartStop=[1 100000];
% ScopeOffset_par.Freq= 500e3;  %frequency

id_scope = visa('agilent','USB0::0x0699::0x0410::C024017::0::INSTR'); % new
id_scope.InputBufferSize = DPORead_par.Samples;
id_scope.OutputBufferSize = DPORead_par.Samples;

freq = 455e3:5e3:455e3;
timeSig_gen = 130e-6;   % cycles freq * timeSig_gen = 1/T * tid
%freq_short_Meas = 500e3;
%cycle_short = 2;
%% Program starts
```

```
fopen(id_sig);
for ii = 1:length(freq)
    fprintf(id_sig,['FREQ ', num2str(freq(ii))]);
    fprintf(id_sig,['BM:NCYC ', num2str(ceil(freq(ii)*timeSig_gen))]);
    read_tmp = adjustAmplitudeScope_rev02(id_scope,DPORead_par,ScopeOffset_par);
    wf_save{ii} = read_tmp{2};
    x_save{ii} = read_tmp{1};
    ii
end
% fclose(id_sig);
% return
%% extra meas for Fourier method
%    fprintf(id_sig,['FREQ ', num2str(freq_short_Meas)]);
 %   fprintf(id_sig,['BM:NCYC ', num2str(cycle_short)]);
  %  read_tmp = adjustAmplitudeScope_rev02(id_scope,DPORead_par,ScopeOffset_par);
   % wf_short_save = read_tmp{2};
    %x_short_save = read_tmp{1};

fclose(id_sig);
fopen(id_scope);
samleRate = query(id_scope,'HORizontal:MAIn:SAMPLERate?');
fclose(id_scope);

%% saving parameters
save WaterTank_save.mat wf_save x_save freq samleRate


%%%%Program for Hpp transfer function%%%%%
    clear
addpath(genpath('../subRutines'))

SampleInfoStruct_wa.Start = 'sample';
SampleInfoStruct_wa.StartVal = 47.5e3;
SampleInfoStruct_wa.End = 'sample';
SampleInfoStruct_wa.EndVal = 48e3;

SampleInfoStruct_pl.Start = 'sample';
SampleInfoStruct_pl.StartVal = 49e3;
SampleInfoStruct_pl.End = 'sample';
SampleInfoStruct_pl.EndVal = 49.5e3;

% samplesForModeMean=8000;
% average_method = 'mode';    %'mode' or 'mean'
periodFracJump = 1/16;

load('D:\Ivar\New\Program/Dispersjon0.mat')
% load '/Home/siv25/msa022/Measurements/Post-Doc/Measurements Semi Tank/Low Water/Water
freq_wa = freq;
x_wa = x_save;
wf_wa = wf_save;
```

```
load('D:\Ivar\New\Program/Dispersjon-5.mat')
% load '/Home/siv25/msa022/Measurements/Post-Doc/Measurements Semi Tank/Low Water/WaterTank
freq_pl = freq;
x_pl = x_save;
wf_pl = wf_save;

%% Program starts

for ii = 1:length(freq_wa)
% ii=1;
SigStruct_wa.x = x_wa{ii};
% SigStruct_wa.y = wf_wa{ii} - feval(average_method,wf_wa{ii}(1:samplesForModeMean));
SigStruct_wa.y = wf_wa{ii};
SigStruct_wa.SigFreq = freq_wa(ii);

SigStruct_pl.x = x_pl{ii};
% SigStruct_pl.y = wf_pl{ii} - feval(average_method,wf_pl{ii}(1:samplesForModeMean));
SigStruct_pl.y = wf_pl{ii};
SigStruct_pl.SigFreq = freq_pl(ii);

CutOffIndxs  = find_index_in_sig(SigStruct_wa,SampleInfoStruct_wa);
    wf_wa_reg = wf_wa{ii}(CutOffIndxs(2):CutOffIndxs(3));
    PeakInfo_wa = findPeaksAndZeros(SigStruct_wa.x,wf_wa_reg,freq_wa(ii),periodFracJump);
    SteadyState_wa{ii} = PeakInfo_wa{3};   % cos signal in steady state
    FT_tmp_wa = fourier_transform(SigStruct_wa.x,SteadyState_wa{ii},1);
    MagFT_wa(ii) = max(abs(FT_tmp_wa{2}));
    SteadyState_amplitude_wa(ii) = mean(abs(wf_wa_reg(PeakInfo_wa{1})));

    CutOffIndxs  = find_index_in_sig(SigStruct_pl,SampleInfoStruct_pl);
    wf_pl_reg = wf_pl{ii}(CutOffIndxs(2):CutOffIndxs(3));
    PeakInfo_pl = findPeaksAndZeros(SigStruct_pl.x,wf_pl_reg,freq_pl(ii),periodFracJump)
    SteadyState_pl{ii} = PeakInfo_pl{3};   % cos signal in steady state
    FT_tmp_pl = fourier_transform(SigStruct_pl.x,SteadyState_pl{ii},1);
    MagFT_pl(ii) = max(abs(FT_tmp_pl{2}));
    SteadyState_amplitude_pl(ii) = mean(abs(wf_pl_reg(PeakInfo_pl{1})));
end

Hpp_fourier = MagFT_pl./MagFT_wa;
Hpp_amplitude = SteadyState_amplitude_pl./SteadyState_amplitude_wa;

close all;plot(freq_wa,20*log10(Hpp_fourier))
legend('Fourier')
%figure;plot(freq_wa,20*log10(Hpp_amplitude))


%%%%Temporal Fourier transform%%%%

    function out = FourierMethod(x,y,SigFreq,periodFracJump,tresh_onset,tresh_unwrap,ZeroPa

% % phase_tmp_ref  = FourierMethod(x_ref,y_ref,SigFreq,periodFracJump,tresh_onset,tresh_unw
% %         ,ZeroPadSide_Method_Value,ValueCutStart_ValueCutDuration,MethodCutStart_MethodD
```

```
% %         ,ShearWaveTimePrediction_ref);
%
% clear
% % close all
% addpath('/Home/siv25/msa022/MATLAB/AllPrograms/main/plotting')
%
% % filenameRef = '/Home/siv25/msa022/Results Measurements/Time_Signals/methane/Referen
% % filenameRef = '/Home/siv25/msa022/Results Measurements/Time_Signals/methane/shear/M
% % load(filenameRef);
% load('test.mat');
%
% %     x = Meas{1}{2}{1};
% %     y = Meas{1}{2}{2};
% x = x_pl;
% y = y_pl;
% region = ShearWaveTimePrediction_pl;
% %
% %
% % periodFracJump = 1/16;
% % tresh_onset = [2 0.3];   %[manual/relMax  valueManual/fracMax]
% % SigFreq = 400e3;
% % CutDownStartAndDurationPeriods = [3 1];
% % MethodDuration = [1 1];
% % tresh_unwrap = 2;
% % SideMethodValue = [1 0 50000];


%%%%%%%%%%%%%%%%%%%%%%%%%%%%%%%%%%%%%%%%%%%%%%%%%%%%%%%%%%%%%%%%


    onset_tmp = findOnsetFromMax(x,y,tresh_onset,SigFreq,periodFracJump,region);
    onset = onset_tmp{1};
    y2 = y(onset:end);

%   Standard.x = x;
%   Standard.y2 = y2;
%   Standard.periodFracJump = x;
%   Standard

  y3_tmp= goToZeroHead(x,y2,SigFreq,periodFracJump,MethodCutStart_MethodDuration,ValueC
  y3 = y3_tmp{1};
  CutDownStart = y3_tmp{2}+y3_tmp{3};
  y4 = ZeroPadCutSetLength(y3,ZeroPadSide_Method_Value);
%   y4 = y3(1:10000);
fourier_tmp = fourier_transform(x,y4);
X_k = fourier_tmp{2};
% break
% X_k =
phase_X_k = atan(imag(X_k)./real(X_k));
freq_fourier = fourier_tmp{1};
unwrap_tmp = UnwrappingBothWays(phase_X_k,tresh_unwrap);
```

```
phase_unwrap = unwrap_tmp{1};

% phase_K_k_save{counter} = phase_X_k;
% phase_unwrap_save{counter} = phase_unwrap;
% counter = counter+1;
%   end


  out{1} = freq_fourier;
  out{2} = phase_unwrap;
  out{3} = phase_X_k;
  out{4} = y4;
  out{5} = onset;
  out{6} = CutDownStart-1+onset;
  out{7} = X_k;
  out{8} = onset_tmp{2};  % maxIndex
  out{9} = onset_tmp{3};  % maxIndexNxt

% close all;figure('Position', [2300, 50, 700, 450]);plot(freq_fourier,20*log10(abs(X_k)))
% figure('Position', [2300, 50, 700, 450]);plot(freq_fourier,phase_X_k);xlim([0 1e6])
% figure('Position', [2300, 50, 700, 450]);plot(y3)
% figure('Position', [2300, 50, 700, 450]);plot(freq_fourier,phase_K_k_save{3});xlim([0 1e6
% figure('Position', [2300, 50, 700, 450]);plot(freq_fourier,phase_unwrap_save{3});xlim([0




%     y2(1:ee)
```